Preparation, Characterisation and Optimization of Blocking Layers for Improving Efficiency of Dye-Sensitized Solar Cells

A thesis submitted to Cardiff University in the candidature
for the degree of
Doctor of Philosophy

by

Mateusz Michał Augustyniak

Institute of Energy
School of Engineering
Cardiff University

September 2016

Abstract

This study explored and described deposition of titanium oxide thin films as blocking layers in dye-sensitized solar cells using the pulsed laser deposition technique. This technique facilitates precise control of deposition conditions that were manipulated to prepare titanium oxide thin films. The electrical, optical and structural properties of the deposited films were investigated and their dependence on these conditions was studied. The key task of the research was to incorporate the deposited films into the structure of dye-sensitized solar cells in order to improve their efficiency that is adversely effected by electron-hole recombination at the interface of transparent conductive oxide and electrolyte. The titanium oxide thin films were successfully grown on fluorine-doped tin oxide coated glass that was used to fabricate the dye-sensitized solar cells. The photovoltaic parameters of the prepared dye-sensitized solar cells were studied using current-voltage characterization method. Influence of blocking layer deposition conditions on dye-sensitized solar cell performance was investigated. Correlation between the optical and electrical properties of deposited titanium oxide blocking layers and the performance of fabricated dye-sensitized solar cells as a function of the thin film deposition conditions was found. Based on that, region of optimal deposition conditions of this type of blocking layers for improving efficiency of dye-sensitized solar cells can be found.

Declaration and statements

DECLARATION

This work has not previously been accepted in substance for any degree and is not concurrently submitted in candidature for any other higher degree.

Signed…… (Mateusz Augustyniak) Date……

STATEMENT 1

This thesis is being submitted in partial fulfilment of the requirements for the degree of Doctor of Philosophy (PhD)

Signed…… (Mateusz Augustyniak) Date……

STATEMENT 2

This thesis is the result of my own independent work/investigation, except where otherwise stated. Other sources are acknowledged by explicit references.

Signed…… (Mateusz Augustyniak) Date……

STATEMENT 3

I hereby give consent for my thesis, if accepted, to be available for photocopying, inter-library loan, and for the title and summary to be made available to outside organisations.

Signed…… (Mateusz Augustyniak) Date……

Acknowledgements

First of all, I would like to thank my supervisor, Prof Gao Min for providing me with an opportunity to pursue research at Cardiff University and for his continuous support at every stage of my PhD and related research. I would also like to express my profound gratitude to him for his patience, motivation and immense knowledge.

I am also grateful to all the colleagues that I worked with for their support and help during my research, especially at the beginning to understand my research area, help in use of and managing some of the laboratory equipment, and in general for being a good example of concerned researchers. Therefore, my sincere thanks go to Dr Jorge García-Cañadas, Dr Lourdes Garcia, Dr John Bomphrey, Dr Tracy Sweet, Dr Hasan Hashim, Dr Matthew Phillips and Matthew Rolley.

I would also like to thank all my fellow laboratory mates for all the fun and social events we have had in the last four years.

I am also grateful to Dr Duncan Muir and Mr Tony Oldroyd of School of Earth and Ocean Sciences for letting me use the SEM and XRD facilities, without which the analysis part of this research would have been difficult.

Additionally, I would like to thank Dr Angela Sobiesierski and Ms Karen Barnett for their help and for letting me use their Cleanroom facilities.

I would like to thank the members of electrical workshop and mechanical workshop who always helped me with fixing faulty equipment, installation of new equipment and with the design and development of the screen-printing. Special thanks go to Malcolm Seaborne for the frequent and knowledgeable help always accompanied by a kind smile.

I would also like to thank all the staff in finance and research offices, especially to Mrs Pavlina Petkova and Mrs Christine Lee for their help in financial, administrative and procedural matters.

Last but not the least, I would like to thank my family: my parents and to my brother for supporting me spiritually throughout my PhD. I am thankful to my friends who were supporting me as well, and to those who were helping me going through the difficulties during my PhD.

And also thank you all who directly or indirectly played a role in smooth completion of this research.

List of symbols

d_f	Thickness of the films
FF	Fill factor
I	Current
I_{SC}	Short-circuit current
J_{SC}	Short-circuit current density
P_{in}	Intensity of incident light
P_{max}	Maximum power output
p_{O_2}	Oxygen partial pressure
R	Electrical resistance
r_d	Deposition rate
T	Optical transmittance
t_d	deposition duration
V	Voltage
V_{OC}	Open-circuit voltage
η	Efficiency
Φ^i	Radiant flux received by the sample
Φ^t	Radiant flux transmitted through the sample
θ	Beam irradiation angle
2θ	Diffraction angle
-ve	Negative terminal
+ve	Positive terminal

List of abbreviations

A	Anatase phase
AM	Air mass
BL	Blocking layer
BSE	Backscattered electrons
C_{BL}	Cell with blocking layer
CE	Counter electrode
C_{ST}	Standard-type cell
DSSC	Dye-Sensitized Solar Cell
ESEM	Emission gun environmental scanning electron microscope
FTO	Fluorine-doped tin oxide
G	Global
L	Layer
MSE	Mean Squared Error
NIR	Near-infrared
PDF	Powder diffraction file
PLD	Pulsed-Laser Deposition
PMMA	Polymethyl methacrylate
PTFE	Polytetrafluoroethylene
R	Rutile phase
RT	Room temperature
SD	Standard Deviation
SE	Standard error

SE	Secondary electrons
SEM	Scanning Electron Microscope
TCO	Transparent conductive oxide
TBP	4-*tetr*-butyl-pirydine
UV	Ultraviolet
UVA	Ultraviolet A
UVB	Ultraviolet B
VIS	Visible
WE	Working electrode
XRD	X-ray Diffraction

Contents

Abstract I

Declaration and statements II

Acknowledgements III

List of symbols V

List of abbreviations VI

List of figures XI

List of tables XVII

Chapter 1: Introduction 1

1.1 Motivation and objectives 1

1.2 Outline of the thesis 5

Chapter 2: Background 7

2.1 Introduction 7

2.2 Photovoltaics 7

2.3 Solar energy conversion 10

2.4 Dye-Sensitized Solar Cells 12

2.5 Blocking Layers 18

2.6 Pulsed Laser Deposition 24

2.7 Titanium oxide thin films 28

Chapter 3: Preparation of Ti-O thin films as Blocking Layers and preparation of Dye-Sensitized Solar Cells 34

3.1 Introduction 34

3.2 Deposition of Ti-O thin films by Pulsed Laser Deposition 34

3.3 Preparation of Dye-Sensitized Solar Cells with Blocking Layer 38

3.3.1 Working electrode preparation 40
3.3.2 Counter electrode preparation 43
3.3.3 Cell assembling 44
3.3.4 Filling cell with electrolyte solution 45
3.3.5 Electrical contacts preparation 45
3.4 Summary 46
Chapter 4: Characterisation of deposited thin films 47
4.1 Introduction 47
4.2 Crystallography 47
4.2.1 XRD technique 47
4.2.2 Results and analysis 49
4.3 Cross-sectional microscopy and film thickness determination 59
4.3.1 Cross-sectional scanning electron microscopy and ellipsometry 59
4.3.2 Influence of deposition duration 62
4.3.3 Influence of oxygen partial pressure 67
4.4 Optical transmittance 72
4.4.1 Spectroradiometer and measurement setup 72
4.4.2 Influence of deposition duration 79
4.4.3 Influence of oxygen partial pressure 89
4.5 Electrical resistance 100
4.5.1 2-point probes measurement method 100
4.5.2 Influence of deposition duration 105
4.5.3 Influence of oxygen partial pressure 109
4.5.4 I-V characteristics 113

Chapter 5: Current-voltage characteristics of fabricated DSSCs with BL under illumination 119
5.1 Introductions 119
5.2 Characterisation methods 119
5.3 Influence of BLs deposition duration on performance of DSSCs 123
5.3.1 Characterisation of best performing cells 123
5.3.2 Characterisation of sets of fabricated cells 132
5.4 Influence of oxygen partial pressure during BLs deposition on performance of DSSCs 141
5.4.1 Characterisation of best performing cells 141
5.4.2 Characterisation of sets of fabricated cells 149
Chapter 6: Conclusions and future work 159
6.1 Conclusions 159
6.2 Future work 161
References 163
Appendix A 178
Appendia B 182

List of figures

Figure 2.1: Diagram of typical dye-sensitized solar cell..... 14
Figure 2.2: Diagram of pulsed-laser deposition system..... 25
Figure 2.3: Scaled ball models of: (a) Rutile - unit cell parameters: a = b = 4.650 Å, c = 2.970 Å, α = β = γ = 90o; (b) Anatase - unit cell parameters: a = b = 3.807 Å, c = 9.705 Å, α = β = γ = 90o. Titanium atoms are coloured grey, oxygen atoms are coloured red..... 29
Figure 3.1: Components of PLD system; (a) substrate holder and FTO glass with deposited titanium oxide film, (b) TiO target. 35
Figure 3.2: Apparatus for Pulsed Laser Deposition. 36
Figure 3.3: Process flow-chart for deposition of titanium oxides thin films on FTO substrate via PLD..... 37
Figure 3.4: Subsequent stages of preparation of WE: (a) FTO glass, (b) the glass with porous structure of TiO_2, (c) the TiO_2 sensitized with dye; of CE: (d) FTO glass with drilled hole, (e) the glass coated with Pt; and (f) completed DSSC..... 39
Figure 3.5: Set for screen printing of titania pastes. 42
Figure 3.6: Assembling DSSC via heat transfer press. 44
Figure 3.7: DSSC backfilling with electrolyte under vacuum desiccator. 45
Figure 4.1: XRD patterns of the titanium oxide film deposited via PLD on Si wafer and FTO glass at 300°C, at oxygen partial pressure equal 0.26 mTorr, for 360 minutes..... 50
Figure 4.2: XRD patterns of the titanium oxide film deposited via PLD on FTO glass at 300°C, for 480 minutes, at oxygen partial pressures: 1.00 mTorr, 0.26 mTorr, and 0.14 mTorr; 2θ range: 0-80°. 52
Figure 4.3: XRD patterns of the titanium oxide film deposited via PLD on FTO glass at 300°C, for 480 minutes, at oxygen partial pressures: 1.00 mTorr, 0.26 mTorr, and 0.14 mTorr; 2θ range: 20-45°. 53
Figure 4.4: XRD patterns of the titanium oxide film deposited via PLD on FTO glass at 300°C, for 480 minutes, at oxygen partial pressures: 1.00 mTorr, 0.26 mTorr, and 0.14 mTorr; 2θ range: 45-70°. 56
Figure 4.5: Cross-sectional SEM image of the titanium oxide film deposited on FTO glass under p_{O_2} of 26 mTorr, at deposition duration of 120 minutes; sample BL120/0.26..... 63

Figure 4.6: Cross-sectional SEM image of the titanium oxide film deposited on FTO glass under p_{O_2} of 0.26 mTorr, at deposition duration of 30 minutes; sample BL30/0.26..... 64
Figure 4.7: Cross-sectional SEM image of the titanium oxide film deposited on FTO glass under p_{O_2} of 0.26 mTorr, at deposition duration of 15 minutes; sample BL15/0.26..... 65
Figure 4.8: Estimated thickness of thin film BLs obtained at p_{O_2} = 0.26 mTorr at different deposition durations; assessed by SEM and ellipsometry..... 66
Figure 4.9: Cross-sectional SEM image of the titanium oxide film deposited on FTO glass at deposition duration of 15 minutes, under p_{O_2} of 2.00 mTorr,; sample BL30/2.00..... 68
Figure 4.10: Cross-sectional SEM image of typical titanium oxide film deposited on FTO glass; sample deposited at 15 minutes, under p_{O_2} of 2.00 mTorr,; sample BL30/2.00. 69
Figure 4.11: Estimated thickness of thin film BLs obtained at t_d = 30 min, at different oxygen partial pressures; assessed by SEM and ellipsometry. Error bars represent SE for SEM, MSE for ellipsometry data. 71
Figure 4.12: Estimated deposition rate of thin film BLs obtained at t_d = 30 min, at different oxygen partial pressures; assessed by SEM and ellipsometry..... 72
Figure 4.13: Diagram of spectroradiometer with division into main units. 74
Figure 4.14: Flowchart of light transmittance measurement of the prepared samples..... 75
Figure 4.15: Setting up distance for transmittance measurement. 77
Figure 4.16: Measurement setup for light transmittance measurement of the prepared samples..... 78
Figure 4.17: Spectral transmittance of FTO glass and samples with BL obtained at p_{O_2} = 0.26 mTorr and at different deposition duration; data in range of 280 - 800 nm. The discontinuities around 380 nm arise from filter changes in the apparatus. 80
Figure 4.18: Calculated transmittance of FTO glass and samples with BL obtained at p_{O_2} = 0.26 mTorr and at different deposition duration; data in range of 280 - 800 nm. Values are encumbered with 5% error resulting from class B solar simulator. 82
Figure 4.19: Calculated transmittance of FTO glass and samples with BL obtained at p_{O_2} = 0.26 mTorr and at different deposition duration; data in range of 280 - 315 nm. Values are encumbered with 5% error resulting from class B solar simulator. 84

Figure 4.20: Calculated transmittance of FTO glass and samples with BL obtained at p_{O_2} = 0.26 mTorr and at different deposition duration; data in range of 315–400 nm. Values are encumbered with 5% error resulting from class B solar simulator. 85
Figure 4.21: Calculated transmittance of FTO glass and samples with BL obtained at p_{O_2} = 0.26 mTorr and at different deposition duration; data in range of 400 – 750 nm. Values are encumbered with 5% error resulting from class B solar simulator. 87
Figure 4.22: Spectral transmittance of FTO glass and samples with BL obtained at t_d = 30 min and under different oxygen partial pressure; data in range of 280 - 800 nm. The discontinuities around 380 nm arise from filter changes in the apparatus. 89
Figure 4.23: Calculated transmittance of FTO glass and samples with BL obtained at t_d = 30 min and under different oxygen partial pressure; data in range of 280 - 800 nm. Values are encumbered with 5% error resulting from class B solar simulator. 91
Figure 4.24: Calculated transmittance of FTO glass and samples with BL obtained at t_d = 30 min and under different oxygen partial pressure; data in range of 280 - 315 nm. Values are encumbered with 5% error resulting from class B solar simulator. 93
Figure 4.25: Calculated transmittance of FTO glass and samples with BL obtained at t_d = 30 min and under different oxygen partial pressure; data in range of 315 - 400 nm. Values are encumbered with 5% error resulting from class B solar simulator. 95
Figure 4.26: Calculated transmittance of FTO glass and samples with BL obtained at t_d = 30 min and under different oxygen partial pressure; data in range of 400 - 750 nm. Values are encumbered with 5% error resulting from class B solar simulator. 97
Figure 4.27: Setup for measurement of resistance using 2-point probes method by digital multimeter. 102
Figure 4.28: Setup for I-V characterisation using 2-point probes method by potentiostat. The distance between the electrodes is fixed and equals 1 cm. 104
Figure 4.29: Electrical resistance of the bare FTO substrate and samples with BL obtained at p_{O_2} = 0.26 mTorr, at different deposition durations. 105
Figure 4.30: Proposed paths of the current flow through the sample during the measurement; (a) dominant path through deposited film, (b) dominant path across the deposited film and mainly through FTO layer. 108
Figure 4.31: Electrical resistance of the bare FTO substrate and samples with BL obtained at t_d = 30 min, under different oxygen partial pressures. 110

Figure 4.32: Dark I-V characteristics of the bare FTO in three separate measurements (a)-(c); (d) general position of probes on the sample during the measurements. The distance between the probes is fixed and equals 1 cm. 114
Figure 4.33: Dark I-V characteristics of the carbon-coated (grey area) FTO substrate in three separate measurements (a)-(c); (d) general position of probes on the sample during the measurements a, and b,; (e) general position of probes on the sample during the measurement c. The distance between the probes is fixed and equals 1 cm. 115
Figure 4.34: Dark I-V characteristics of the sample with thin film deposited under p_{O_2} = 0.40 mTorr, at t_d = 120 min, obtained in three separate measurements a-c); d) general position of probes on the sample during the measurements. The distance between the probes is fixed and equals 1 cm. 117
Figure 5.1: Setup for calibration light intensity to 1000 W/m^2. 121
Figure 5.2: Setup for photocurrent-voltage characterisation of the DSSCs. 122
Figure 5.3: Photocurrent density-voltage characteristics of best-performing DSSCs without and with BLs deposited under the oxygen partial pressure of 0.26 mTorr. The measurement was taken under AM1.5 simulated-sunlight illumination (100 mW/cm^2). Initial temperature for each measurement was 25^{o}C. 124
Figure 5.4: Efficiencies of illuminated best-performing DSSCs without and with BLs deposited under the oxygen partial pressure of 0.26 mTorr against the deposition duration of these BLs. 126
Figure 5.5: Short-circuit current densities of illuminated best-performing DSSCs without and with BLs deposited under the oxygen partial pressure of 0.26 mTorr against the deposition duration of these BLs. 128
Figure 5.6: Open-circuit voltages of illuminated best-performing DSSCs without and with BLs deposited under the oxygen partial pressure of 0.26 mTorr against the deposition duration of these BLs. 130
Figure 5.7: Fill factors of illuminated best-performing DSSCs without and with BLs deposited under the oxygen partial pressure of 0.26 mTorr against the deposition duration of these BLs. 131
Figure 5.8: Averaged efficiencies of illuminated sets of DSSCs without and with BLs deposited under the oxygen partial pressure of 0.26 mTorr against the deposition duration of these BLs. 133

Figure 5.9: Averaged short-circuit current densities of illuminated sets of DSSCs without and with BLs deposited under the oxygen partial pressure of 0.26 mTorr against the deposition duration of these BLs. 135
Figure 5.10: Averaged open-circuit voltages of illuminated sets of DSSCs without and with BLs deposited under the oxygen partial pressure of 0.26 mTorr against the deposition duration of these BLs. 138
Figure 5.11: Averaged fill factors of illuminated sets of DSSCs without and with BLs deposited under the oxygen partial pressure of 0.26 mTorr against the deposition duration of these BLs. 140
Figure 5.12: Photocurrent density-voltage characteristics of best-performing DSSCs without and with BLs deposited at deposition duration of 30 minutes. The measurement was taken under AM1.5 simulated-sunlight illumination (100 mW/cm^2). Initial temperature for each measurement was 25^oC. 142
Figure 5.13: Efficiencies of illuminated best-performing DSSCs without and with BLs deposited at deposition duration of 30 minutes against the oxygen partial pressure used for deposition of these BLs. 144
Figure 5.14: Short-circuit current densities of illuminated best-performing DSSCs without and with BLs deposited at deposition duration of 30 minutes against the oxygen partial pressure used for deposition of these BLs. 146
Figure 5.15: Open-circuit voltages of illuminated best-performing DSSCs without and with BLs deposited at deposition duration of 30 minutes against the oxygen partial pressure used for deposition of these BLs. 147
Figure 5.16: Fill factors of illuminated best-performing DSSCs without and with BLs deposited at deposition duration of 30 minutes against the oxygen partial pressure used for deposition of these BLs. 148
Figure 5.17: Averaged efficiencies of illuminated sets of DSSCs without and with BLs deposited at deposition duration of 30 minutes against the oxygen partial pressure used for deposition of these BLs. 150
Figure 5.18: Averaged short-circuit current densities of illuminated sets of DSSCs without and with BLs deposited at deposition duration of 30 minutes against the oxygen partial pressure used for deposition of these BLs. 153

Figure 5.19: Averaged open-circuit voltages of illuminated sets of DSSCs without and with BLs deposited at deposition duration of 30 minutes against the oxygen partial pressure used for deposition of these BLs. 155
Figure 5.20: Averaged fill factors of illuminated sets of DSSCs without and with BLs deposited at deposition duration of 30 minutes against the oxygen partial pressure used for deposition of these BLs. 157
Figure A.1: I-V characteristics of the sample with thin deposited film that was carbon coated; measured in 3 positions, sample BL120/0.26 178
Figure A.2: I-V characteristics of the sample with thin deposited film that was carbon coated; measured in 3 positions, sample BL30/0.26 178
Figure A.3: I-V characteristics of the sample with thin deposited film that was carbon coated; measured in 3 positions, sample BL15/0.26 179
Figure A.4: I-V characteristics of the sample with thin deposited film that was carbon coated; measured in 3 positions, sample BL30/1.00 179
Figure A.5: I-V characteristics of the sample with thin deposited film that was carbon coated; measured in 3 positions, sample BL30/2.00 180
Figure A.6: I-V characteristics of the sample with thin deposited film that was carbon coated; measured in 3 positions, sample BL30/0.18 180
Figure A.7: I-V characteristics of the sample with thin deposited film that was carbon coated; measured in 3 positions, sample BL30/0.14 181
Figure A.8: I-V characteristics of the sample with thin deposited film that was carbon coated; measured in 3 positions, sample BL30/0.11 181

List of tables

Table 2.1: Comparison of several exemplary blocking layer materials, their deposition conditions and basic parameters of the DSSCs that incorporate those BLs. Data retrieved from reference materials. 22

Table 3.1: Basic deposition conditions and name of each sample in each deposition series. 38

Table 3.2: Types and names of DSSCs and incorporated BLs. 40

Table 4.1: The two sets of samples prepared for XRD analysis. 49

Table 4.2: Estimated thickness of thin film BLs obtained at p_{O_2} = 0.26 mTorr at different t_d; assessed by SEM and ellipsometry. 66

Table 4.3: Estimated thickness of thin film BLs obtained at t_d = 30 min, at different p_{O_2}; assessed by SEM and ellipsometry. 71

Table 4.4: List of measured samples and their basic deposition conditions. 74

Table 4.5: Calculated transmittance of FTO glass and samples with BL obtained at p_{O_2} = 0.26 mTorr and at different deposition duration. Values are encumbered with 5% error resulting from class B solar simulator. 83

Table 4.6: Calculated transmittance of FTO glass and samples with BL obtained at p_{O_2} = 0.26 mTorr and at different deposition duration. Values are encumbered with 5% error resulting from class B solar simulator. 84

Table 4.7: Calculated transmittance of FTO glass and samples with BL obtained at p_{O_2} = 0.26 mTorr and at different deposition duration. Values are encumbered with 5% error resulting from class B solar simulator. 86

Table 4.8: Calculated transmittance of FTO glass and samples with BL obtained at p_{O_2} = 0.26 mTorr and at different deposition duration. Values are encumbered with 5% error resulting from class B solar simulator. 87

Table 4.9: Calculated transmittance of FTO glass and samples with BL obtained at t_d = 30 min and under different oxygen partial pressure. Values are encumbered with 5% error resulting from class B solar simulator. 91

Table 4.10: Calculated transmittance of FTO glass and samples with BL obtained at t_d = 30 min and under different oxygen partial pressure. Values are encumbered with 5% error resulting from class B solar simulator. 93
Table 4.11: Calculated transmittance of FTO glass and samples with BL obtained at t_d = 30 min and under different oxygen partial pressure. Values are encumbered with 5% error resulting from class B solar simulator. 95
Table 4.12: Calculated transmittance of FTO glass and samples with BL obtained at t_d = 30 min and under different oxygen partial pressure. Values are encumbered with 5% error resulting from class B solar simulator. 97
Table 4.13: Results from electrical resistance measurement for the bare FTO substrate and samples with BL obtained at p_{O_2} = 0.26 mTorr; including errors of estimation and deposition conditions. 106
Table 4.14: Results from electrical resistance measurement for the bare FTO substrate and samples with BL obtained at t_d = 30 min; including errors of estimation and deposition conditions. 110
Table 5.1: List of fabricated DSSCs with BL, which photocurrent-voltage characteristic was tested. 120
Table 5.2: Photovoltaic parameters of best-performing DSSCs without and with BLs deposited under the oxygen partial pressure of 0.26 mTorr. The measurement was taken under illumination of AM1.5 simulated solar light (100 mW/cm^2). 125
Table 5.3: Averaged efficiencies of illuminated sets of DSSCs without and with BLs deposited under the oxygen partial pressure of 0.26 mTorr including errors of estimation and deposition conditions. 134
Table 5.4: Averaged short-circuit current densities of illuminated sets of DSSCs without and with BLs deposited under the oxygen partial pressure of 0.26 mTorr including errors of estimation and deposition conditions. 136
Table 5.5: Averaged open-circuit voltages of illuminated sets of DSSCs without and with BLs deposited under the oxygen partial pressure of 0.26 mTorr including errors of estimation and deposition conditions. 138
Table 5.6: Averaged fill factors of illuminated sets of DSSCs without and with BLs deposited under the oxygen partial pressure of 0.26 mTorr including errors of estimation and deposition conditions. 140

Table 5.7: Photovoltaic parameters of best-performing DSSCs without and with BLs deposited at deposition duration of 30 minutes. The measurement was taken under illumination of AM1.5 simulated solar light (100 mW/cm^2). 143
Table 5.8: Averaged efficiencies of illuminated sets of DSSCs without and with BLs deposited at deposition duration of 30 minutes including errors of estimation and deposition conditions. 150
Table 5.9: Averaged short-circuit current densities of illuminated sets of DSSCs without and with BLs deposited at deposition duration of 30 minutes including errors of estimation and deposition conditions. 153
Table 5.10: Averaged open-circuit voltages of illuminated sets of DSSCs without and with BLs deposited at deposition duration of 30 minutes including errors of estimation and deposition conditions. 155
Table 5.11: Averaged fill factors of illuminated sets of DSSCs without and with BLs deposited at deposition duration of 30 minutes including errors of estimation and deposition conditions. 157

Chapter 1: Introduction

1.1 Motivation and objectives

Constantly growing demand for electrical energy on a global scale progressively devours fossil-fuel reserves. Also massive production of greenhouse gases has strong impact on the environment on the earth. This creates a need to search for alternative energy resources. Harvesting the energy from sunlight is a very appealing notion as the sun supplies the surface of the earth with over a hundred thousand terawatts. However, harnessing solar energy and converting it into electrical or chemical energy at low cost remains a huge challenge that is an incentive for research in the field of solar cells.

Solar cells are photovoltaic devices whose principle of operation is based on the photovoltaic effect, which was discovered by A. E. Becquerel in 1839 (Becquerel 1841). The photovoltaic effect is the process of creating a voltage in the solar cells upon its illumination; thus sunlight is directly converted into electricity. Although this phenomenon was observed in an electrochemical cell, construction of most modern solar cells is based on an idea of p-n junction that was invented in Bell Laboratories 1940 while studying on silicon crystals. Development of modern photovoltaic devices that are based on silicon p-n junction was initiated by making silicon solar cells of 6% efficiency in 1954 (Chapin et al. 1954). At the same time there was a constant progression in photography that was focused on the photosensitization process. Knowledge of the fields of photovoltaics and photography has merged and led to the development of another type of photovoltaic devices in which light absorption occurs at deliberately introduced sensitizers, like in photography, rather than at p-n junctions. As a result, it was testified in the late 1960s that organic dyes adsorbed on oxide electrodes of electrochemical cells manage to generate electricity upon illumination (Gerischer et al. 1968). Soon after, it was illustrated that titanium dioxide (TiO_2) semiconductor electrode of electrochemical cell

under illumination allows water splitting via its photodecomposition (Fujishima & Honda 1972). Afterwards, it was demonstrated that use of mesoporous TiO_2 semiconductor that increased surface area is coated with charge-transfer dye molecules for light harnessing enables the photoelectrochemical cell to improve the energy conversion efficiency (O'Regan & Grätzel 1991). Photovoltaic devices of this design are known as dye-sensitized solar cells and, since the improvement of their efficiency, they have attracted a good deal of attention as alternatives to p-n junction solar cells. Main advantages of dye-sensitized solar cells are ease of fabrication at low cost, inexpensive materials, and relatively good efficiency. However, dye-sensitized solar cells possess two weaknesses which need to be addressed in order to become fully competitive with other types of solar cells. One drawback is long-term stability, and the other is the conversion efficiency, which is not competitive enough.

The performance of dye-sensitized solar cell is controlled by photoinduced electrochemical reactions and their derivatives. However, some of these reactions are disadvantageous to efficient energy conversion thus their occurrence should be minimized. One of these unwanted reactions is recombination of photoelectrons at the interface of transparent conductive oxide / electrolyte. Prevention of this reaction can be achieved through appropriate design of the cell and a method to do so is incorporation of a thin layer that will block the back-transfer reaction of the photoelectrons. Such a layer is called a blocking layer and is applied at the interface of the transparent conductive oxide / electrolyte. This approach has been proved effective in dye-sensitized solar cell based on liquid electrolytes (Cameron et al. 2004), as well as in those with solid-state electrolytes (Jennings & Peter 2007), including perovskite solar cells (Hwang & Yong 2016). Research on preventing this electron recombination process has recently brought about new efficiency records in dye-sensitized solar cells.

There are several requirements for the ideal blocking layer. The blocking layer should be very thin, about a hundred of nanometres or less, compact and pinhole-free. Therefore, most favoured methods are bottom-up deposition

techniques which can be precisely controlled. Among many techniques that meet these requirements to a greater or lesser extent (Góes et al. 2012; Cameron & Peter 2003), there is pulsed laser deposition (Lee et al. 2009). Materials for good blocking layers are usually searched among metal oxides, such as ZnO, Nb_2O_5 (Woo & Jang 2013), HfO_2 (Bills et al. 2011), including the most widely studied TiO_2 (H.-J. Kim et al. 2012). That has also been studied as doped material, for instance Nb-doped TiO_2 (Lee et al. 2009).

The greatest advantage of deposition of thin layers via pulsed laser deposition is that it enables the stoichiometric transfer of almost any material from target to substrate as well as facilitates to supply reactive gases in order to change the composition of the deposited film. It is also known that it provides good adhesion of the film to the substrate and good mechanical rigidity (György et al. 2005). Moreover, it enables easy control of deposition conditions, such as operating pressure, substrate temperature, deposition atmosphere (vacuum, inert gases or reactive atmosphere), and use of variety of targets and substrate materials. Additionally, the use of lasers with different wavelengths is also possible. This wide range of deposition conditions gives practically unlimited diversity of films that may be deposited. This technique of deposition due to its versatility has been often chosen for the study of deposition of TiO_2 thin films. It has been used mainly due to the wide range of conditions it is possible to control. It has been observed that the composition of TiO_2 thin films, their structure and resulting properties significantly depend on the background atmosphere, substrate temperature as well as on laser wavelength.

Titanium oxide materials are extensively studied mainly due to abundance of its constituent elements in nature and the fact that structure and composition of titanium oxides can appear in several variations, and blends, which possess their own features. For instance, the two basic forms of TiO_2 are rutile and anatase, having bandgaps of 3.0 and 3.2 eV respectively. Another possible form is, for example, titanium monoxide (TiO) that has bandgap energy of approximately 2.0

eV. Therefore, the resulting electrical, optical, photo- and electro-chemical properties of each phase and composition are different.

The diversification of properties of titanium oxides resulting from their structures and compositions makes them suitable for a variety of applications including the use of the titanium dioxide as a blocking layer for dye-sensitized solar cells. However, the investigations in this area appears to only focus on titanium dioxide and the possibility of other titanium oxides as a blocking layer has not been reported. Considering a wide range of possibilities of optical, physical, chemical and electrical properties exist in the titanium oxides, this work was initiated to investigate the performance of titanium oxides as possible blocking layers for dye-sensitized solar cells in a system manner.

The main objective of this study is to prepare titanium suboxide blocking layers using pulsed laser deposition, incorporate them into the structure of dye-sensitized solar cells and evaluate their effectiveness in terms of their influence on the efficiency of the solar cell. The key tasks of this work include:

- Deposition of titanium oxide thin films on suitable substrates
- Characterisation of the electrical and optical properties of deposited thin films
- Study the influence of deposition conditions on the properties of deposited thin films
- Fabrication of dye-sensitized solar cells that incorporate the deposited thin films as blocking layers.
- Characterisation of the conversion efficiency of the fabricated solar cells
- Investigation of the effectiveness of the prepared titanium oxides thin films as blocking layers
- Study the influence of deposition conditions on the properties of fabricated solar cells and determine the optimal deposition conditions for fabrication of the most effective titanium oxide blocking layers.

1.2 Outline of the thesis

Chapter 1

The first chapter provides background information about photovoltaic technology in its historical context. It also presents a background and motivation to the present work, describes the aim and objectives, as well as outlines the thesis.

Chapter 2

The second chapter presents and overviews solar cells technology, beginning with the discovery of photovoltaic effect and historical development of photovoltaic cells and also discuss main aspect of assessment of their solar energy conversion efficiency. It also presents the origin and evolution of dye-sensitised solar cells and discusses their working principle and performance limitations. There is also discussion of the solution to the performance limitation of dye-sensitized solar cells. This chapter also presents basic intimation about pulsed laser deposition and capability of this technique to deposit titanium oxide thin films, which are discussed as well.

Chapter 3

The third chapter explains experimental procedures that were used to deposit titanium oxide thin films and procedure of fabrication of dye-sensitized solar cells. It presents all used materials and devices, including specially designed for this research equipment for screen-printing and holder for thin film deposition. It also details all the preparation procedures.

Chapter 4

This fourth chapter presents all characterisation techniques used in this research for characterisation of structural, optical and electrical properties of deposited. It also shows all the obtained results and presents detailed discussion and conclusions on each measured property of the deposited films.

Chapter 5

This fifth chapter gives description of all characterisation techniques used in this research for characterisation of photovoltaic parameters of fabricated solar cells that include different types of blocking layers. It also shows all the obtained results from the measurements and presents detailed discussion and conclusions on each measured parameter fabricated solar cells.

Chapter 6

The sixth chapter presents the conclusions of conducted experiments and their results and summaries main achievements of this research. It also proposes ideas for future work of this or related studies.

Chapter 2: Background

2.1 Introduction

The aim of this chapter is to present and overview solar cells technology. Description beginnings with the discovery of photovoltaic effect and historical development of photovoltaic cells and also discuss main aspect of assessment of their solar energy conversion efficiency. The origin and evolution of dye-sensitised solar cells and discusses their working principle and performance limitations are also presented. There is also discussion of the solution to the performance limitation of dye-sensitized solar cells. This chapter also presents basic intimation about pulsed laser deposition and capability of this technique to deposit titanium oxide thin films, which are discussed as well.

2.2 Photovoltaics

Human development relies on energy supply, which over the last several centuries is predominantly obtained from fossil fuels. Growing consumption of this non-renewable energy source devours its resources in a rapid rate leading to a global issue, therefore, searching for alternative energy becomes essential. One of the possibilities is harnessing solar energy, which can be directly converted into electrical or chemical energy. The amount of energy from sunlight that reaches the surface of the earth exceeds the present world's consumption by several thousand times. However, harnessing energy from sunlight at low cost still remains a big challenge that has to be tackled to make solar power technology more competitive with other technologies, therefore, this challenge is one of the big motivations for research in the field of solar cells.

Principle of operation of solar cells is based on a photovoltaic effect, which was for the first time observed in 1839 by A. E. Becquerel (Becquerel 1841). The photovoltaic effect is the process of creation of voltage in the solar

cells upon its illumination thus sunlight is directly converted into electricity. The observation of this effect was made with the use of an electrochemical cell. The cell comprised of two platinum or gold plates immersed in an alkaline, acidic or neutral solution. When the cell was exposed unevenly to the light, the electric current passing between the two metal electrodes was detected. This experiment also presented that different types of light sources and materials used to build this electrochemical cell affect the amount of generated current. At present, prevalent utilization of photovoltaic effect is in solid-state devices rather than in the electrochemical.

The first discovery of the photovoltaic effect in solid-state system was made in 1876 by W.G. Adams and R.E. Day (Adams & Day 1877). Material, in which the phenomenon was observed, was selenium which formed as a bar had two platinum wires joined on both ends as contacts. The system generated measureable current when was exposed to the light. Authors attributed current generation to induction of crystallization process of the outer layers of the selenium under illumination. Understanding of semiconductor materials at the time was at its early stage and insight into this process needed time.

Further research on photocurrent generation in selenium led to devising the first thin-film photovoltaic device by C.E. Fritts in 1883 (Fritts 1883). Molten selenium was compressed in between two metal plates made from different materials. As a top plate, a gold leaf was used. Pressing the gold leaf to exposed surface of selenium let contact these two materials and created gold-selenium junction which under illumination was able to generate current.

For the consecutive decades the idea of layered structured photovoltaic devices became prevalent. Successful development of the devices based on selenium was continued (Bergmann 1931) and research of photovoltaic materials extended to new materials, including structures based on thallous sulphide (Nix & Treptow 1939) and copper-cuprous oxide (Grondahl 1933). Researches on the latter incorporated also studies on other structures of photovoltaic cells, for instance, such as described by Grondahl (Grondahl 1933). Finding that the action

of the light to produce photocurrent occurs also at the contact between the copper and the oxide initiated an idea to let light strike the oxide and reach the junction as effortlessly as possible.

In the second decade of twentieth century, J. Czochralski invented a method of crystal growth, named Czochralski process, to obtain single crystals (Czochralski 1918). This process was then employed in production of high-purity silicon wafers that contributed to development of electronic industry. Study on silicon crystals by R. S. Ohl, in Bell Laboratories, lead in 1940 to invention of p-n junction, that is formed at the contact between p-type and n-type semiconductors, and discovery that shining the light on the p-n junction in silicon allows producing significant electrical current (Riordan & Hoddeson 1997). Based on this discovery, the first silicon solar cell was made and then patented in 1941 as a light sensitive device (Ohl 1941). Further improvement of the concept allowed in 1954 making silicon solar cell with 6% efficiency which initiated development of modern photovoltaic devices that are based on silicon p-n junction (Chapin et al. 1954).

In 1956 the first photovoltaic device made of GaAs was reported as a result of research on new materials for p-n junctions made of III-V semiconductors, compounds composed of elements form group 13 with 15 (Jenny et al. 1956). Progress in understanding the physics of semiconductors led to further development of solar cells technology. If bandgaps between p-type and n-type semiconductors are equal, the p-n junction is defined as a homojunction, whereas if they are unequal, it is defined as heterojunction. Understanding the concept of homojunction and heterojunction triggered a burst of progress of high-efficiency solar cells (Alferov et al. 1971).

Contemporaneously there was a continual development in technology of photography which was focused on photosensitization process. Knowledge of the fields of photography and photovoltaics has come together and fructified with photoelectrochemical cells in which light absorption process occurs at deliberately introduced sensitizers, like in photography, rather than at p-n junction. In the early

1970s it was testified that titanium dioxide (TiO_2) semiconductor electrode of electrochemical cell allows water splitting upon illumination via its photodecomposition (Fujishima & Honda 1972). Subsequently, it was illustrated that use of mesoporous TiO_2 semiconductor that increased surface area and coating it with charge-transfer dye molecules for light harnessing enables the photoelectrochemical cell to boost the energy conversion efficiency (O'Regan & Grätzel 1991). Photovoltaic devices of this design are known as dye-sensitized solar cells and since the enhancement of their performance and conversion efficiency, they have attracted a great deal of attention as alternative to p-n junction solar cells.

2.3 Solar energy conversion

Every material in the presence of light exhibits its optical properties which result from the interaction of electromagnetic radiation with matter. Light reflection, transmission and absorption are one of the basic optical phenomena observed in materials. Light absorption causes excitation of an electron or other charge carrier to a higher-energy state via the transfer of energy from a photon to a charge carrier. Charge separation, occurring after the photoexcitation, leads to creation of electronic potential, also called photovoltage. Photoexcitation may occur only when the photon has a sufficient energy to overcome a potential barrier for excitation of the charge carrier. The potential barrier is an intrinsic property of the material. Situation when the excited charge carrier directly enters another material is called the photovoltaic effect. Then the situation when the excited charge carrier is ejected out of the material into a vacuum space is called the photoelectric effect.

The photoelectric effect, as the ability to eject free charge carriers from the material under light illumination, was discovered by H. Hertz in 1887 (Hertz 1887). The observation was performed with the use of two oppositely charged electrodes in a vacuum, which upon illumination create electric spark between them. The generation of the spark was easier for shorter wavelength of

electromagnetic radiation in the ultraviolet region of the spectra. Deeper understanding and explanation of this effect was proposed by A. Einstein in 1905 (Einstein 1905). Clarification concludes that a beam of light is a collection of discrete wave packets rather than a wave propagating through space. These quantised packets, called photons, carry energy which consequently is quantised as well and proportional to the frequency of the electromagnetic radiation. Quanta of energy carried by photons move without being divided and can only be emitted or absorbed as a whole.

The first estimation of maximum power conversion performance for photovoltaic devices was proposed by M. Prince (Prince 1955). The evaluation was derived from research on silicon based solar cells and was expressed as a maximum converted power density as a function of semiconductor's bandgap. It presents that the optimum bandgap is between 1.1-1.5 eV with generated power density of about 24 mW/cm^2 under bright sunlight with power density of 108 mW/cm^2 that gives about 22.2% conversion efficiency. Profound understanding of photovoltaic phenomenon from quantum mechanics point of view let also evaluate the maximum theoretical efficiency of photovoltaic devices. One of the first estimation of potential solar energy conversion efficiency in this way was made in 1955 by D. Trivich and P. Flinn (Landsberg & Badescu 2000). The ultimate conversion efficiency was predicted to be about 44% and based on theory that photons cannot be absorbed by a material when their energy is lower than bandgap energy of the material and only equivalent of this energy can be utilized from higher energy photons. The estimated conversion efficiency does not include energy losses due to re-radiation from photovoltaic device, which is inevitable. Fact that every matter which temperature is above absolute zero emits blackbody radiation was taken into account while calculating the limit of photovoltaic device efficiency by W. Shockley and H. Queisser (Shockley & Queisser 1961). The calculation includes also loss of energy conversion due to radiative recombination that occurs for any photon energies exceeding bandgap energy of a solar cell. These main factors and other considerations resulted in estimating the maximum

efficiency of 30% for an energy bandgap of 1.1 eV and nearly the same efficiency for consecutive bandgaps unto 1.5 eV. The results are established on assumption that the sun is a blackbody at temperature 6000 K which gives incident power about 158 mW/cm^2 and there is no loss of radiation within a medium transferring it to the photovoltaic device. Furthermore, the temperature of the device is assumed to be 300 K. Nowadays it is well known that spectral energy distribution of the sunlight at the surface of the Earth is strongly affected by Earth's atmosphere thus it differs from spectral distribution of blackbody radiation at 6000 K. Therefore currently solar spectral irradiance at the Earth's surface is precisely defined by the international standard and its Hemispherical Tilted Irradiance, often named as AM 1.5G, is now used for vast majority of studies and calculations in photovoltaic technology (Gueymard 2006). The total power density derived from the standard is 100 mW/cm^2. The solar cell temperature of 298.15 K (25°C) is now used as corresponding to standard conditions. Considering these conditions and assuming radiative losses from the front and rear side of the cell, the maximum power conversion efficiency based on Shockley and Queisser calculations is higher than the originally forecasted and reaches 32.23% for semiconductor with bandgap of 1.1 eV and the utmost 33.16% for bandgap of 1.34 eV (Rühle 2016).

2.4 Dye-Sensitized Solar Cells

Dye-Sensitized Solar cell (DSSC) is a low-cost solar cell belonging to second generation photovoltaics, which typical power conversion efficiency is between 10% and 15%. DSSC is a photoelectrochemical system whose principle of operation is akin to the process known in nature as photosynthesis. In the late 1960s it was testified that organic dyes adsorbed on oxide electrodes in electrochemical cells are able to generate electricity under illumination (Gerischer et al. 1968). Then, in the early 1970s it was demonstrated that shinning the light upon titanium dioxide (TiO_2) semiconductor electrode of electrochemical cell

allows water splitting via its photodecomposition (Fujishima & Honda 1972). Thereafter, it was illustrated that use of high-surface-area mesoporous TiO_2 semiconductor in order to increase its surface area and coating it with charge-transfer dye molecules for light harvesting, enables the photoelectrochemical cell to improve the energy conversion efficiency (O'Regan & Grätzel 1991). The latter design of the photovoltaic device has attracted a good deal of attention as an alternative to conventional solar cells. Their main advantages are low cost of materials, ease of fabrication at reasonable price, and relatively good efficiency (Ito et al. 2008; Chiba et al. 2006). Moreover, it has been also proved that large scale DSSC modules are able to produce yearly more electricity than conventional silicon modules due to their ability to efficiently convert energy of diffused light (Toyoda et al. 2004). Additionally, it was also shown that the performance of DSSCs at moderate temperatures, up to 50°C, can be even enhanced at full sunlight (Berginc et al. 2007). Another practical advantage of DSSCs is possibility to fabricate them on flexible substrates (Miettunen et al. 2013; Dürr et al. 2005).

The typical dye-sensitized solar cell (O'Regan & Grätzel 1991; Hagfeldt & Grätzel 2000; Grätzel 2001; Jena et al. 2012) is composed of a working electrode (WE), also known as a photoelectrode, a counter electrode (CE) and electrolyte. The working electrode consists of a porous nanocrystalline layer of titanium dioxide (TiO_2) particles applied on a conducting substrate, that is transparent conductive oxide (TCO) coated glass (see Figure 2.1). The layer of the titanium dioxide particles is sensitized with a monolayer of small dye molecules that are responsible for light absorption. The counter electrode consists of another conducting substrate which conductive side is covered with a layer of platinum-based catalyst. The electrodes are facing each other and are physically separated by a ring-shaped thermoplastic spacer. The gap between the electrodes is filled with an electrolyte solution that permeates into the porous structure of TiO_2 layer and connects the electrodes electrically. This architecture differs from the design of the traditional silicon solar cells and performs as photoelectrochemical system

thus its principle of operation is somewhat different than in typical p-n junction solar cells. The main difference is that in the DSSCs the element which is responsible for light absorption, the dye, is separated from the element responsible for charge carrier transport. In traditional p-n junction silicon-based solar cells the silicon provides two functions that are acting as the source of photoelectrons and providing the electric field for charges separation, and conducting a current.

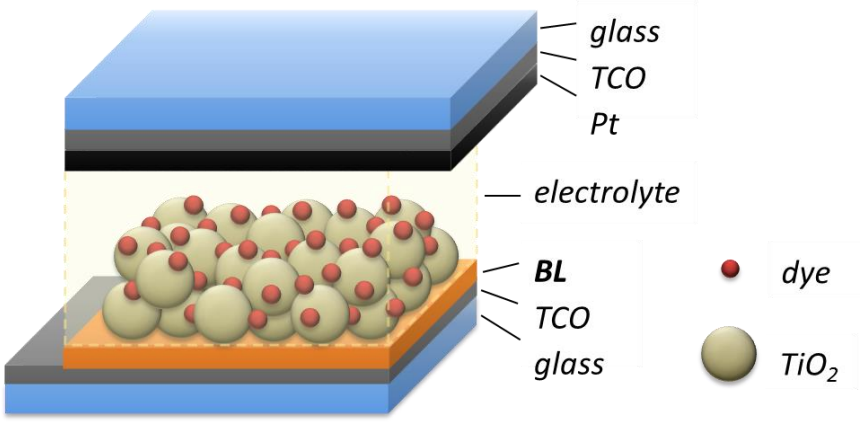

Figure 2.1: Diagram of typical dye-sensitized solar cell.

In DSSCs (Grätzel 2009; Gong et al. 2012; Peter 2007) under light illumination conditions light passes through the glass and conductive coating and reaches the monolayer of the dye molecules where it is absorbed. The dye molecules by absorbing the photons form sunlight excite to higher energy level creating excitons. These usually dissociate at a heterointerface to generate electrons and holes in adjacent phases. At this point, the photogenerated electrons are injected into the conduction band of the TiO_2 and the holes into the electrolyte. The injected electrons diffuse through interconnected network of semiconducting oxide nanoparticles to reach the TCO layer where are transferred further to a contact with an external circuit. Meanwhile, the electrolyte solution which contains a redox couple, usually iodide/tri-iodide, regenerates the dye

molecules by reducing them back to their original oxidation state. In this process iodide ions transform into tri-iodide ions. The oxidized component of the electrolyte diffuses to the counter electrode where it is reduced back to iodide ions by receiving electrons that migrated through the external load and were transferred from the TCO layer through the platinum coating. Transfer of holes in solar cells can be always described as the transfer of electrons in the opposite direction.

Efficient conversion of light into electrical energy in DSSCs (Snaith 2010; Durrant et al. 2004; Ito et al. 2008; Tétreault & Grätzel 2012; Peter 2011) depends on several factors, much like in other solar cells. The first important factor is efficient light absorption. For this reason dye molecules should absorb all photons in visible and near infrared region of solar spectrum. In reality dyes strongly absorb only part of this spectrum. Among many kinds of dye molecules that have been developed, the most common ones are ruthenium based metal complex dyes (e.g. N3, N719, N749, Z907). In order to increase light harvesting and achieve efficient charge carrier pair generation, a fair amount of dye molecules have to be present inside the cell and adsorbed on large surface of charge conducting material. For this reason, nanocrystalline porous semiconducting film is used as a scaffolding with high internal surface area available for substantial adsorption of the dye molecules. Additional approach for enhancement of light harvesting is use of light scattering layer. This layer is porous and is applied on top of the nanocrystalline layer before sensitization and is usually composed of the same semiconducting material but with particles that have ten times greater diameter. This layer scatters the incident light within the photoanode efficiently increasing its absorption by dye molecules. Injection efficiency of photogenerated electrons from dye into semiconducting film is determined by several factors, including the potential difference between the lowest unoccupied molecular orbital of the dye and conduction band edge of the semiconductor. Essentially the semiconductors used in working electrodes of DSSCs are wide band gap metal oxides like TiO_2, ZnO SnO_2, Nb_2O_3 etc. Among all of these materials, TiO_2 is the most common

due to its properties and availability. Another factor important for the efficiency of DSSCs is efficiency of the photogenerated charge transport in the porous TiO_2 film that is usually determined by the electron diffusion length. If the latter exceeds the thickness of the porous titania film, collection efficiency of the photoelectrons at TCO becomes significantly decreased. Therefore, typical thickness of the TiO_2 layer, including light scattering layer, is about 16 μm. The dye should be efficiently regenerated after its electron injection into the TiO_2 layer, which is performed by the electrolyte. After that, the oxidized component of the electrolyte should quickly diffuse to the platinum coated counter electrode where it is reduced. Therefore, role of the electrochemical properties of the electrolyte is also important in terms of dye-sensitized solar cells efficiency. Many different electrolytes have been tested, including their different physical state, and based on that, they can be classified into three groups – liquid electrolytes, solid electrolytes and quasi-solid electrolytes. Most of the DSSCs are based on the liquid electrolytes and among them commonly used electrolytes are those with redox couple where the most widely used is I^-/I_3^- couple. The distance for the electrolyte components to diffuse during the cell operation is dictated by the inter-electrode separation which typically is around 40 μm. The oxidized component of the redox electrolyte should be reduced quickly at the counter electrode to efficiently complete the cycle of charge transport inside the cell. To meet this requirement, the surface of the counter electrode is activated using a catalyst. The most common catalysts used for counter electrode preparation are platinum and carbon. In order to efficiently pass the photogenerated charge carriers through the external circuit, well conducting and transparent material is needed for coating the glass with the transparent conductive oxide layer. The most widely used materials for the TCO are fluorine-doped tin oxide (FTO) and indium tin oxide (ITO).

Although dynamic development of dye-sensitized solar cells and increased research on their components over the last two decades, there is still variety of problems and challenges to tackle in order to fabricate high efficient DSSCs, especially on industrial scale. One of the biggest problems is related with

photosensitizer. There is still considerable amount of photons of solar spectra which are not efficiently absorbed or not absorbed at all. Moreover, stability of the photosensitizer species is also challenging. Dye molecules should be stable enough to survive 20 years of exposure to sunlight without tangible degradation. However, many dyes used in DSSCs are not stable chemically and thermally and are not photostable to ultra violet light. One of new types of sensitizers used in DSSCs are semiconductor quantum dots. These are inorganic nanoparticles with size dependant absorption spectra. Their physical and optical properties can be controlled by changing their size and shape. They are sometimes used as co-sensitizers along with other dyes. DSSCs based on quantum dots have the potential to increase the maximum attainable thermodynamic conversion efficiency of solar photon conversion much above the Shockley-Queisser limit (Kongkanand et al. 2008; Nozik 2005). Another new type of sensitizers that recently boosted the efficiency of DSSCs are perovskites. These perovskite structured compounds are most commonly hybrid organic-inorganic lead or tin halide-based materials. Use of these materials have recently revolutionised the DSSC technology and already became separate emerging photovoltaic technology, known as perovskite solar cells. Efficiency of these cells have increased from 3.8% in 2009 (Kojima et al. 2009) to 22.1% in 2016 (NREL 2016). On the other hand, a huge challenge for perovskite solar cells is their short-term and long-term stability. These cells are very instable to several environmental conditions and suffer from moisture and oxygen degradation (Bryant et al. 2016), thermal degradation (Juarez-Perez et al. 2016) and photo degradation under ultraviolet light (Matteocci et al. 2016).

Long-term and high-temperature stability issues in DSSCs are also related with commonly used liquid electrolytes. Organic liquid electrolytes are highly volatile therefore cells experience degradation by solvent evaporation and iodine sublimation. Solution to this problem is replacement of the volatile electrolyte with solid-state or quasi solid-state hole conductor, such as ionic liquid electrolytes (Yamanaka et al. 2007; Wang et al. 2005), p-type semiconductors

(O'Regan & Schwartz 1998; Smestad et al. 2003) and polymer electrolytes (Wang et al. 2003; Kang et al. 2005). Replacement of liquid electrolyte with solid electrolyte creates a new problem that is poor pore filling of photoanode by the electrolyte, high recombination reactions and ineffective contact with the counter electrode. Furthermore, the carrier mobility in solid state or quasi-solid state electrolytes is lower as compared to liquid electrolytes.

Architecture of DSSCs consists of many interfaces through which photoelectrons pass during the cell operation. Electron transfer kinetics at theses points are critical to the performance of DSSCs (Hagfeldt & Grätzel 2000), therefore, proper interface engineering is another crucial aspect. Problems quite often occurring at the interfaces are recombination reactions where photogenerated electrons undergo unwanted back-reactions leading to loss of energy absorbed from photons. Details of these reactions and solutions for the problem, such as blocking layers, are described in the following section.

2.5 Blocking Layers

Competition between transport of photogenerated charge carriers and recombination reactions is an important factor that influences cells efficiency. The photoelectrons which undergo recombination reactions are those from conduction band of the TiO_2 and from the FTO. The former electrons may recombine with oxidized dye molecules at the TiO_2 layer / dye molecule interface (Patrocínio et al. 2009; Grätzel 2005). However, the recombination reaction at this interface is negligible. Nonetheless, it can be further minimized by surface treatment of the porous TiO_2 with $TiCl_4$ before sensitization (O'Regan et al. 2007; Sommeling et al. 2006) or by applying core-shell double structured electrodes (Diamant et al. 2004) which was pioneered by Zaban in 2000 (Zaban et al. 2000) using Nb_2O_5 as shell material. Also use of co-adsorbents (Zhang et al. 2005; Zhang et al. 2007) can effectively suppress this recombination by eliminating dye-vacant sites on the

nanoporous TiO_2. The effect of co-adsorbents in DSSCs was for the first time observed in 1993 (Kay & Graetzel 1993).

The injected conduction-band photoelectrons may also recombine with redox species in the electrolyte. This recombination may occur either directly from the conduction band or via surface states (Peter 2007). However, it was found that reaction via surface states is not important (Bailes et al. 2005; Cameron & Peter 2005; Cameron et al. 2005). It was suggested (Peter 2007) that selectively blocking the surface of the nanocrystalline TiO_2 may lead to increase of photovoltage in DSSCs. Another approach to suppress the recombination at the porous TiO_2 / electrolyte interface is optimization of composition of liquid electrolyte by using additives. One of the most frequently used additives is 4-*tetr*-butyl-pirydine (TBP) (Huang et al. 1997) which can greatly improve an open-circuit voltage of DSSCs. Other very important additive is guanidinium (Kopidakis et al. 2006) because guanidinium cations slow down the recombination and cause the band edge of the conduction band of the porous TiO_2 to move downward which results in improvement in the open-circuit voltage.

The porous interface between the FTO substrate and the TiO_2 layer in the photoelectrode also acts as the recombination site. Charge recombination at this interface occurs due to the physical contact between the FTO surface and the electrolyte which permeates the mesoporous structure of the TiO_2 layer. In this case, photoinjected electrons in the FTO can react with the I_3^- ions being thereby directly transferred to the electrolyte at the FTO / electrolyte interface, without leaving the cell to perform work in an external circuit. The leakage sites at the FTO / electrolyte interphase exist especially when highly viscous redox species, like ionic liquid iodides or solid electrolytes infiltrate into the porous interface. The problem with the recombination at the interface can be solved by applying a compact oxide layer on the FTO substrate before deposition of the semiconductor mesoporous layer. This compact layer physically blocks the reaction of the photoinjected electrons with I_3^- ions or holes of the electrolyte and is often called the blocking layer (BL) (see Figure 2.1).

The blocking layer made of compact TiO_2 layer had been introduced in DSSCs at the interface of FTO and mesoporous TiO_2 layer in the early 1990s. It was usually fabricated either by electrodeposition (Kavan et al. 1993) or by spray pyrolysis (Kavan & Grätzel 1995). That type of blocking layer did not have strong influence on conversion efficiency of DSSCs and only some groups studied the interface of FTO / TiO_2 in order to establish models of DSSCs (Pichot & Gregg 2000; Levy et al. 1997; Zaban et al. 1997; Cahen et al. 2000; van de Lagemaat et al. 2000; Fabregat-Santiago et al. 2003). Before the early 2000s some research has also been done to characterise and investigate the effectiveness of the TiO_2 blocking layer on conversion efficiency (Gregg et al. 2001; Ito et al. 2005; Peng et al. 2004; Hore & Kern 2005). Cameron et al. (Cameron & Peter 2003; Cameron & Peter 2005; Cameron et al. 2005) studied the TiO_2 blocking layers from reaction mechanism of back-electron standpoint. They used electrochemical impedance spectroscopy and simulations and found that the blocking layers could considerably have an impact on current decay and on the transient photovoltage. In 2005 Ito et al. (Ito et al. 2005) found that the TiO_2 compact layer can greatly suppress the dark current in DSSC. Research done by Abdullach et. al. (Abdullah & Rusop 2013; Abdullah et al. 2013) on a graded index TiO_2 compact layer was focused not only on elechtrochemical influence of the BL on the performance of the DSSC but also paid attention to the optical properties of the BL, such as refractive indices in the multilayer structure. They highlighted that tailoring the refractive index in the multilayer structure is needed to minimise the reflection loss, which results in noticeable change in spectral response of the dye.

Xia et. al (Xia, Masaki, Jiang, Wada, et al. 2006) also studied different oxides, like Nb_2O_5, by the spray pyrolysis method and found that these materials can work as the blocking layer as well. Therefore, they developed another technique for deposition of the Nb_2O_5 BL which was magnetron sputtering (Xia et al. 2007c) and showed that it has good reproducibility, allows for homogenous coverage of the substrate and has capability for large-scale application. It was also found that only very thin film of about 3 – 5 nm, that gives a trace amount of

Nb_2O_5, is needed to work well as the blocking layer and, on the other hand, thicker layer can result in poor performance (Xia et al. 2007b). This was ascribed to complete diffusion of Nb_2O_5 to the FTO and the mesoporous TiO_2 layer during calcinations process. Another material and deposition technique used for the blocking layers was Nb-doped TiO_2 thin film deposited on the FTO by pulsed laser deposition (Lee et al. 2009). It was reported that this layer can be bifunctional, as it works not only as the blocking layer but also as an ancillary TCO layer.

So far, the most studied material for the blocking layer is TiO_2 (H.-J. Kim et al. 2012) and it seems to be the most suitable candidate for several reasons. Except its function as the layer that effectively retards the recombination reaction of photoelectrons at the TCO / electrolyte interface, it also features excellent match to mesoporous layer that is commonly made of TiO_2 naonparticles. It is easy to be deposited as a compact film and it is the abundant material thus it can be easily used on industrial scale. There exist various types of materials that have been tested as alternative materials for the TiO_2 blocking layer. They are usually semiconducting or insulating metal oxides, such as aforementioned Nb_2O_5 (Woo & Jang 2013; Xia et al. 2007a), ZnO-based compact layer (Woo & Jang 2013; Abdullah et al. 2013), BaCO3 (Wu et al. 2007), CaCO3 (Wang et al. 2006), Al2O3 (Prasittichai & Hupp 2010), HfO2 (Bills et al. 2011), $Mg(OH)_2$ (Peiris et al. 2012). There was also report of thin films of titanium species, expressed as TiOx that can work as the compact blocking layer as well (Xia, Masaki, Jiang & Yanagida 2006). However, study of these novel blocking layers are not well developed yet.

Since the beginning of development of the blocking layers, one of the most used deposition techniques is spray pyrolysis (Cameron & Peter 2003; Xia et al. 2007a), The other very popular method, which is used for the TiO_2 BL deposition, is $TiCl_4$ treatment of the FTO substrate prior application of the mesoporous layer (Ito et al. 2008). Various techniques such as dip-coating (Patrocínio et al. 2009; Hart et al. 2006), magnetron sputtering (Abdullah et al.

2013) using either Ti (Xia, Masaki, Jiang & Yanagida 2006) or TiO_2 target (Goto & Hattori 2006; Góes et al. 2012), electron beam deposition (Manca et al. 2010), chemical vapour deposition (Thelakkat et al. 2002), electrodeposition (Peiris et al. 2012), atomic layer deposition (Bills et al. 2011; Prasittichai & Hupp 2010) and pulsed laser deposition (Lee et al. 2009) have also been used to fabricate the compact blocking layer for the DSSCs. Table 2.1 gives an overview of exemplary blocking layers, their deposition methods and basic performance parameters of the DSSCs with those BL.

Table 2.1: Comparison of several exemplary blocking layer materials, their deposition conditions and basic parameters of the DSSCs that incorporate those BLs. Data retrieved from reference materials.

Cell number	BL material	BL deposition method	BL thickness (nm)	J_{SC} (mA/cm^2)	V_{OC} (mV)	FF	η (%)	references
1	*none*	-	-	9.18	695	0.681	4.30	(Hore & Kern 2005)
2	TiO_2	spray pyrolysis	50	9.35	702	0.720	4.73	
3	TiO_2	spray pyrolysis	75	8.96	696	0.767	4.78	
1	*none*	-	-	8.30	580	0.57	2.8	(Xia, Masaki, Jiang, Wada, et al. 2006)
2	Nb_2O_5	spray pyrolysis	50	7.43	649	0.67	3.2	
1	*none*	-	-	7.91	663	0.66	3.5	(Xia et al. 2007c)
2	Nb_2O_5	RF sputtering	5	9.32	710	0.68	4.5	
1	*none*	-	-	10.16	703	0.61	4.37	(H.-J. Kim et al. 2012)
2	TiO_2	DC sputtering	57	11.61	703	0.60	4.90	
3	TiO_2	DC sputtering	103	13.92	733	0.63	6.42	

4	TiO_2	DC sputtering	201	13.51	729	0.57	5.57	
5	TiO_2	DC sputtering	412	12.93	732	0.53	5.05	
1	*none*	-	-	14.72	681	0.652	6.54	(Lee et al. 2009)
2	TiO_2	PLD	120	15.14	696	0.678	7.14	
3	Nb-doped TiO_2	PLD	110	16.26	714	0.662	7.69	

Use of the blocking layers in DSSCs is important not only for those with I_3^-/I^- redox couple-based liquid electrolytes. In the case of alternative redox electrolytes, such as $Co^{II}(dbbip)_2^{2+}$ (Nusbaumer et al. 2001; Nusbaumer et al. 2003), incorporation of the blocking layer on the FTO substrate has been proved obligatory (Cameron et al. 2004). Explanation is that the rate constant for recombination reaction at the interface of FTO and those alternative electrolytes is much higher than for standard redox electrolyte. The same is true when the liquid electrolyte is replaced with an organic hole conductor such as spiro-MeOTAD in solid-state DSSCs (Krüger et al. 2001; Kruger et al. 2003; Jennings & Peter 2007), including Perovskite Solar Cells (Hwang & Yong 2016).

Over the years of research on the blocking layers, basic requirements for this component of the DSSC have been already established. It is demanded from the BL to be very thin, compact and pinhole-free hence bottom-up deposition techniques that can be precisely controlled are favoured. Among many techniques that considerably meet these requirements, the BL deposited via PLD can also noticeably enhance the performance of DSSC. The PLD technique not only allows meeting all basic requirements for the BL but also one can take advantage of easiness to control deposition conditions and versatility of materials that can be used for the deposition process.

2.6 Pulsed Laser Deposition

First attempts to deposit a film through evaporation of a material by use of a laser as a direct energy source were done shortly after the discovery of the lasers. Initially, both continuous-wave and pulsed lasers were used. In the 1970s and 1980s only limited efforts were carried out using the pulsed lasers. Thereafter, in the late 1980s pulsed laser deposition was rediscovered and popularised as a fast and reproducible technique for growth of oxide films. Over the past 20 years, the pulsed laser deposition technique has been significantly developed and transformed from an academic curiosity to widely applicable technique used for thin films deposition-based research. Nowadays, the PLD became one of the most popular and relatively simple techniques that can be used to deposit variety of materials, from metals, semiconductors, insulators, polymers to even biological materials of nearly any complexity.

The pulsed laser deposition is a physical vapour deposition technique, which deposits films in a vacuum system. In the PLD laser pulse is a direct source of energy, which is focused onto a target material. The target is a source of material which is deposited. Once the laser pulse of sufficient energy density hits the target, a certain amount of material is evaporated or ablated and ejected from the target in a forward directed plume. The role of the ablated plume is to provide the material flux for growth of the film. When epitaxial film growth is performed, ejected material creates the ablation plume which then absorbs the laser and creates plasma. Depending on the complexity of ablated material and desirable volume of the target material which is absorbed, relevant wavelength and duration of laser pulse can be chosen. Diagram of the PLD system used in this study is sown in Figure 2.2.

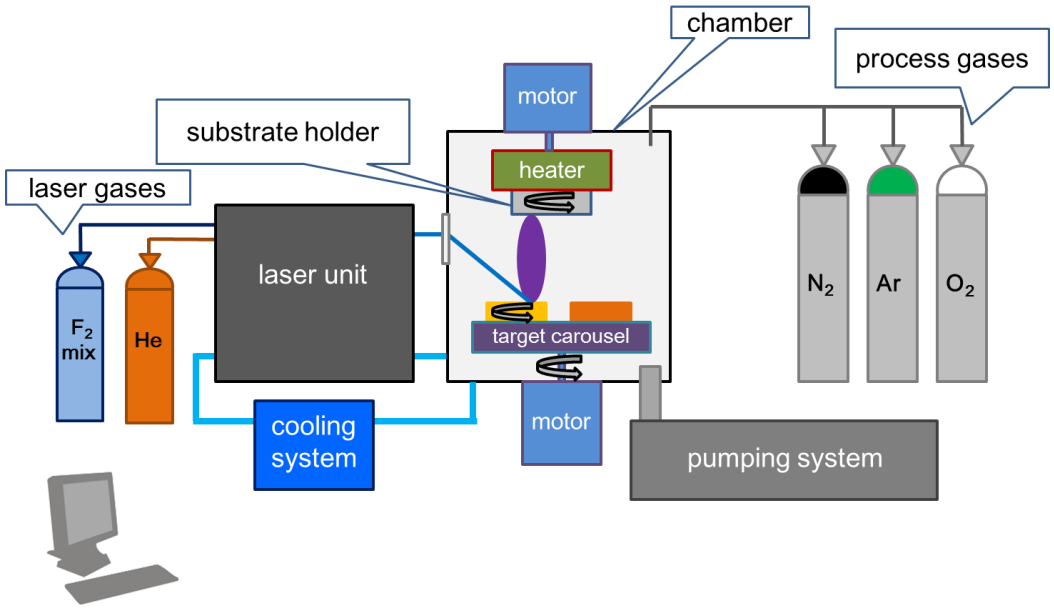

Figure 2.2: Diagram of pulsed-laser deposition system.

The PLD is very attractive method for growth films of complex materials because it features stoichiometric transfer of the target material, hyperthermal reaction between background gas and ablated cations in plasma, and compatibility with background pressures in the wide range of vacuum. Also multication films of many materials can be obtained by the PLD because of flexibility in types and amount of targets used in a single deposition process. In this case desirable film can be produced from a set of targets for each element, or from single stoichiometric target with relevant composition. This is due to nonequilibrium nature of the ablation process. Low laser fluence and/or low absorption of the laser can simply heat the target and eject flux due to thermal evaporation. In this situation, the vapour pressure of the constituents can determine the evaporative flux from multicomponent target. Increase of laser fluence can go beyond ablation threshold that depends on the absorption coefficient of the target. In this case, absorption by the ablated species occurs and thus plasma at the target surface is formed. Because absorption coefficient depends on laser wavelength, vaporization

independent on the vapour pressures of constituent cations occurs when appropriate ablation wavelength and absorbing target material is chosen.

Film growth properties, such as particulate density, epitaxy, phase formation, deposition rate, highly depend on selection of the target for multication materials deposition. Phase of the target material is not very important in contrast to cation stoichiometry. Minimum requirement for target ablation is high optical absorption coefficient of target material at the selected laser wavelength. Wide bandgap ceramic insulators, such as Al_2O_3, have insufficient optical absorption for efficient ablation process when the target consists of single crystal phase. Much more practical in that case is use of polycrystalline target or use of the target that is composed of the constituent cations and anion is supplied by the background gas and utilized in reactive deposition process. Soft materials and biological materials can be used directly as a target or can be embedded in an optically absorbing substance as a matrix, which yields effective ablation process but does not deposit itself.

One of the common problems with PLD deposition process is ejection of micro-size particles during the ablation and deposition of these particles onto the substrate. This can of course influence the quality of the grown film and can be a problem in the formation of multilayer device structure. This problem occurs when the penetration depth of the laser pulse into the target is considerable. It can be solved by using targets that are highly dense and by choosing ablation wavelengths that are strongly absorbed by the target. Also alternative techniques have been developed to solve the issue, such as velocity filters (Pechen et al. 1995), line-of-sight shadow masks (Trajanovic et al. 1997) and off-axis laser deposition (Holzapfel et al. 1992).

Deposition of material by PLD is a highly energetic process thus obtained films have good adhesion to substrate and good mechanical rigidity (György et al. 2005). Moreover, material can be stoichiometrically transferred from target to substrate (György et al. 2005) and vast amount of materials for target and substrate can be chosen considering different types of lasers and conditions for the

deposition. Furthermore, the PLD offers wide range of operational pressures, from medium to high vacuum, deposition in inert gas as well as reactive gas and gases mixtures. Also substrate temperature can be controlled from room temperature to almost 1000^{o}C facilitating heat treatment before or after the process if needed. Taking into consideration possibility of using multiple targets in one process, the PLD technique offers practically unlimited diversity of deposited films.

The capability of the PLD technique and the variety of materials that can be deposited is known since successful grow of in situ epitaxial high-temperature superconducting films in the late 1980s (Inam et al. 1988). The achievement of deposition of complex crystal structures, such as $YBa_2Cu_3O_7$ (Achutharaman et al. 1994) let explore growth of the other complex oxide films, like ferromagnetic oxide $Ba_2Co_2Fe_{12}O_{22}$ (Ohkubo et al. 2001) that can be used in thin-film magnetic device applications. The PLD is successful in deposition of epitaxial heterostructures and superlattices (Yilmaz et al. 1991; Chang et al. 1998; Xu et al. 2000) including the perovskite structure (Christen et al. 1996; Christen et al. 1998). This technique is also capable of creating automatically abrupt epitaxial interfaces (Norton et al. 2000). Another example of possibilities of PLD technique is synthesis of nanomaterials, such as heterostructured one-dimensional semiconductor nanostructures (Wu et al. 2002) that are potentially useful light-emitting devices and thermoelectrics. A different example can be a growth of non-oxide binary compounds, like narrow gap semiconductors (Yu et al. 2013). Interesting application and proof of versatility is deposition of "soft" materials, for instance PTFE (Blanchet et al. 1993) or PMMA (Cristescu et al. 2003) films. Possibility of growing simple oxides as blocking layers in solar cells (Lee et al. 2009; J. Kim et al. 2012) and superlattices like perovskites promise enhancement of attention to this technique in the field of emerging photovoltaic technologies, such as perovskite solar cells.

2.7 Titanium oxide thin films

The most common naturally occurring oxide of titanium is titanium dioxide (TiO_2) also known as titania. It has a wide range of applications, from paints, photovoltaics, cosmetics to food colouring. One of the primary factors affecting properties of titanium oxide-based materials is structure and composition. TiO_2 exists as two main polymorphs, the stable rutile, which is most common form, and metastable anatase (see Figure 2.3). At elevated temperatures, about 600^{o}C, anatase undergoes irreversible transformation to rutile. However, this transformation temperature is not unique and the processes that are involved in this transformation are not well understood (Hanaor & Sorrell 2011). Titanium can appear in Ti-O system in several variations, and their blends, possessing their own characteristic features. For instance, the two basic forms of titania, anatase and rutile, have bandgaps of 3.2 and 3.0 eV respectively thus corresponding light absorption in anatase is initiated at approximately 390 nm while in rutile it is initiated at about 410 nm which was confirmed by Karakitsou et al. (Karakitsou & Verykios 1993). It is also apparent that the light-absorption capacity of the anatase at the near-UV is fairly higher than of rutile (Karakitsou & Verykios 1993). Moreover, measurement of optical transmittance of poorly crystallised/amorphous and well crystallised anatase showed that average transmission in visible and near-infrared spectrum (400 – 1200 nm) is above 85% regardless the crystallinity (György et al. 2005). Then, titanium monoxide (TiO) has bandgap energy of approximately 2.0 eV thus easily absorbs wavelengths in visible range. Furthermore, it is known that anatase has higher photocatalytic activity than rutile phase (Kavan et al. 1996). Additionally, it was shown (Lin et al. 2008) that oxygen vacancies in TiO_2 thin films may change electronic structure of the films and was concluded that adjustment of the Fermi energy level and structure of TiO_2 thin film to align the energy of the flatband potential with respect to specific materials is possible, for example, by controlling the temperature and buffer gas pressure during deposition by PLD technique.

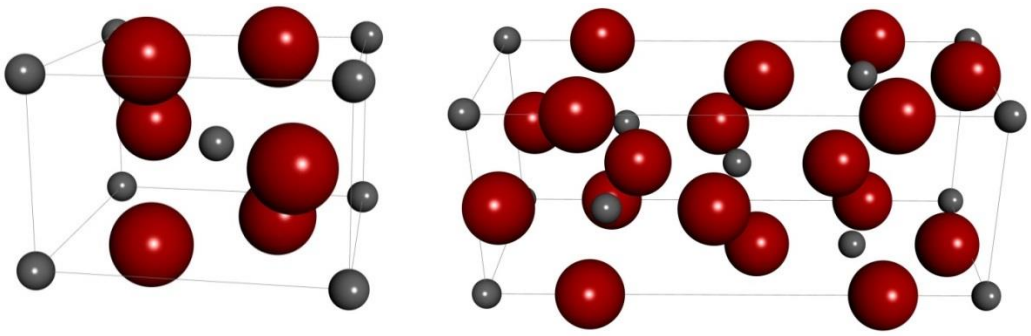

(a) **(b)**

Figure 2.3: Scaled ball models of: (a) Rutile - unit cell parameters: a = b = 4.650 Å, c = 2.970 Å, α = β = γ = 90o; (b) Anatase - unit cell parameters: a = b = 3.807 Å, c = 9.705 Å, α = β = γ = 90o. Titanium atoms are coloured grey, oxygen atoms are coloured red.

Such diversity in properties of TiO_2 related with its form, structure and composition makes it suitable for use in DSSC (O'Regan & Grätzel 1991), gas sensing applications (György et al. 2005), as photocatalyst for water cleavage (Karakitsou & Verykios 1993) or as highly hydrophilic material (Luca et al. 2006).

TiO_2 can be obtained in a form of thin film via many deposition techniques, such as dip-coating (Takahashi & Matsuoka 1988; Sharma et al. 2006), electrostatic sol-spray deposition (Chen et al. 1999), spray pyrolysis (Cameron & Peter 2003), treatment of the substrate by $TiCl_4$ solution (Ito et al. 2008), anodic spark deposition (Meyer et al. 2004), magnetron sputtering (Mardare et al. 2000), chemical vapour deposition (Goossens et al. 1998; Mills et al. 2002), as well as by pulsed laser deposition (Kim et al. 1999; György et al. 2005; Sanz et al. 2009).

Pulsed laser deposition of TiO_2 thin films at various conditions have been studied by numerous researchers. Many of them observed that during the PLD deposition multi-valence Ti species like ionized Ti, TiO species (Kitazawa 2004) as well as Ti and O neutrals are normally created in ablation plume even when TiO_2 target was used (Sanz et al. 2009). Luca et al. (Luca et al. 2006) and Sanz et

al. (Sanz et al. 2009) discussed the relationship between the deposition conditions and the valence states of Ti.

Investigation of influence of ambient pressure in PLD on film crystallinity was done by Kim et al. (Kim et al. 1999). They performed growth of TiO_2 films under various ambient pressures (in the range of 10 - 1000 mTorr) and different kind of gases (Ar, O_2) and found that under low pressures of oxygen (10 - 100 mTorr) one can grow high quality TiO_2 thin film. Effect of buffer O_2 gas and its pressure on deposition of TiO_2 thin films from Ti target was examined by Kitazawa et al (Kitazawa et al. 2004) and it was found that Ti particles presented in ablation plume interacted with buffer O_2 gas and produced TiO molecules that affected structure of formed TiO_2 film. Lin et al. (Lin et al. 2008) in order to prevent formation of TiO or Ti_2O_3 during deposition of TiO_2 used buffer gas (O_2:Ar = 1:1) pressure from 250 to 750 mTorr and obtained slightly reduced to stoichiometric TiO_2 films which was attributed to insufficient oxygen conditions.

György et al. (György et al. 2005) studied impact of substrate temperature in PLD on growth of TiO_2 thin films by carrying out experiments with substrate kept at room temperature or heated at values within 100 - 500^{o}C. It was found that TiO_2 thin films obtained at RT were amorphous, at temperatures between 100 - 300^{o}C were poorly crystallised while at higher than 300^{o}C up to 500^{o}C were well crystallised and corresponding to anatase phase. Similar results were achieved by Kitazawa et al (Kitazawa et al. 2004) were at RT obtained amorphous TiO_2 film, however at 500^{o}C deposited film contained a mixture of rutile and anatase phases. Experiments at higher temperatures were done by Lin et al. (Lin et al. 2008) where TiO_2 films deposited at 600^{o}C and 800^{o}C are mixtures of rutile and anatase but with variation in the rutile/anatase phase ratio. Also roughness of the films was different where for thin film prepared at 800^{o}C occurred to be higher.

Much research has revealed that composition, structure and properties of pulsed laser deposited TiO_2 thin films significantly depend on background atmosphere, substrate temperature and even laser wavelength. It occurs basically due to nature and variety of possible compounds from Ti-O system. György et al.

(György et al. 2005) successfully deposited well crystallised pure anatase phase of TiO_2 at temperatures above 300^oC, at dynamic oxygen pressure of 75 mTorr using laser with wavelength of 248 nm on TiO_2 target. It was proved that structure of thin films changed from amorphous (for deposition on substrate kept at room temperature) to poorly crystallised (for depositions on substrates at temperatures between 100 - 300^oC). It was also observed that preferred orientations of crystals of the films were temperature dependant, while crystal phase was always assigned to anatase despite the fact it is neither the most common nor the most stable phase of TiO_2. Lin et al. (Lin et al. 2008) deposited TiO_2 thin films at higher temperatures and different buffer gas pressures (O_2:Ar = 1:1) and found that the films comprised of both rutile and anatase phases regardless of the substrate temperature (600^oC and 800^oC). However this multi-phase structure showed variation in the rutile/anatase ratio related with buffer gas pressure. The anatase contents increased with increase of the pressure and it was assigned to sufficient amount of oxygen that allowed to obtain lower oxygen vacancy concentration in the films. Consequently, under deposition in buffer gas pressure of 750 mTorr only anatase phase was obtained even at 800^oC that is much higher than anatase to rutile phase transformation temperature in bulk TiO_2. Stoichiometry of TiO_2 films was somewhat reduced for deposition conditions having insufficient oxygen that causes formation of oxygen vacancy. Luca et al. (Luca et al. 2006) reported deposition of TiO_x thin films that consisted of mixture of amorphous TiO_2 and Ti_2O_3 regardless of oxygen pressure (1 - 20 mTorr) and with O:Ti atomic ratio fluctuated in their surface around 1.83 for process at 150^oC. On the other hand, for deposition at 500^oC composition and structure was pressure dependant, where below 20 mTorr films contained mixture of anatase and rutile (dominant phase) along with titanium suboxides while above 20 mTorr the rutile disappeared leaving the anatase (predominant) along with small amount of nanocrystalline suboxides. The samples prepared at higher temperature presented improvement of surface stoichiometry from about $TiO_{1.8}$ to $TiO_{1.9}$. Sanz et al. (Sanz et al. 2009) studied influence of deposition conditions on growth of TiO_2 thin films using

different laser irradiation wavelengths. Results from films deposited under vacuum and above 600^{o}C showed wavelength dependant evolution of phase formation from amorphous (at 532 nm) to rutile (at 355 nm) and to mixed anatase (predominant phase) and rutile (at 266 nm). Deposition at the latter wavelength and under pressure of oxygen (0.38 mTorr) resulted in predominant formation of rutile over anatase, that almost disappeared. For deposition at longer wavelengths (532 and 355 nm) the preferred phase was rutile both in vacuum and under oxygen. Growth of stoichiometric films with good crystallinity was favoured at temperatures above 600^{o}C for longer wavelengths (532 and 355 nm) while for shorter (266 nm) the temperature range was wider (450 – 650 ^{o}C).

Pulsed Laser Deposition is capable of fabricating TiO_2 material in form of amorphous or single phase crystallised film (György et al. 2005), layer with mixed phases (Sanz et al. 2009), reduced to stoichiometric TiO_x thin film (Luca et al. 2006) or as doped compact layer (Lee et al. 2009).

Titanium dioxide thin films are well known in the field of dye-sensitized solar cells technology as good candidates for blocking layers that can effectively retard photoelectrons recombination reactions which can lead to improve of energy conversion efficiency in DSSCs. The other similar materials, especially those which derive from TiO_2 are not broadly studied so far in that area. Many techniques of deposition of blocking layers have been already studied, but not much work has been done yet using pulsed laser deposition. The PLD has been widely used in deposition of variety thin films in many areas. However, according to knowledge of the author of this work, studies on titanium suboxides layers obtained by pulsed laser deposition for application as blocking layers in dye-sensitized solar cells have not been reported yet.

In summary, the overview of harvesting of solar energy by solar cells technology has been done. Discovery and explanation of photovoltaic and photoelectric effects have been presented. Historical development of photovoltaic devices has been reviewed. Main aspects of assessment of solar energy conversion efficiency have been discussed. The origin and evolution of dye-sensitized solar

cells have been presented. DSSCs components, working principle and performance limitations have been explained. Charge recombination reactions, their influence on DSSC performance and means of prevention of these reactions have been detailed. Importance of blocking layer and evolution of the component has been discussed. Deposition methods of the blocking layers and studied materials have been reviewed. Principle of operation of pulsed laser deposition and examples of application of this technique have been presented. Properties of TiO_2, review of techniques of deposition of this material as a thin film, as well as examples of application of TiO_2 thin films have been given. Need for study of titanium oxide thin films obtained by pulsed laser deposition as the blocking layer for dye-sensitized solar cells have been explained.

Chapter 3: Preparation of Ti-O thin films as Blocking Layers and preparation of Dye-Sensitized Solar Cells

3.1 Introduction

This chapter describes the deposition of titanium suboxide thin films by Pulsed Laser Deposition and preparation of Dye-Sensitized Solar Cells incorporating the deposited films as Blocking Layer. Experimental procedures that were used to deposit titanium oxide thin films and procedure of fabrication of dye-sensitized solar cells are explained. The chapter presents all used materials and devices, including specially designed for this research equipment for screen-printing and holder for thin film deposition.

3.2 Deposition of Ti-O thin films by Pulsed Laser Deposition

The thin films for this study were deposited using Pulsed Laser Deposition technique. By virtue of the main objective of this study, the substrate used for films growth was conductive side of FTO glass (TEC 15, Sigma-Aldrich). The FTO glass was fluorine doped tin oxide coated float glass slide of 2.3 mm thickness and surface resistivity of about 13 Ω/sq. The glass slide was firstly cut into size of 40 mm x 36 mm to fit into a substrate holder specially designed for this deposition process (see Figure 3.1 (a)). Next, the cut substrates were thoroughly cleaned via ultrasonic treatment in water with dishwashing liquid and then in isopropyl alcohol for 15 min in each step to remove any organic greasiness and other contamination. This was followed by drying with a hot air blower. Such cleaned substrate was placed on the holder into the deposition chamber. The substrate holder was purposely designed to mask the edge with strip of 3 mm width along both shorter edges of the glass. This allows it to obtain uncoated two opposite edges on coated side of the FTO glass.

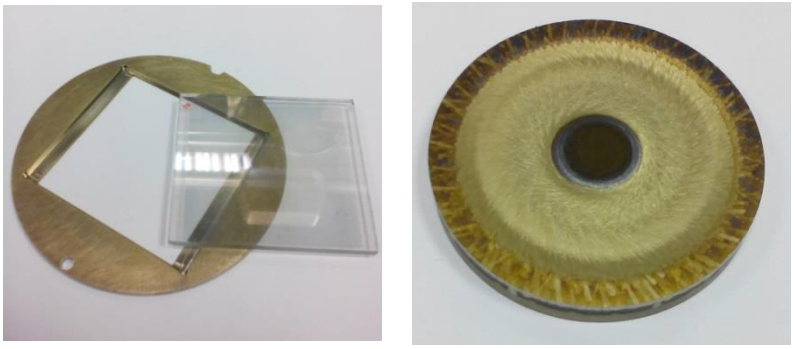

(a) **(b)**

Figure 3.1: Components of PLD system; (a) substrate holder and FTO glass with deposited titanium oxide film, (b) TiO target.

The deposition of the films was performed using apparatus for Pulsed Laser Deposition (PLD2000 Deposition System, PVD Products) shown in Figure 3.2. All films in this study used as BL were deposited from a 2" in diameter TiO target by means of a 248 nm KrF excimer laser at 210 mJ and 15 Hz repetition rate, that delivers 3.15 W power for ablation. The laser spot size at the surface of the target was 9 mm x 1.5 mm, that gives a pulse energy density of about 1.56 J/cm^2. The target-to-substrate distance was maintained at about 75 mm and both target and substrate were rotating during the deposition. Before film deposition, the chamber was evacuated to pressure below 5 x 10^{-7} Torr. Before target ablation, substrate was gradually heated up to the deposition temperature and maintained at this temperature for one hour along with process gases flow adequate to particular deposition experiment. All films were deposited at 300^{o}C and in total pressure of 2 mTorr. The process gases for experiments were argon and/or oxygen. The oxygen serves as reactive gas and a series of six different values of oxygen partial pressures (p_{O_2}) were investigated at fixed deposition duration of 30 min. This was performed to study influence of oxygen partial pressure on properties of deposited film which is described in details in the chapter 4. Also a series of three different values of deposition durations (t_d) were investigated at fixed p_{O_2} of 0.26 mTorr in order to study relation between deposition duration and film thickness and its

influence on deposited films properties. Additional series of three samples at fixed t_d of 480 min and three values of p_{O_2} from first series was performed for compositional measurement at thicker films. All substrates with grown films were gradually cooled down to room temperature under their respective oxygen pressures, directly after the deposition itself. All essential deposition conditions for each series and their samples are summarised in Table 3.1. As films grown symmetrically towards the centre of the substrate, each sample was cut into quadrants of size of 20 mm x 18 mm after deposition. Three out of four quadrants of each samples named as **BL** were later used for making Dye-Sensitized Solar Cells and the remaining quadrants were used for measurements of the films properties. Process flow-chart for the substrate preparation and film deposition is presented in Figure 3.3.

Figure 3.2: Apparatus for Pulsed Laser Deposition.

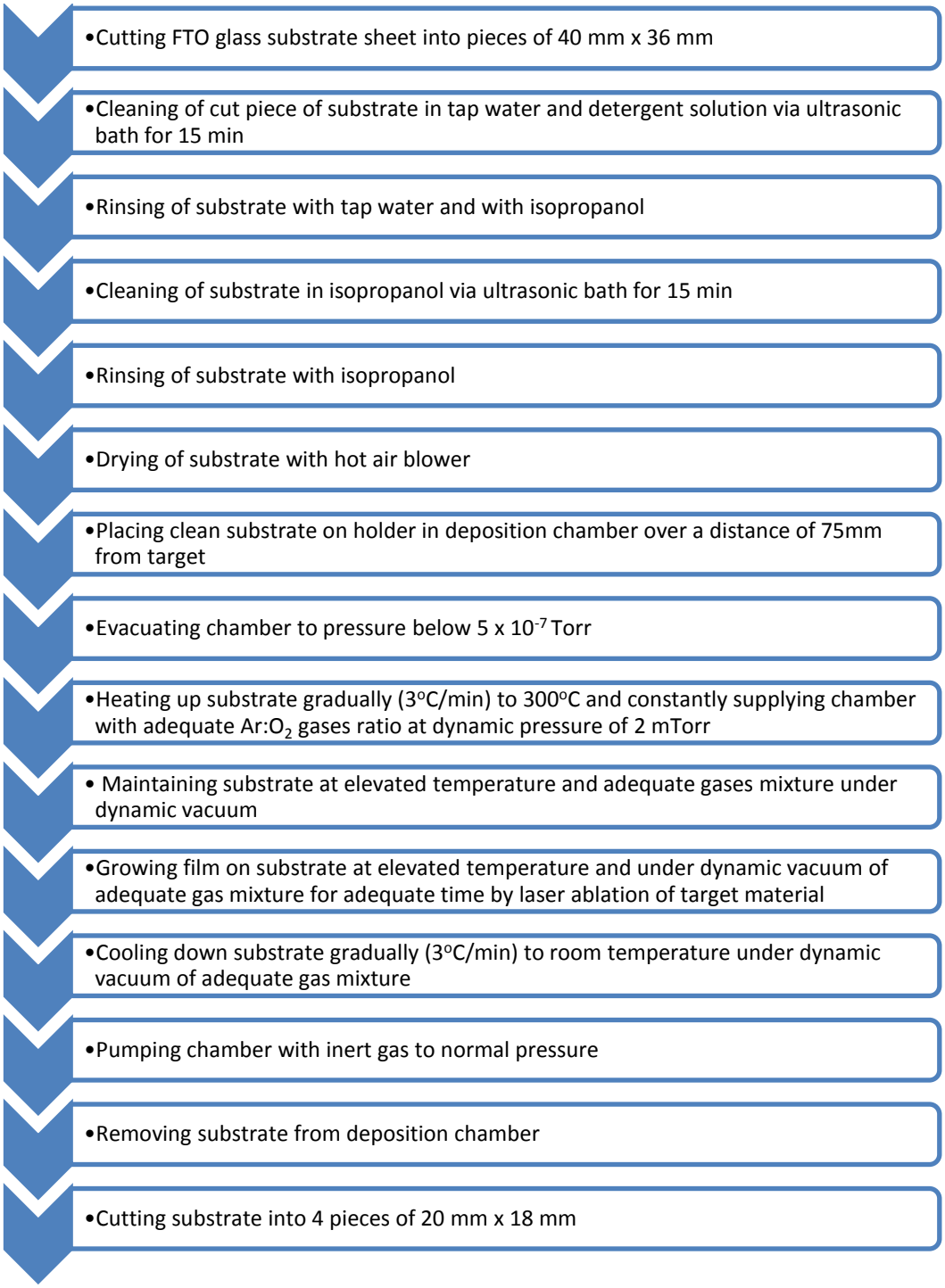

Figure 3.3: Process flow-chart for deposition of titanium oxides thin films on FTO substrate via PLD.

Table 3.1: Basic deposition conditions and name of each sample in each deposition series.

Series No	Samples type name	Total gases pressure (mTorr)	Gases flowrate (sccm)		Oxygen partial pressure, p_{O_2} (mTorr)	Deposition duration, t_d (min)	Substrate temperature (^oC)
			Oxygen	Argon			
1	**BL**30/0.11	2.00	1.15	20.00	0.11	30	300
	BL30/0.14		1.50		0.14		
	BL30/0.18		2.00		0.18		
	BL30/0.26		3.00		0.26		
	BL30/1.00		10.00	10.00	1.00		
	BL30/2.00		20.00	-	2.00		
2	**BL**15/0.26		3.00	20.00	0.26	15	
	BL120/0.26				0.26	120	
3	**L**480/0.14		1.50	20.00	0.14	480	
	L480/0.26		3.00		0.26		
	L480/1.00		10.00	10.00	1.00		

3.3 Preparation of Dye-Sensitized Solar Cells with Blocking Layer

Two types of Dye-Sensitized Solar Cells were made in this work. The first type was a standard DSSC which consisted of working electrode, counter electrode and liquid electrolyte in between. The working electrode was made of FTO glass with applied porous layer of semiconductor that was loaded with dye molecules. Counter electrode was made of more conductive FTO glass with applied catalyst particles. Working and counter electrodes were joined together with polymeric sealant that also separated them from direct contact with each other. The space between electrodes was filled with liquid electrolyte. One edge of each electrode was coated with well conducting material to provide electrical contacts for the

cell. The second type of cell was DSSC with Blocking Layer. This type had similar structure as the standard cell however its FTO glass in working electrode was initially coated with semiconducting thin film, as the BL, by PLD. Details of the deposition of this type of film are described in Section 3.2. In this research, three out of four similar samples of each thin film deposition named **BL** were used to make cells thus their names begin with $\mathbf{C_{BL}}$. Additionally, nine standard type DSSCs were prepared and their names begin with $\mathbf{C_{ST}}$. All prepared DSSCs, including type of used PLD coating and number of prepared samples of particular group, are listed in Table 3.2. The table also contains deposition duration and oxygen partial pressure during the deposition of each type of Blocking Layer. Figure 3.4 shows WE and CE electrodes at different stages of fabrication as well as fabricated DSSC.

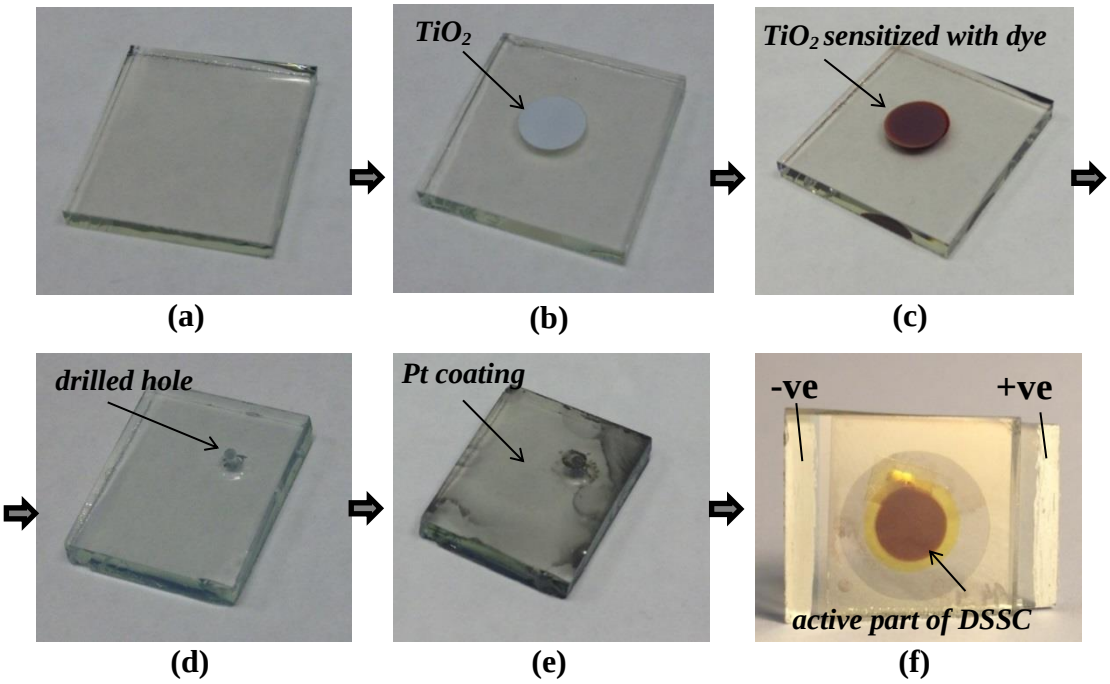

Figure 3.4: Subsequent stages of preparation of WE: (a) FTO glass, (b) the glass with porous structure of TiO_2, (c) the TiO_2 sensitized with dye; of CE: (d) FTO glass with drilled hole, (e) the glass coated with Pt; and (f) completed DSSC.

Table 3.2: Types and names of DSSCs and incorporated BLs.

Cell type name	BL type name	Size of active cell area (cm^2)	Number of cells	BL deposition duration, t_d (min)	Deposition oxygen partial pressure, p_{O_2} (mTorr)
C_{ST}	-	0.283 cm^2	9	-	-
C_{BL}30/0.11	**BL**30/0.11		3	30	0.11
C_{BL}30/0.14	**BL**30/0.14		3		0.14
C_{BL}30/0.18	**BL**30/0.18		3		0.18
C_{BL}30/0.26	**BL**30/0.26		3		0.26
C_{BL}30/1.00	**BL**30/1.00		3		1.00
C_{BL}30/2.00	**BL**30/2.00		3		2.00
C_{BL}15/0.26	**BL**15/0.26		3	15	0.26
C_{BL}120/0.26	**BL**120/0.26		3	120	0.26

3.3.1 Working electrode preparation

The TCO glass used in this study for working electrode was fluorine doped tin oxide coated (FTO) float glass slide of 2.3 mm thickness and surface resistivity of about 13 Ω/sq (TEC 15, Sigma-Aldrich). The FTO glass was chosen because unlike its counterpart ITO, does not change its electrical properties due to the heat treatment required during the cell preparation. For preparation of standard DSSC, the glass slide was firstly cut into small samples with size of 20 mm x 18 mm (see Figure 3.4a). Afterwards, the cut samples were well cleaned by an ultrasonic treatment in water mixed with dishwashing liquid and then in pure isopropanol for 15 min in each step to degrease them and remove any other surface impurity. The cleaning process was followed by drying with a hot air blower. For preparation of DSSC with BL, the cut into size of 20 mm x 18 mm samples with PLD-deposited films were used. Thus working electrodes of both standard DSSC and DSSC with

BL were built on conductive side of the same type of FTO glass. The cut samples from PLD deposition were only cleaned by an ultrasonic treatment in pure isopropyl alcohol for 15 min followed by drying with hot air blower to remove any non-adhering residues after the deposition.

Application of porous coating of semiconducting material on FTO glass (see Figure 3.4b) with or without PLD-coating was performed by screen printing on specially designed screen (see Figure 3.5). The Screen printing set consisted of aluminium block with recess for glass substrates and attached screen with artwork in the shape of rows of spots of 6 mm diameter. That spot determined the size of active area of working electrode that is 0.283 cm^2. It is important to note the reason for circular shape of the spot. The screen-printed layer of TiO_2 with the round shape and no corners will have less contact area with the electrolyte in the cell in comparison to the rectangular shape that is also common in research on DSSCs. Smaller contact area per volume will reduce leakage current during the cell operation. Each circular spot in this study was applied on the centre of individual glass substrate of size of 20 mm x 18 mm. Mesh of the screen used in this process was 90T. This set allows to screen print up to 16 spots of paste on a substrate thus can be used to prepare up to 16 individual cells. The advantage of this technique is that it provides repeatable quality of applied layers over entire screen within the same printing process despite it is a handmade process. Furthermore, for experienced operator it also allows to obtain repeatable quality from one printing to another as long as quality of used materials does not change.

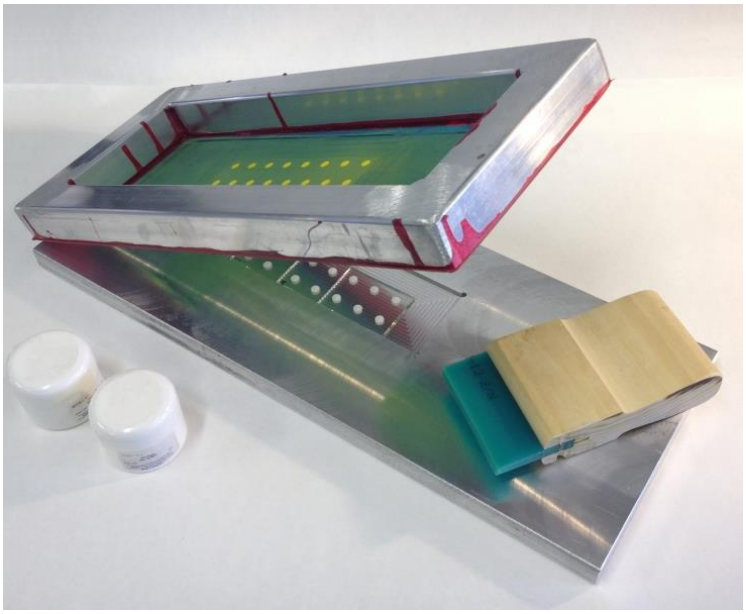

Figure 3.5: Set for screen printing of titania pastes.

Two types of paste were used in this research to screen print the porous layer of wide bandgap semiconductor that was TiO_2. The first paste was transparent titania paste (DSL 18NR-T, Dyesol) having an average particle size of between 10 nm and 30 nm. The second paste was active opaque titania paste (DSL 18NR-AO, Dyesol) having an average particle size between 200 nm and 300 nm. Both pastes are commercially available products. The transparent paste was used twice in the process to obtain two transparent layers. Instead, the opaque paste was used once to attain one light-scattering opaque layer which will effectively increase the optical path length for photos. After deposition of each layer, the glass substrates were placed on a hot plate and heated up gradually to 100^{o}C to reduce moisture contained within. Subsequently, glass substrates with applied trilaminar coating were put into programmable furnace in order to sinter them into one solid porous structure. Sintering was performed by way of slow heating up to about 450^{o}C, with 10 min dwell at about 375^{o}C and 30 min dwell at maximum temperature, followed by slow cooling down to room temperature. This process allowed achieving one porous spot of 6 mm diameter and about 16 μm thickness, as measured by stylus profilometer, on each individual sample.

Each prepared working electrode having porous layer of TiO_2 was then sensitised with dye molecules (see Figure 3.4c) by immersing it overnight in dye solution. Sensitization was done in dark, at room temperature, for 16 hours to assure complete sensitizer uptake. The solution was prepared by dissolving ruthenium-based dye (N719 Industry Standard Dye, Dyesol) in pure ethanol in such quantity to achieve 0.3 mM molar concentration. After sensitization was complete, working electrode was rinsed with ethanol and dried at room temperature.

3.3.2 Counter electrode preparation

The FTO glass used for counter electrode was fluorine doped tin oxide coated float glass slide of 3 mm thickness and surface resistivity of about 10 Ω/sq (TEC 10, Sigma-Aldrich). The glass slide was firstly cut into small samples with size of 20 mm x 18 mm and afterwards a hole of 1 mm diameter was drilled in each sample (see Figure 3.4d). Thereafter, the samples were cleaned by an ultrasonic treatment in water with washing-up liquid and then in pure isopropanol for 15 min in each step to remove greasiness and other surface impurity. This was followed by drying with a hot air blower. The conductive side of cleaned and dry glass was coated with a droplet of platinum solution spread over via doctor blade method. The sample then was put into furnace at $400^{o}C$ for 20 - 25 min in order to thermally decompose the solution that resulted in well distributed catalytic layer of platinum nanoclusters (see Figure 3.4e). The Pt-solution in this work was prepared by dissolving such quantity of $H_2PtCl_6 \cdot 6H_2O$ (Chloroplatinic acid hexahydrate, Sigma-Aldrich) in pure isopropanol to achieve 10 mM molar concentration of Pt.

3.3.3 Cell assembling

The dye-covered TiO_2 working electrode and Pt-coated counter electrode were assembled together sandwiching a polymeric sealant in between. The sealant used in this work was 50 μm thick thermoplastic film (Dyesol's Low Temperature Thermoplastic Sealant, DuPont™ Surlyn®). Before cell assembly, this was cut into ring shape of 8 mm internal and 12 mm external diameter to surround the TiO_2 spot of working electrode as airtight spacer between two electrodes. Sandwiched components of a cell with asymmetric alignment were placed under a preheated to 120^{o}C heat transfer press (Test Cell Heat Press, Dyesol) where were hot pressed with a pressure of 6 bar for 35 seconds (see Figure 3.6). These conditions let the sealant to partially melt and tightly bond both electrodes.

Figure 3.6: Assembling DSSC via heat transfer press.

3.3.4 Filling cell with electrolyte solution

The airgap between electrodes of assembled cell was vacuumed in a desiccator connected to a vacuum pump (see Figure 3.7). The created void was then filled with a liquid electrolyte via backfilling a drop of the electrolyte placed on the hole drilled in counter electrode. Afterwards, the hole was sealed by a 60 μm thick aluminium adhesive tape. The electrolyte solution prepared for this work consisted of: 0.05 M Iodine (I_2) and 0.5 M Lithium-Iodide (LiI) as a redox couple, 0.1 M Guanidinium thiocyanate (GuSCN) and 0.5 M 4-*tert*-butylpyridine (TBP) as additives to suppress electrons recombination at titania electrolyte interface, 3-methoxypropionitrile (MPN) as organic solvent.

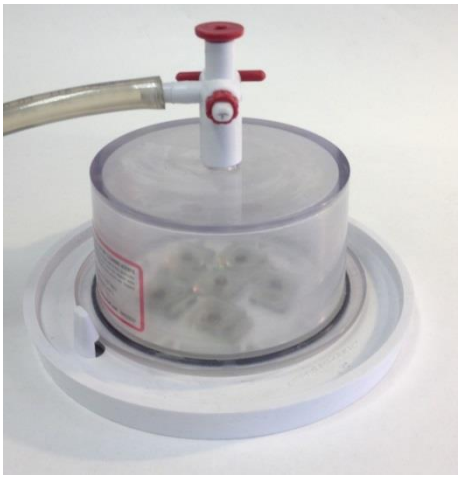

Figure 3.7: DSSC backfilling with electrolyte under vacuum desiccator.

3.3.5 Electrical contacts preparation

Asymmetric alignment of electrodes in assembling process exposed one edge of each electrode. Cells with blocking layer, that were made of working electrode with PLD-coated titanium oxide layer, were aligned in such a way that uncoated edge of 3 mm width was exposed. In each case, the protruding conductive edges of electrodes were painted with silver (Silver Conductive Paint, RS) by brush

painting. Such prepared cells (see Figure 3.4f) were ready for measurements after 30 min.

3.4 Summary

- Deposition procedure of thin film of TiO_2 by Pulsed Laser Deposition as Blocking Layer for Dye-Sensitized Solar Cells was presented. All necessary steps of the deposition process were listed. The growth conditions of titanium oxide thin films using PLD were detailed.
- Reason for variable parameters in deposition process was given. Successful deposition of titanium oxide films was reported and their application of the deposited films was declared.
- Fabrication of Dye-Sensitized Solar Cells incorporating Blocking Layers and those without BL was described in details. Distinction between prepared samples was explained. Specification of all used components for cells preparation and type of fabricated components was noted.

Chapter 4: Characterisation of deposited thin films

4.1 Introduction

The aim of this chapter is to present all characterisation techniques used in this research for characterisation of structural, optical and electrical properties of deposited films. This chapter also shows all the obtained results and presents detailed discussion and conclusions on each measured property of the deposited films.

4.2 Crystallography

4.2.1 XRD technique

X-ray diffraction (XRD) is one of the non-destructive techniques used in materials science. It is utilised for identification of crystallinity, a crystalline phase, and crystals orientation of a material based on interaction of incident X-rays with the material. The atoms in the material cause a beam of incident X-rays incoming from a source of radiation to diffract into many directions. If the irradiated material is amorphous, a scattering of the beam is diffuse, arising from the distribution of short-range structure. Instead, when the beam hits a crystalline material or crystalline phase of multiphase material, it diffracts into many specific directions. Scattered rays are collected by a detector moving in different directions relative to the incident beam. Quantity of the collected scattered-rays is automatically counted and plotted by a computer as a function of diffraction angle (2θ). The diffraction patterns for amorphous materials are similar and always consist of a broad low peak in lower angels region with entire background being raised. On the other hand, the diffraction patterns for crystalline materials feature sharp characteristic peaks emerging from low background. Amount of peaks, their position, and relative height is individual feature for every crystalline phase of the material. The diffraction patterns of many materials have been created and

collected in databases. The XRD analysis is the identification of peaks on obtained diffraction pattern by matching them with characteristic peaks on diffraction patterns from powder diffraction file (PDF) database.

In this study, the crystallographic properties of deposited films were characterised using a Philips PW1710 Automated Powder Diffractometer. This XRD system, equipped with a Cu K_α radiation source of wavelength of 1.54 Å, was operating at 35kV, 40 mA with a scan speed of 0.005 °2θ/s (slow scan), or with speed of 0.02 °2θ/s (faster scan) in a 2θ range from 2° to 80°. Identification of phases was done using a Philips PC-Identify software. To accommodate the sensitivity of the XRD measurement, two sets of titanium oxide films for XRD analysis were prepared by PLD deposition at significantly longer deposition duration (t_d).

A first set was prepared at deposition duration of 360 minutes. The chosen oxygen partial pressure (p_{O_2}) was 0.26 mTorr, which corresponds to the deposition pressure of couple of samples used as BL, and was selected to investigate crystallinity and composition of these group of titanium oxide BL samples. In order to distinguish between peaks of the film and peaks of the substrate, two different substrates were chosen; FTO glass and Si wafer. The substrates were cut to squares of 1 cm by 1 cm and used in the same experiment which provided identical film growth conditions. These samples were tested with XRD at faster scan speed.

The second set consisted of three titanium oxide film samples prepared by PLD deposition on FTO glass substrate at deposition duration of 480 minutes, to enhance the intensity of the peaks on XRD pattern. In order to investigate the influence of oxygen partial pressure on crystallographic properties of the films, the samples were prepared under different oxygen pressures, identical to three exemplary selected out of samples used as BL. The three samples of the second set were scanned with slower scan speed that further enhanced sensitivity of the measurement to enable to analyse results quantitatively with more precision. Both

sets of samples and their main deposition conditions are listed in Table 4.1 and their preparation is in details described in Chapter 3.

Table 4.1: The two sets of samples prepared for XRD analysis.

sample	deposition duration, t_d (min)	oxygen partial pressure, p_{O_2} (mTorr)	substrate type	type of XRD analysis
L360/0.26-F	360	0.26	FTO glass	qualitative
L360/0.26-S			Si wafer	
L480/1.00	480	1.00	FTO glass	
L480/0.26		0.26		
L480/0.14		0.14		

4.2.2 Results and analysis

Figure 4.1 shows XRD patterns obtained for titanium oxide film deposited on FTO glass and Si wafer. Film deposited on the silicon substrate features couple of distinct peaks emerging from low background. Also a couple more peaks with very small intensities can be distinguished from the background. All of the peaks are reasonably narrow. These denote that obtained film was quite crystalline. A similar situation is observed for film deposited on FTO glass substrate, where a couple of strong peaks are presented along with weakly visible peaks. On the other hand, the peaks are somewhat broader than in the first case, and also background is enhanced, especially for lower angles of diffraction between 20° to 40°. The latter feature might in some cases eclipse low intensity peaks existing in that region. Nevertheless, film deposited on this substrate can also be considered as crystalline to some extent.

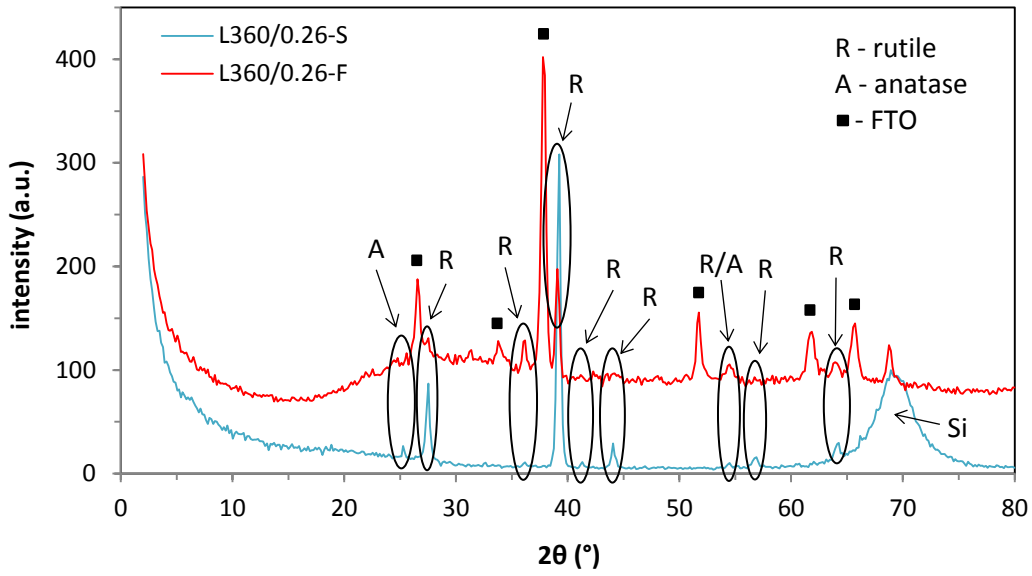

Figure 4.1: XRD patterns of the titanium oxide film deposited via PLD on Si wafer and FTO glass at 300°C, at oxygen partial pressure equal 0.26 mTorr, for 360 minutes.

The raised background in the diffraction pattern for the film on the FTO substrate, which appears for lower diffraction angles, can be attributed to the glass as information depth in this type of diffractometry is deeper than the thickness of sub-micrometre films. For the same reason, strong and broad peak appears in the second diffraction pattern, which can be assigned to Si wafer. Location of three other strongest peaks in the latter diffraction pattern, which appeared at 27.5°, 39.2°, and 64.3° correspond to TiO_2 that is rutile phase. These three peaks have their equivalent, relatively distinguishable peaks on the diffraction pattern for the film on the FTO substrate. In the case of the silicon substrate, there are four other peaks which locations correspond to rutile phase of TiO_2 in powder diffraction file (PDF) database despite they appeared weak on the analysed diffraction pattern. Only one of these peaks that appeared at 36.2° has its analogue peak on the other diffraction pattern where appeared to be relatively strong. Three other peaks that appeared perceivable at 41,3°, 44.0°, and 56.9° on the diffraction pattern for the film on the silicon do not have their equivalents on the diffraction pattern for the

film FTO glass. On the pattern for the silicon sample, there is a peak at 25.3°, which can be unequivocally assigned to TiO_2 that is anatase phase. However, its analogue on the pattern for FTO sample does not appear against the background noise. The last peak that appeared as common on both patterns is located at 54.5°. This peak corresponds to TiO_2 in patterns database, but its crystallographic phase cannot be distinguished as both rutile and anatase phases feature a peak at this angle of diffraction on their patterns. In this situation this ambiguous peak might correspond to one of the phases or some combination of the two. The remaining six out of seven strongest peaks that appeared on the diffraction pattern for the film deposited on the FTO glass substrate well correspond to the peaks of FTO layer (H.-J. Kim et al. 2012), which is a component of the FTO glass.

XRD analysis of titanium oxide film deposited by PLD from TiO target, at 300°C, at oxygen partial pressure of 0.26 mTorr showed that obtained film consists of crystalline TiO_2 that is notably rutile phase, with possible participation of anatase phase. Diffraction patterns for the film deposited on the silicon and the FTO substrates feature similar peaks for TiO_2 material that might indicate that films deposited on both substrates under these conditions are similar. Absence of some low intensity peaks, which appear on pattern for silicon sample, from pattern for FTO sample, might result from raised background noise in the latter case.

Figure 4.2 presents three XRD patterns obtained for titanium oxide films deposited on FTO glass only, at deposition duration of 480 min, at three different oxygen partial pressures. Two additional patterns are from powder diffraction database and represent TiO_2 of rutile and anatase separately, as these two patterns of Ti-O system seem to be the best match to patterns obtained for prepared films. All three patterns of these films are similar to each other as well they are similar to some extent to the pattern for sample L360/0.26-F. The sample L480/0.26 was prepared under the same conditions as the latter, except the deposition duration which was longer, therefore, it was expected to obtain similar pattern. The main difference between the patterns for films deposited at longer deposition time and

the pattern for film deposited at slightly shorter time is higher intensity of all the peaks and more clear distinction of the peaks from the background in the first case. This can be credited to longer deposition duration that further increased the thickness of the films as well as to slower scan speed which increased resolution of the measurement. This approach overcame a problem with poor quality and credibility of the measurement which was a great drawback in an attempt to analyse the influence of deposition conditions on composition and crystalline structure of the films form XRD patterns obtained directly from thin film samples of blocking layers.

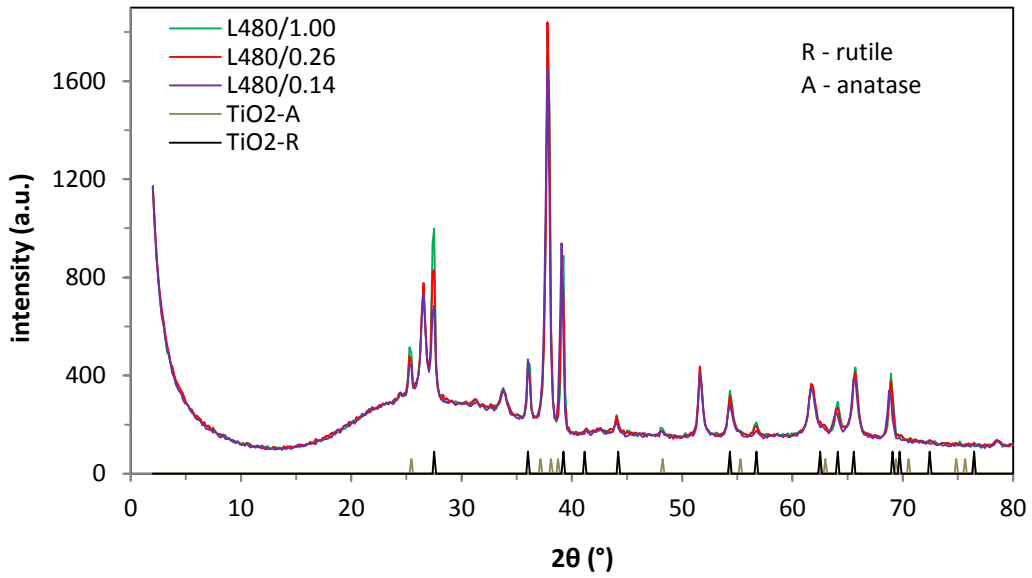

Figure 4.2: XRD patterns of the titanium oxide film deposited via PLD on FTO glass at 300°C, for 480 minutes, at oxygen partial pressures: 1.00 mTorr, 0.26 mTorr, and 0.14 mTorr; 2θ range: 0-80°.

In the case of relatively thicker films, deposited at 480 minutes, all diffraction patterns feature several distinct peaks emerging from a background in spite of the fact that the entire background is still somewhat elevated, especially in a region of lower angels of diffraction, due to the contribution of the glass of FTO glass substrate. The emerged peaks are proportionately distinguishable from the

background that it can be assumed that all films deposited at those conditions are fairly crystalline.

The more detailed view on diffraction patterns, in the range of angle of diffraction between 20° and 45°, for thicker films is shown in Figure 4.3. The strongest peak in that range, which relates to the films, appeared at diffraction angle of around 39.1°. This peak appeared with similar intensity on all three patterns for thicker films and well corresponds to peak of rutile TiO_2 of crystal plane of (200) on the diffraction pattern from database (Ref. Code: 165925, at ICSD).

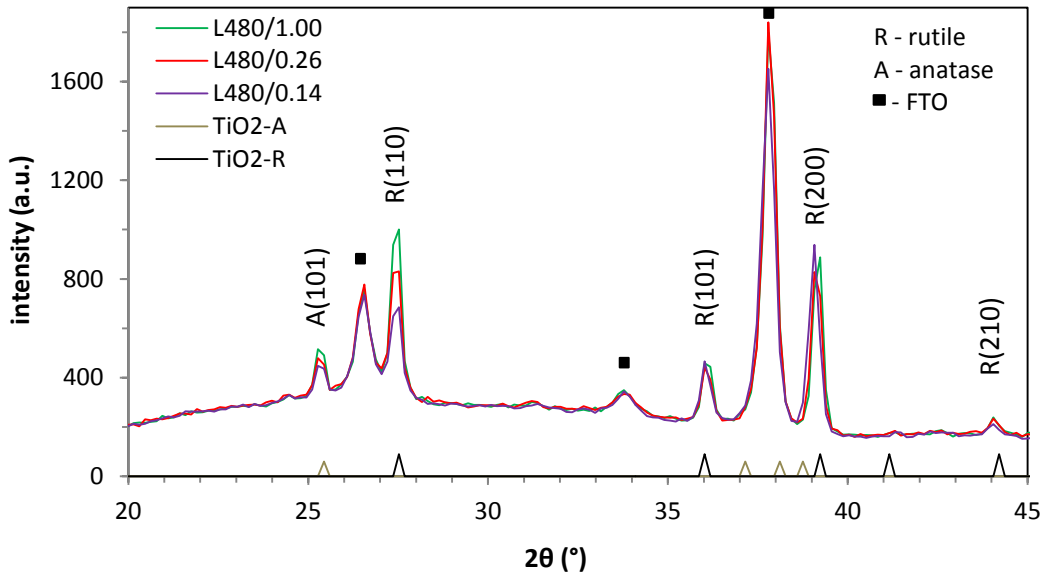

Figure 4.3: XRD patterns of the titanium oxide film deposited via PLD on FTO glass at 300°C, for 480 minutes, at oxygen partial pressures: 1.00 mTorr, 0.26 mTorr, and 0.14 mTorr; 2θ range: 20-45°.

The next strongest peak in that region appeared at 27.5°. It appeared for all three film samples, but its intensity is clearly different for each sample. This peak corresponds to TiO_2 of rutile phase of crystal plane of (110). On the pattern in the database it is the strongest peak for that phase and is well known as the most characteristic peak for rutile phase in research of TiO_2 materials (Li et al. 2014;

Sanz et al. 2009). Clear trend can be seen between the intensity of this peak on obtained patterns and oxygen partial pressure during the deposition of the films. The higher the oxygen partial pressure is the higher the intensity of the peak appears on the diffraction pattern. This indicates that higher content of oxygen gas during deposition might favour growth of rutile TiO_2 in a crystallographic direction of (110), at least under oxygen partial pressure between 0.14 mTorr and 1.00 mTorr. It is important to mention that other deposition conditions were identical for all three deposition processes, especially the total pressure, which was 2 mTorr, and argon was always supplied proportionally to oxygen in order to keep the total pressure constant.

Another strong peak that appeared on diffraction pattern at lower angles of diffraction is located at 25.3°. This peak also appears for all three film samples and its intensity, when compared between the samples, also differs to some extent. The peak corresponds to TiO_2 of anatase phase of crystal plane of (101). This peak on the pattern in the database (Ref. Code: 92363, at ICSD) is the strongest and is well recognised as the most characteristic peak for anatase phase in study on TiO_2 materials (György et al. 2005; Li et al. 2014). In this case a certain trend between oxygen partial pressure during the films deposition and the intensity of this peak on obtained patterns can also be seen. Some increase of peak intensity with increase of oxygen partial pressure suggests that growth of the anatase TiO_2 phase of crystal plane of (101) might be enhanced by higher concentration of oxygen gas during the deposition. On the other hand, increase of the intensity of the peak assigned to anatase phase with increase of p_{O_2} is smaller than increase of the intensity of the peak assigned to rutile phase with increase of p_{O_2}. Therefore, comparison of changes in relative intensity of peak assigned to rutile and peak assigned to anatase, between the samples indicates that increase in oxygen partial pressure during the deposition might favours growth of rutile (110) over anatase (101) in spite of the fact that growth of both phases increases with increase of oxygen gas content. Sanz et al. (Sanz et al. 2009) observed similar trend of predominant formation of rutile over anatase during PLD-deposition of TiO_2

under oxygen-reach deposition conditions. On the other hand, Lin et al. (Lin et al. 2008) and Luca et al. (Luca et al. 2006) observed increased formation of anatase over rutile phase when oxygen pressure used for deposition was increased.

Two other peaks that are presented at lower angles of diffraction on diffraction patterns of prepared films appeared at angles of 36.0°, and 44.0°. Both peaks are univocally assigned to rutile TiO_2 of crystal planes of (101) and (210), respectively. Both peaks appear on all three diffraction patterns with persistent intensities that indicate that the growth of rutile TiO_2 in these two directions occurs for films deposited under discussed conditions and seems to be constant regardless of oxygen partial pressure, at least within discussed range.

Second part of more detailed view on diffraction patterns, in the range of angle of diffraction between 45° and 70°, for thicker films is shown in Figure 4.4. This region of the pattern also features couple of distinctive peaks related to TiO_2. First worth mentioning peak is the one that appeared at the angle of 56.7°. Despite the fact that it is one of the weak peaks, it is observable on all three patterns of the films. Moreover, the peak at this position was also noticeable on the diffraction pattern for somewhat thinner film deposited on silicon wafer (see Figure 4.1). This peak was assigned to rutile TiO_2 of crystal planes of (220). This peak at standard diffraction pattern from the database has moderated intensity, which can explain its low intensity on patterns obtained from prepared films. The peak intensity tangibly differs between the patterns and the difference follows similar trend as for a certain previously mentioned peaks, where higher concentration of oxygen gas used for deposition could result increased formation of rutile phase of particular crystallographic direction.

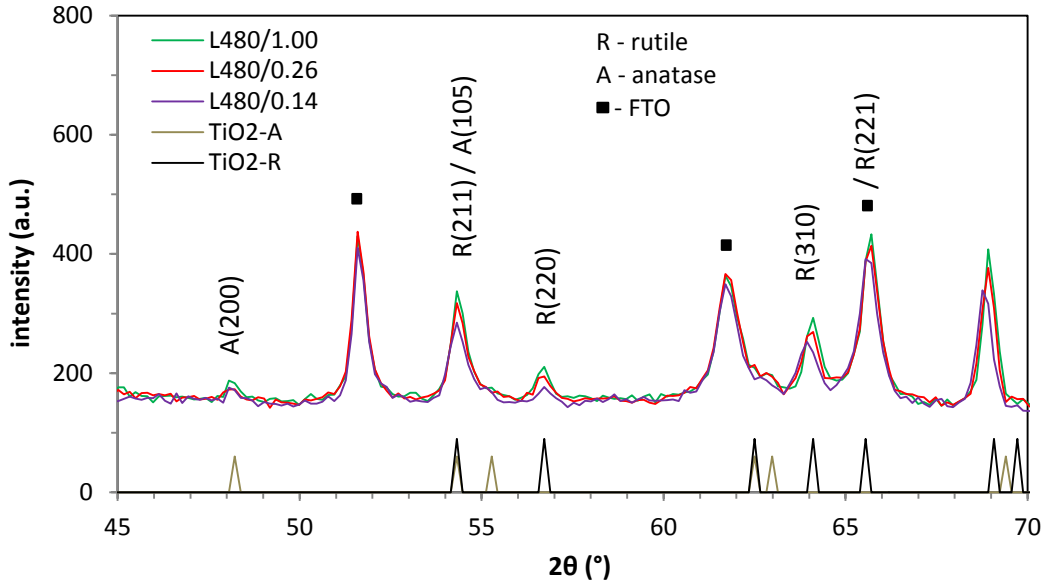

Figure 4.4: XRD patterns of the titanium oxide film deposited via PLD on FTO glass at 300°C, for 480 minutes, at oxygen partial pressures: 1.00 mTorr, 0.26 mTorr, and 0.14 mTorr; 2θ range: 45-70°.

Another idiosyncratic peak appeared around 48.1°. This peak has low intensity, yet it is distinguishable from the background on all three diffraction patterns. It corresponds to anatase TiO_2 of crystal planes of (200), especially that peak at this angle of diffraction on standard diffraction pattern for anatase from patterns database is the second most intense peak. Due to its low intensity on patterns from prepared samples a clear trend between formation of anatase of this particular crystallographic direction and oxygen partial pressure during deposition cannot be concluded.

The most intense peak at higher angles of diffraction which can undoubtedly derive from the deposited film appeared at 54.3°. In this particular case, the peak can be assigned to rutile TiO_2 of crystal planes of (211), which gives the second strongest peak on standard pattern of rutile TiO_2, or anatase TiO_2 of crystal planes of (105), which gives one of the relatively strong peaks on standard pattern of anatase TiO_2 at the same angle of diffraction as that of the rutile. It cannot be also excluded that peak at this angle, which is clearly visible on

all three patterns of prepared films, result from some combination of the two phases of this particular crystallographic directions existing in some or all prepared films. Nevertheless, a certain trend between oxygen partial pressure during the films deposition and the intensity of that peak on obtained patterns can also be seen, which follows previously described relation, where intensity of the peak increased with increased oxygen partial pressure. This can only suggest that the peak might originate from rutile phase formation in the film under a certain growth conditions. However it does not exclude other possibilities.

Another distinct peak on all three patterns of prepared films appeared around the angle of 64.0°. It corresponds to rutile TiO_2 of crystal planes of (310) that gives a peak of moderate intensity on standard diffraction pattern from the database. Intensity of that peak on all three patterns feature similar trend between oxygen partial pressure during the films deposition as a certain peaks at lower angles. This only confirms the validity of the hypothesis that higher oxygen partial pressure during deposition enhances formation of rutile TiO_2.

As relative intensities of certain peaks on the patterns from prepared samples not necessary match to relative intensities of peaks on the standard patterns, as well as lack of some strong, characteristic peaks on obtained patterns that normally appear on standard patterns, does not exclude the scenario where peak which appeared around the angle of 65.7° might originate not only from FTO layer, but also from rutile TiO_2 of crystal planes of (221). This peak on the standard pattern appears as very weak, but there is a certain increment of intensity when samples were deposited at higher oxygen partial pressure, whereas intensities of other peaks ascribed to FTO layer do not follow this trend and remain pretty constant regardless the oxygen partial pressure.

To sum up, all analysed diffraction patterns of deposited relatively thick films from TiO target, at 300°C, under low pressure conditions, and three variant oxygen partial pressures, show characteristic features of quite well crystalline films, regardless the used substrates. Most of the peaks on the patterns correspond to TiO_2 of rutile phase and some of anatase phase, regardless the used oxygen

partial pressure during the deposition of the films. For this reason, all deposited films in this research under oxygen partial pressure between 0.14 mTorr and 1.00 mTorr can be considered as crystalline films that majorly consist of TiO_2 of mixed anatase and rutile phases with dominant of the latter. Intensities of certain peaks ascribed to rutile phase are trending upwards in proportion to higher oxygen partial pressure used during the depositions which indicates that higher oxygen gas concentration during the process might favours formation of rutile phase. Also noticeable increase in intensity of one of the peaks ascribed to anatase proportionally to oxygen partial pressure suggests that formation of this phase could also be enhanced by higher concentration of oxygen gas during the process. However, enhancement of peaks assigned to rutile phase is more distinct than of this assigned to anatase, therefore, at higher oxygen partial pressures growth of rutile phase is more favourable than formation of anatase. Increase in intensities of only certain peaks for both phases in proportion to higher oxygen gas concentration during the deposition appears to increase concentration of TiO_2 in general. Thus possibility of existence of some other phases from Ti-O system cannot be dismissed. This scenario is possible when target used for PLD deposition is not TiO_2, but for instance TiO, like in this research, and oxygen gas concentration during the process is relatively very small. Peaks that appear on diffraction patterns at high angles of diffraction and do not correspond well to peaks of standard patterns of TiO_2 might also indicate existence of some other phases. Moreover, relative intensities of the peaks on diffraction patterns of prepared samples do not match relative intensities of the peaks on standard diffraction patterns from database, and some peaks have some tendency to slightly broaden. These may also result from coexistence of some other phases in the obtained films, but also can feature a certain directional growth of the film that might be influenced by type of used substrate. Fully reliable XRD analysis of the films with use of standard XRD technique requires preparation of relatively thick films, closer to a micrometre or more, due to relatively deep penetration of the sample by X-ray beam. Thus all obtained diffraction patterns of prepared films

feature several very strong peaks related to the substrate and raised background noise that could overlap with other peaks which could exist on the patterns and originate from other crystallographic phases.

4.3 Cross-sectional microscopy and film thickness determination

4.3.1 Cross-sectional scanning electron microscopy and ellipsometry

Electron microscopy is a microscopy technique that uses a beam of accelerated electrons as a source of illumination to produce image of a sample. As the wavelength of electrons can be many thousand times shorter than that of visible light photons, electron microscopes can achieve magnifications of up to hundreds of thousand times. A scanning electron microscope (SEM), which was used in this study, produces the image by scanning the sample with the focused beam of electrons that interact with atoms in the sample. The electrons from the beam can be reflected or back-scattered out of the specimen and collected by a detector. These types of electrons are called backscattered electrons (BSE). The interaction of beam electrons with the sample can also result in ejection of electrons from the specimen atoms. This type of detected electrons is called secondary electrons (SE).

In this research, the SEM was employed to produce cross-sectional images of the deposited film samples in order to estimate the thickness of the films (d_f) and hence the deposition rate (r_d). To this purpose, the remaining quadrant of the film sample cut after the deposition (see Chapter 3) was placed in SEM with cross-section exposed towards the incident beam. All of the samples consist of well conducting FTO layer, however, vast majority of their volume is made of glass, thus at large are considered as electrically insulating. For this reason, the samples were pre-coated with ultra-thin carbon coating in order to prevent the accumulation of electrostatic charges at the surface of the specimen during the imaging. Although all of the samples of thin films deposited as prospective blocking layers were carbon-coated, electrostatic charges accumulation issue was

not overcame in some cases and consequently only five out of eight samples were studied by SEM. Perhaps the carbon-coating in those cases was not thick enough to discharge those samples effectively. The electron microscope used in this study was FEI XL30 Field Emission Gun Environmental SEM (ESEM) fitted with back-scattered electron detector. The microscope was operating in BSE detection mode and accelerating beam voltage of 15 kV or higher. Obtained images showed cross-section of the film on the FTO glass substrate with magnification of 120 000 times or higher. The cross-sectional images which presented the layers of titanium oxides deposited on multi-layer FTO coating on glass were used to evaluate the thickness of studied thin films. The thickness was averaged over 7 locations for each sample of which up to standard image was obtained. For samples obtained at identical deposition duration (t_d) of 30 minutes and at different oxygen partial pressures (p_{O_2}), the deposition rate (r_d) was calculated using equation (4.1), where the film thickness (d_f) was the averaged value from cross-sectional images.

$$r_d = \frac{d_f\,(nm)}{t_d\,(\text{min})} \tag{4.1}$$

The obtained cross-sectional images were also used to assess the quality of deposited films that is its adhesion, roughness, uniformity and continuity.

Ellipsometry is another non-destructive technique used in thin films technology. It can be employed to estimate film thickness as well as optical constants by examining a particular interaction of light with the sample. In ellipsometer, a portion of a known incoming light that is obliquely reflected from the sample is detected and analysed in terms of its oscillating components of an electric field. The reflection occurs at the surface of the sample as well as at the surface of a sublayer when layers above it in a multilayer sample are at least partially transparent to the incoming light. The incident light is a known polarised light, which electric field vector oscillating in a plane of incidence is called p-polarised light and an electric field vector oscillating perpendicularly to the plane of incidence is called s-polarised light. The enabling principle of ellipsometry is that both components of the linearly polarised light reflect differently and create

an elliptically polarised light. A complex reflectivity ratio of p- and s-polarised light, which is measured, relates to ellipsometric Ψ and Δ parameters, where the former describes the magnitude of the ratio and the latter defines the phase difference between p- and s-polarised reflected light. The measured ellipsometric data are plotted as a function of wavelengths of incident light. To analyse the measured dataset, it is necessary to define an optical model corresponding to the structure of the sample which is used by a computer software to generate an equivalent ellipsometric dataset. Then, the software searches for the input model parameter values which minimise the difference between the measured data and model generated data to match these datasets with good accuracy. An algorithm responsible for matching the data calculates the means square error (MSE) to quantify the difference between the datasets. The smaller the MSE the better is the fit. The mean square error is proportional to a sum of differences between the experimental data and model calculated that can be expressed as

$$MSE \propto \sqrt{\sum(Model - Experiment)^2} \tag{4.2}$$

The ellipsometer used in this study was a spectroscopic ellipsometer (M-2000, J.A. Woolam) which collects over 700 wavelengths from ultraviolet to the near infrared with different angles of incidence. The measurement of the samples was performed at three angles of incidence equal to 65°, 70° and 75°. The range of wavelengths was between 200 nm and 1000 nm. The analysis of the data was performed within the visible range that was from 400nm to 800 nm. The purpose of this experiment was to supplement the thickness evaluation of the deposited thin films on some of the samples that were not analysed by SEM as well as to support the results already obtained by electron microscopy. Some of the evaluated values of the films thickness were used to supplement and support the calculations of the deposition rate using the equation (4.1).

4.3.2 Influence of deposition duration

Figure 4.5 presents the cross-sectional image obtained by SEM for sample with the titanium oxide film deposited via PLD at 300°C, under oxygen partial pressure of 0.26 mTorr and at the deposition duration of 120 min. The image distinctly shows the FTO glass stack that consists of three layers of total thickness of about 386 nm. The thickness of the deposited film measured from this image was about 154 nm. It can be clearly seen that the deposited film has intimate contact with FTO substrate without any visible delamination, which means that the adhesion of the film to the substrate is very good. There are no visible cracks across the film, which means that the cohesion of the film is satisfactory. The deposited layer seems to be uniform in terms of the thickness, which shows that it was uniformly deposited over the substrate, and with the previous observation, it indicates that the film is pinhole free. The surface of the deposited layer is smoother as against the surface of the FTO thus the roughness of the film is presumably less than that of the FTO.

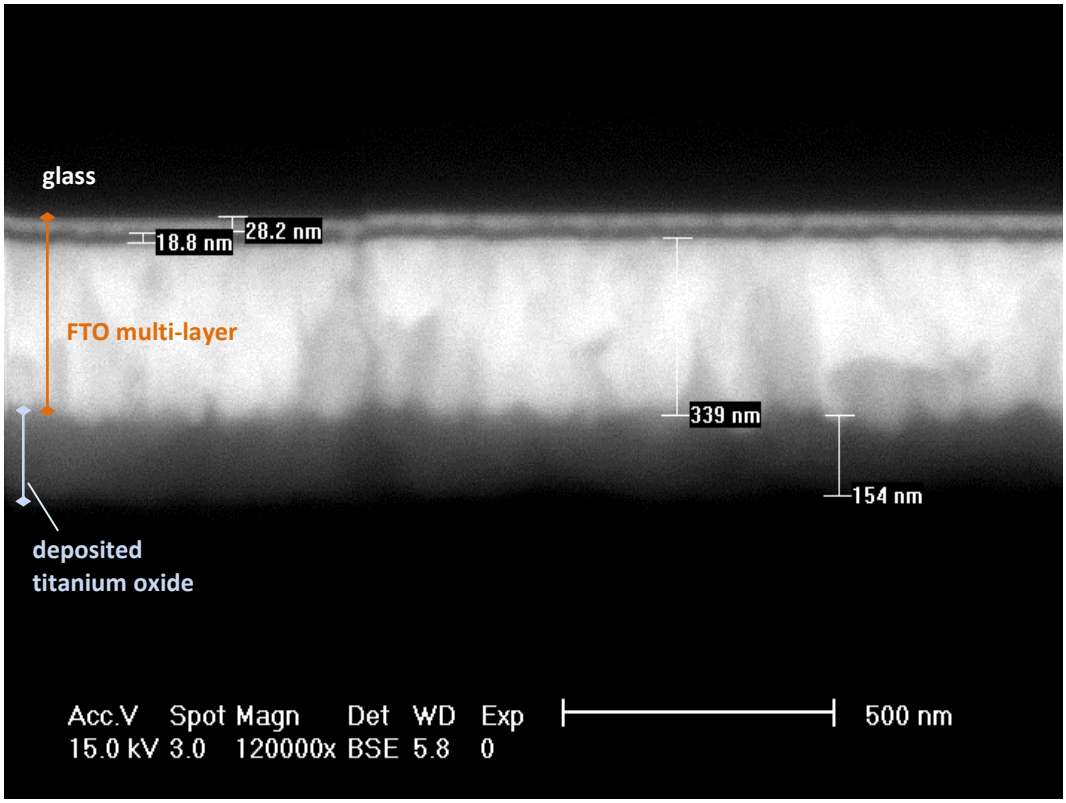

Figure 4.5: Cross-sectional SEM image of the titanium oxide film deposited on FTO glass under p_{O_2} of 26 mTorr, at deposition duration of 120 minutes; sample BL120/0.26.

Figure 4.6 shows the cross-sectional image for the titanium oxide film deposited under the oxygen partial pressure of 0.26 mTorr and at the deposition duration of 30 min. The thickness of the deposited film that was measured from this image was about 53 nm. Although the obtained image was not very sharp, it was observed that the film was uniform in thickness, with good adhesion to the substrate and continuous.

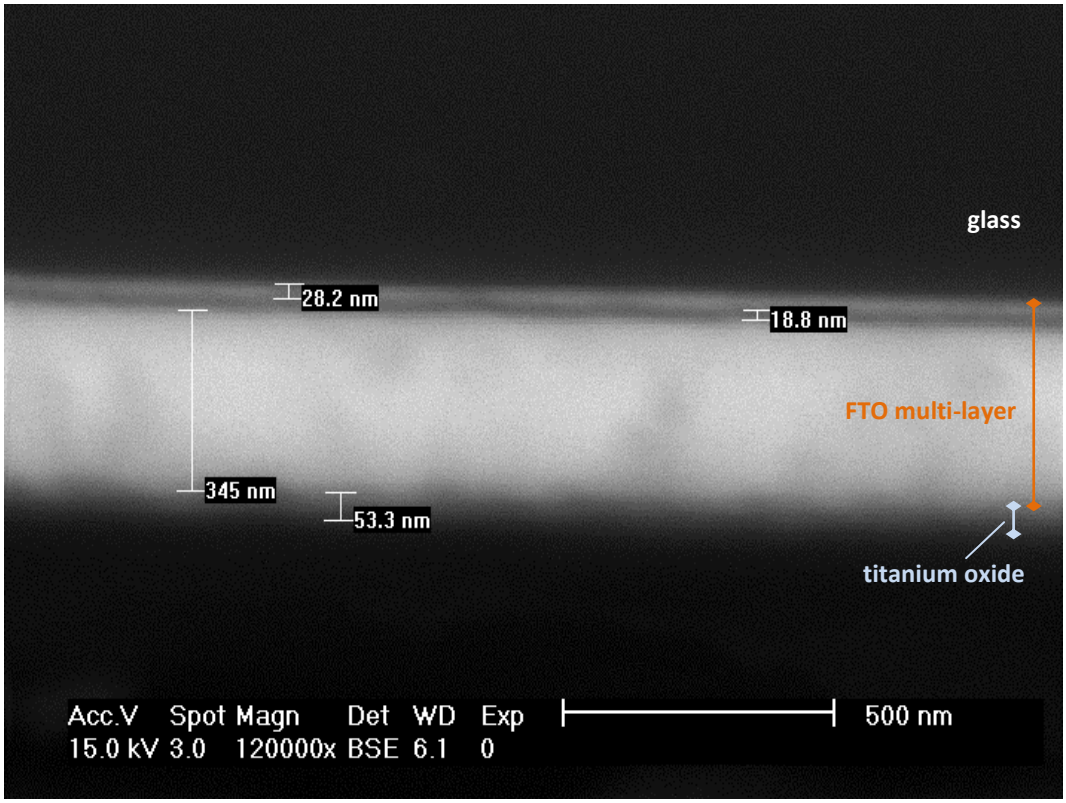

Figure 4.6: Cross-sectional SEM image of the titanium oxide film deposited on FTO glass under p_{O_2} of 0.26 mTorr, at deposition duration of 30 minutes; sample BL30/0.26.

The cross-sectional image of the film deposited under the oxygen partial pressure of 0.26 mTorr and at the deposition duration of 15 min is presented in Figure 4.7. The thickness of the film was estimated to be 28 nm. Although the obtained image was not sharp, at higher magnification the film seemed to be continuous.

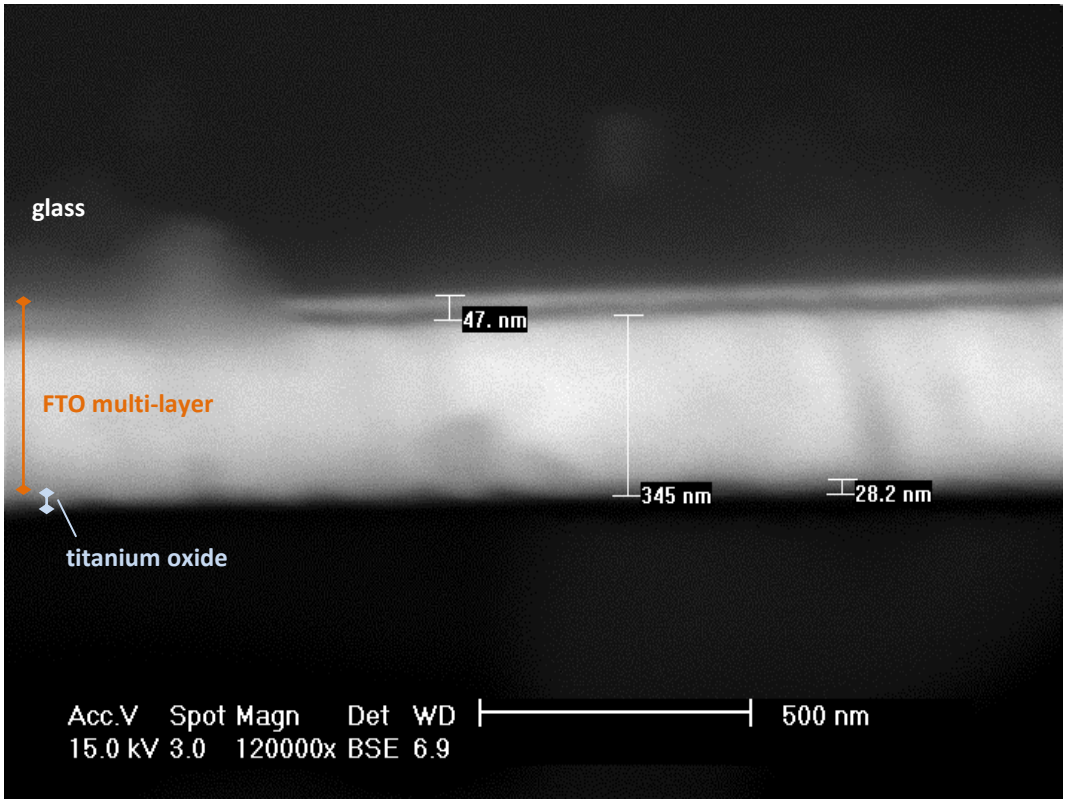

Figure 4.7: Cross-sectional SEM image of the titanium oxide film deposited on FTO glass under p_{O_2} of 0.26 mTorr, at deposition duration of 15 minutes; sample BL15/0.26.

Figure 4.8 shows the thickness of the deposited films as a function of the deposition duration for samples obtained under identical oxygen partial pressure of 0.26 mTorr. Presented values of the thickness are averaged over several locations for each sample, obtained via SEM, and are supported by the measurement via ellipsometry. The averaged values and their errors of estimation are detailed in Table 4.2. The value of thickness assessed by ellipsometry does not deviate significantly from the value obtained via SEM for the same sample. Estimated thicknesses of the films tend to fall into trend similar to linear trend. However, at shorter deposition duration films seem to grow slightly faster than at longer deposition process, therefore, a power trend-line was used as a best-fit to experimental data. The R-squared value of the trend-line is 0.996 which is very good fit of the line to the data. Such estimation confirms that at shorter deposition

process the film growth-rate is somewhat higher than at longer processes. This confirms that adhesion of the film to the substrate at the deposition temperature used in this research, which was 300°C, is satisfactory.

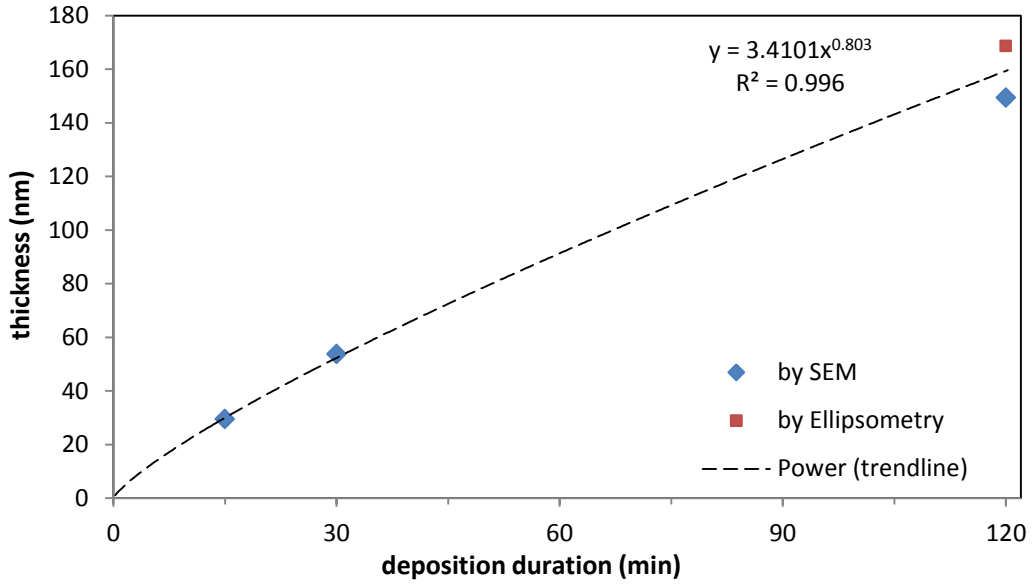

Figure 4.8: Estimated thickness of thin film BLs obtained at p_{O_2} = 0.26 mTorr at different deposition durations; assessed by SEM and ellipsometry.

Table 4.2: Estimated thickness of thin film BLs obtained at p_{O_2} = 0.26 mTorr at different t_d; assessed by SEM and ellipsometry.

sample	deposition duration, t_d (min)	oxygen partial pressure, p_{O_2} (mTorr)	film thickness by SEM - averaged, d_f (nm)	standard deviation, *SD* (nm)	standard error, *SE* (nm)	film thickness by ellipsometry - averaged, d_f (nm)	mean squared error, *MSE* (nm)
BL15/0.26	15	0.26	29.5	1.5	0.57	-	-
BL30/0.26	30		53.7	2.6	0.98	-	-
BL120/0.26	120		149.3	6.5	2.47	168.55	16.301

4.3.3 Influence of oxygen partial pressure

Figure 4.9 shows the cross-sectional image obtained by SEM for sample with the titanium oxide film deposited by PLD at 300°C, at the deposition duration of 30 minutes, under oxygen partial pressure of 2.00 mTorr. The film can be distinguished from the substrate multi-layer, therefore, its thickness estimated as about 58 nm can be considered as reliable. Another cross-sectional image for this sample is shown in Figure 4.10 where it is clearly seen that the deposited film has intimate contact with the substrate without a sign of delamination that proves good adhesion of the film to the substrate. Lack of cracks across the film suggests that the cohesion of the film is satisfactory. Uniform thickness of the deposited film shows that it was uniformly deposited over the substrate that proves that the film can be pinhole free. The surface of the deposited layer seems to be smoother to some extent in comparison with the surface of the FTO layer thus the roughness of the film is presumably somewhat less than that of the FTO. Results from the observation of this sample, named as BL30/2.00, are identical to that of the sample BL120/0.26, which was deposited under lower oxygen partial pressure. Therefore, it can be assumed that the films deposited in this research are deposited with good match to the substrate.

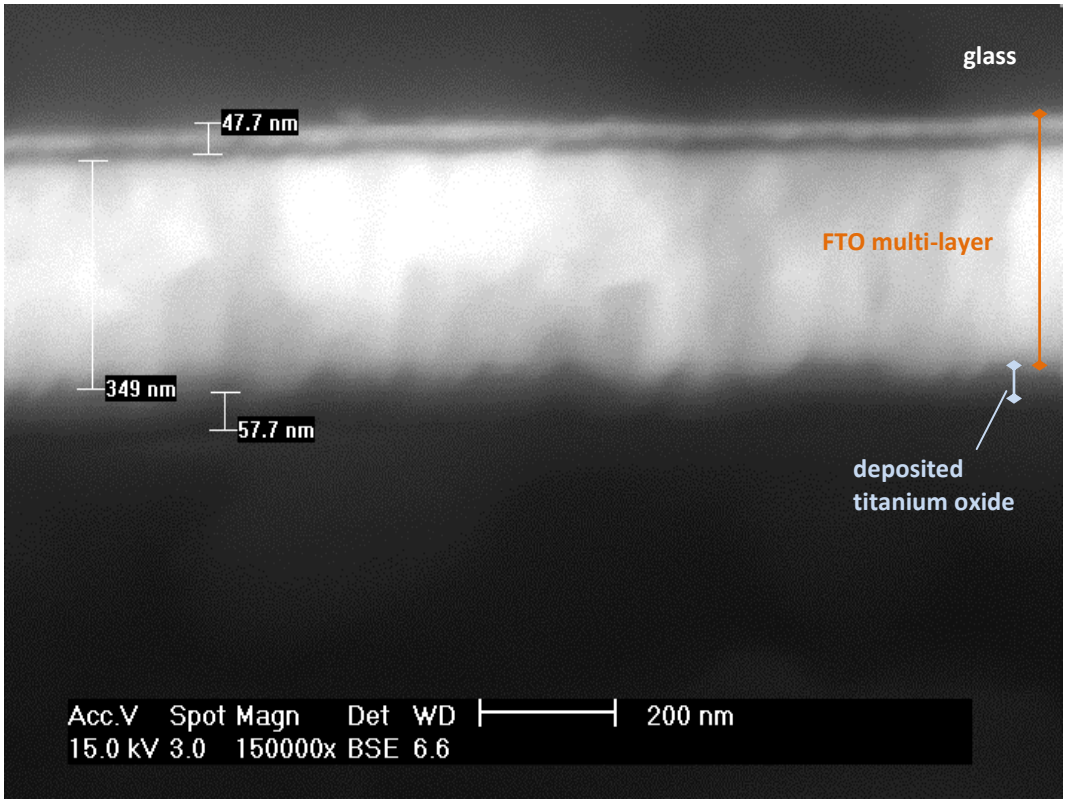

Figure 4.9: Cross-sectional SEM image of the titanium oxide film deposited on FTO glass at deposition duration of 15 minutes, under p_{O_2} of 2.00 mTorr,; sample BL30/2.00.

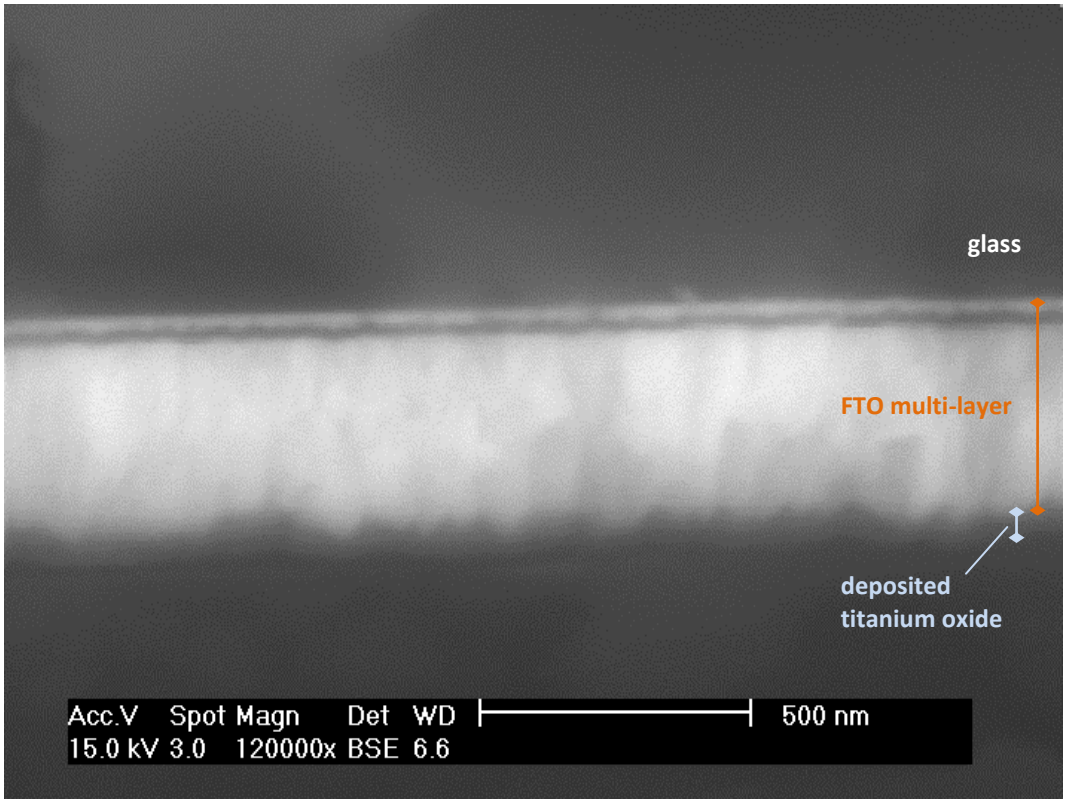

Figure 4.10: Cross-sectional SEM image of typical titanium oxide film deposited on FTO glass; sample deposited at 15 minutes, under p_{O_2} of 2.00 mTorr,; sample BL30/2.00.

Figure 4.11 presents the relation between the thicknesses of the deposited films and oxygen partial pressure for samples obtained at the identical deposition duration of 30 minutes. Presented values of the thickness are averaged over several locations for each sample, obtained from SEM images, and are supplemented and supported by the thickness measurement via ellipsometry. There is lack of data for one sample obtained at p_{O_2} = 1.00 mTorr. Images obtained by SEM were not clear enough to distinguish the deposited film from the substrate. Measurement of this sample by ellipsometry was not performed as this sample was already carbon coated for SEM measurement. Therefore, direct estimation of the thickness of the film for this particular sample turned out to be impossible. The averaged values of the thicknesses of measured samples and the

errors of estimation are detailed in Table 4.3. The value of thickness assessed by ellipsometry deviate to some extent from the value obtained via SEM for the sample BL30/2.00, however this could be related with their errors of estimation. As a whole, all of the estimated thicknesses for these films oscillate about the value of 53 nm with agreeable deviation. Therefore, a linear trend-line was used as a best-fit to experimental data. Similar results of the thickness for films, obtained at identical deposition duration, regardless the oxygen partial pressure used during the films deposition indicates that the deposition rate is independent from oxygen gas concentration and probably more dependent on total pressure during the process. In that case, it can be concluded that the deposition rate is controled by the total pressure, the film thickness by deposition duration, and properties of the film result from the composition and structure considerably controlled by oxygen partial pressure. Calculated deposition rate as a function of oxygen partial pressure is presented in Figure 4.12. The typical deposition rate was estimated as 1.78 nm/min.

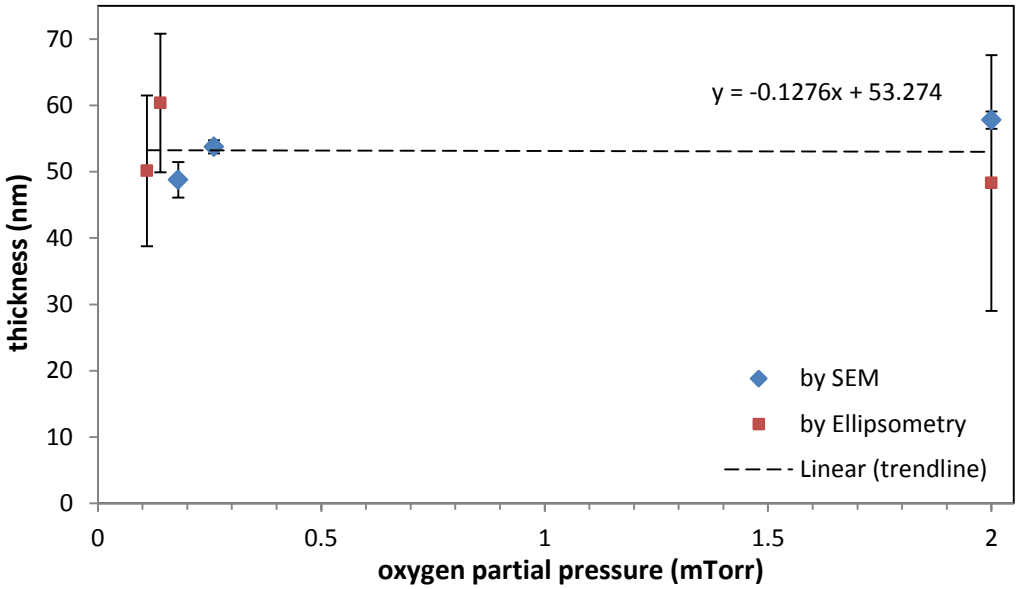

Figure 4.11: Estimated thickness of thin film BLs obtained at t_d = 30 min, at different oxygen partial pressures; assessed by SEM and ellipsometry. Error bars represent SE for SEM, MSE for ellipsometry data.

Table 4.3: Estimated thickness of thin film BLs obtained at t_d = 30 min, at different p_{O_2}; assessed by SEM and ellipsometry.

sample	deposition duration, t_d (min)	oxygen partial pressure, p_{O_2} (mTorr)	film thickness by SEM - averaged, d_f (nm)	standard deviation, *SD* (nm)	standard error, *SE* (nm)	film thickness by ellipsometry - averaged, d_f (nm)	mean squared error, *MSE* (nm)
BL30/0.11	30	0.11	-	-	-	50.12	11.359
BL30/0.14		0.14	-	-	-	60.36	10.455
BL30/0.18		0.18	48.8	5.4	2.68	-	-
BL30/0.26		0.26	53.7	2.6	0.98	-	-
BL30/2.00		2.00	57.8	3.5	1.32	48.28	19.267

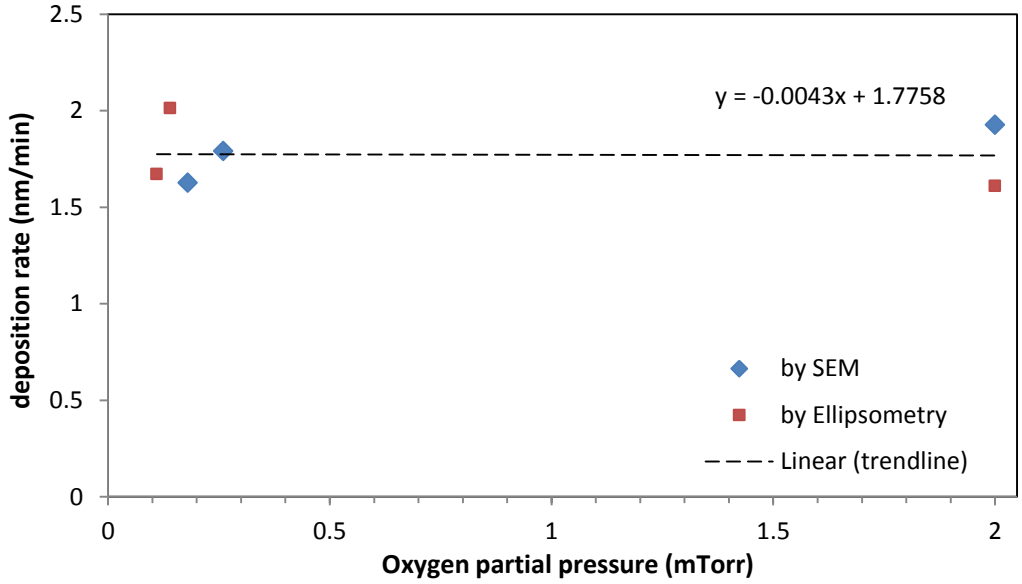

Figure 4.12: Estimated deposition rate of thin film BLs obtained at t_d = 30 min, at different oxygen partial pressures; assessed by SEM and ellipsometry.

4.4 Optical transmittance

4.4.1 Spectroradiometer and measurement setup

One of the techniques used for measuring the spectrum of electromagnetic radiation emitted by a light source is spectroradiometry. This method is the measurement of absolute radiometric quantities, typically spectral radiance and spectral irradiance, in narrow wavelength intervals. Therefore, measuring the spectrum requires separation of radiation into its constituent wavebands whereby each band can be measured separately. After the measurement of the intensity of each band, the measured values are plot as the function of the wavelength which represents the spectral characteristics of the light source.

In order to measure the spectrum of radiation by spectroradiometers, the first unit of the system must consist of input optics. This gathers the radiation form a specific field of view and delivers it to the second unit. At this stage, the

radiation that entered the system has to be split into its component wavelengths in a unit called monochromator. This is always done by reflecting the wavelengths of radiation at different angles, either by a prism or by using a diffraction grating. After that, a quantification of the radiation of each waveband is performed by a detector which measures the radiation at each wavelength. Finally, data gathering, defining, and storing, as well as controlling of the spectroradiometer, is done by a logging and control system.

Spectroradiometry is used in many ways in laboratories. Exact measurement of the emission spectrum of a source gives information about the emitting substance. On the other hand, the inverse process can be used to identify a material when a known spectrum of radiation is shone upon the substance and the spectroradiometer is employed to quantify the amount of the radiation that has passed through the material. By measuring this, it is possible to precisely determine a transmittance of the material or its closely related quantity that is absorbance. Investigating the later properties is also often performed by spectroscopy methods which work on the same principle, where matter, under certain conditions, absorbs or emits energy depending on the energy of incident photons. An optical transmittance or related absorbance is commonly measured by UV-VIS-NIR spectroscopy when the material is irradiated with an ultraviolet-visible-near-infrared light of a continuous wavelength.

In this study, the spectroradiometer was used to evaluate total transmittance of light through the FTO glass samples coated with titanium oxide film that was deposited by PLD (see chapter 3). In this measurement, a source of incident light was a solar simulator. In order to measure a spectrum of radiation, a spectroradiometer was used. The transmittance of the samples was measured individually for each sample by placing it between the light source and light measuring device, on top of a head of spectroradiometer. To minimise refraction of incident light passing through a sample, the head of spectroradiometer and the sample was set perpendicularly the direction of incident radiation. The measurement was performed inside a Faraday cage to protect the equipment from

external electromagnetic fields that would influence the measurement. The entire spectroradiometer apparatus is presented in Figure 4.13. List of the samples and their main deposition conditions are listed in Table 4.4.

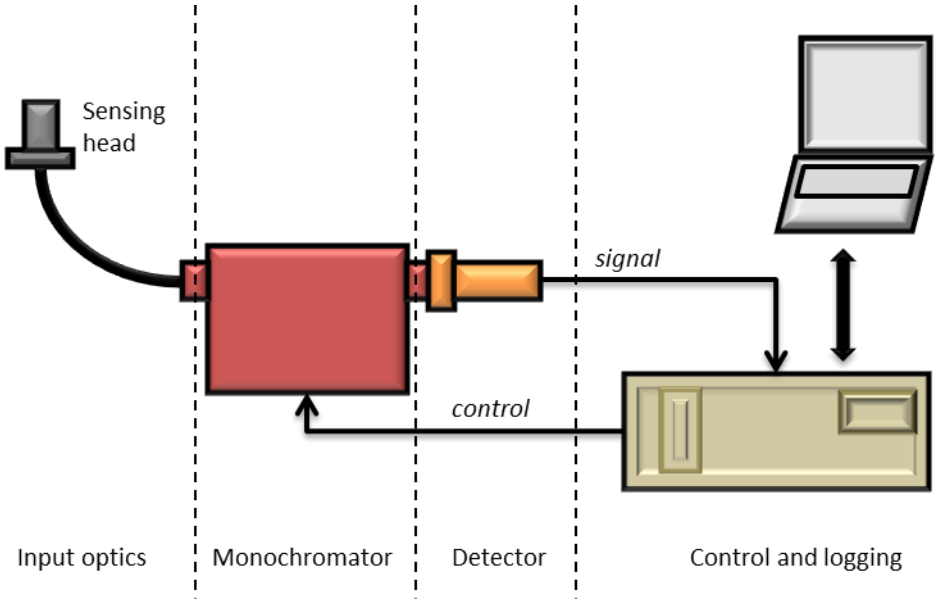

Figure 4.13: Diagram of spectroradiometer with division into main units.

Table 4.4: List of measured samples and their basic deposition conditions.

sample	oxygen partial pressure, p_{O_2} (mTorr)	deposition duration, t_d (min)	deposition temperature (^{o}C)	total gases pressure (mTorr)
bare FTO	-	-	-	-
BL30/0.11	0.11	30	300	2.00
BL30/0.14	0.14			
BL30/0.18	0.18			
BL30/0.26	0.26			
BL30/1.00	1.00			
BL30/2.00	2.00			
BL15/0.26	0.26	15		
BL120/0.26		120		

The measurement of the transmittance with the use of the spectroradiometer was performed in a few several steps as shown in Figure 4.14. Firstly, the spectroradiometer was calibrated with a calibration light source (CL6, Bentham Instruments) to guarantee that the measurement within entire measurement spectrum is adequate. The calibration light source is fitted with a 150 W quartz halogen lamp, which emission spectrum is identical to black-body radiation with peak wavelength at 770 nm. During the calibration, the measuring head, which contains input optics, was kept from the light source at fixed, appropriate distance provided by socket of housing of the calibration lamp. The housing protects the system from external electromagnetic fields. Calibration parameters and entire procedure were managed via computerised control unit.

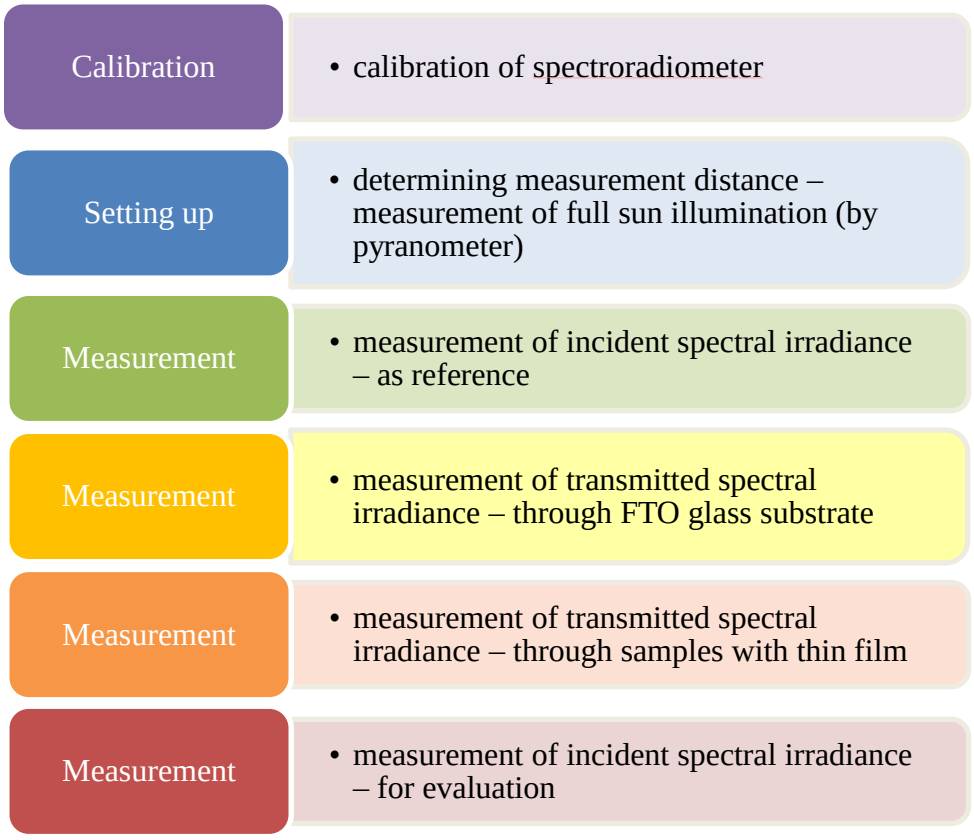

Figure 4.14: Flowchart of light transmittance measurement of the prepared samples.

In that step, it was necessary to choose a light source for transmittance measurement and determine constant distance between the head of spectroradiometer and the light source. The chosen source of radiation was a continuous light from the solar simulator that was also later used for test of performance of fabricated DSSCs (LCS-100 Solar Simulator, Newport). The solar simulator is ABB class. This means that its spectral match to the standard values is within 0.75 – 1.25 for each interval, irradiance spatial non-uniformity is classified as 5%, and temporal instability is classified as 5%. The radiation source in the solar simulator is a xenon lamp. Light from the lamp in this facility passes through a set of optics including light filters thus so the spectrum of radiation exiting the solar simulator is very similar to that of the sun on the earth surface as it is standardized to a spectrum known as AM1.5. An intensity of the light was selected to be 1000 W/m^2, which corresponds to full sun illumination, like for performance characterisation of the DSSCs. Setting the intensity of the radiation was done by use of a pyranometer that is commonly used for irradiance measurements of light sources. With this end in view, the pyranometer was placed directly under the solar simulator, on a levelled surface, perpendicularly to the incident light. The entire solar simulator mounted to a vertically moving stage is capable of changing the light intensity by moving further or closer to the illuminated area. This feature was used to set the appropriated distance between the solar simulator and the pyranometer. Setup for determining the adequate distance for transmittance measurement is presented in Figure 4.15.

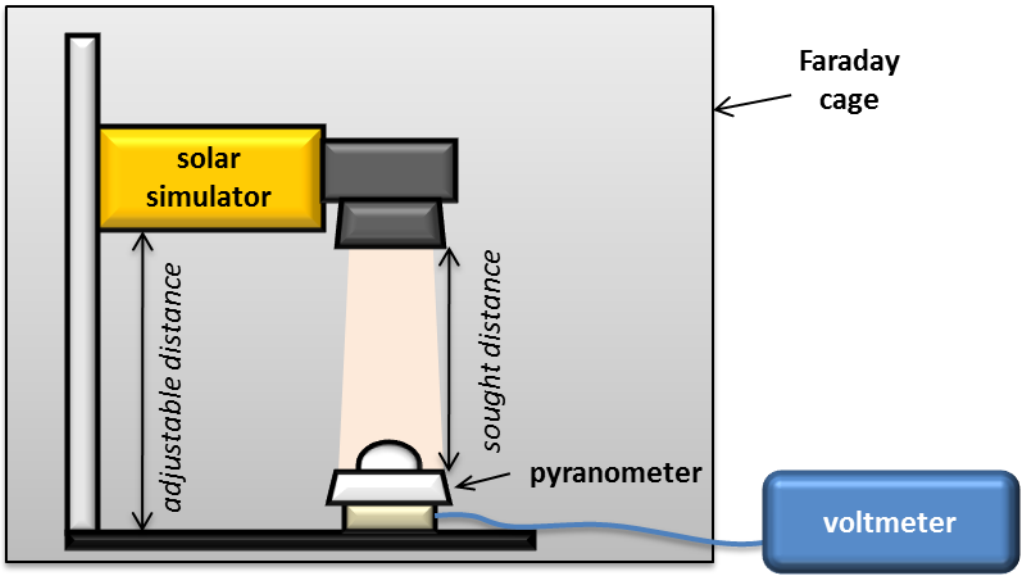

Figure 4.15: Setting up distance for transmittance measurement.

In this step, the head of the calibrated spectroradiometer was placed under the solar simulator in the location of pyranometer. The top of the head was positioned on the same level where pyranometer detected full sun illumination. This configuration was maintained for all the following measurements undertaken for assessment of transmittance of deposited films. The first measurement was taken for solar simulator only in order to measure the spectral irradiance of incident light established as a radiant flux received by a surface of a sample (Φ^i). The measuring range of wavelengths was between 280 nm and 800 nm, which covers part the UV, VIS and part of the NIR spectrum, at 0.5 nm intervals. Next measurements were taken for a glass sample placed between the incident light and the head. In all those cases the sample was placed directly on top of the head and oriented perpendicularly to the incoming light, with FTO coated side facing down towards the head, which was in identical orientation against the incident light as FTO glass in working electrode during the measurement of performance of DSSCs under illumination conditions. The setup and sample configuration for measurement of its light transmittance is shown in Figure 4.16.

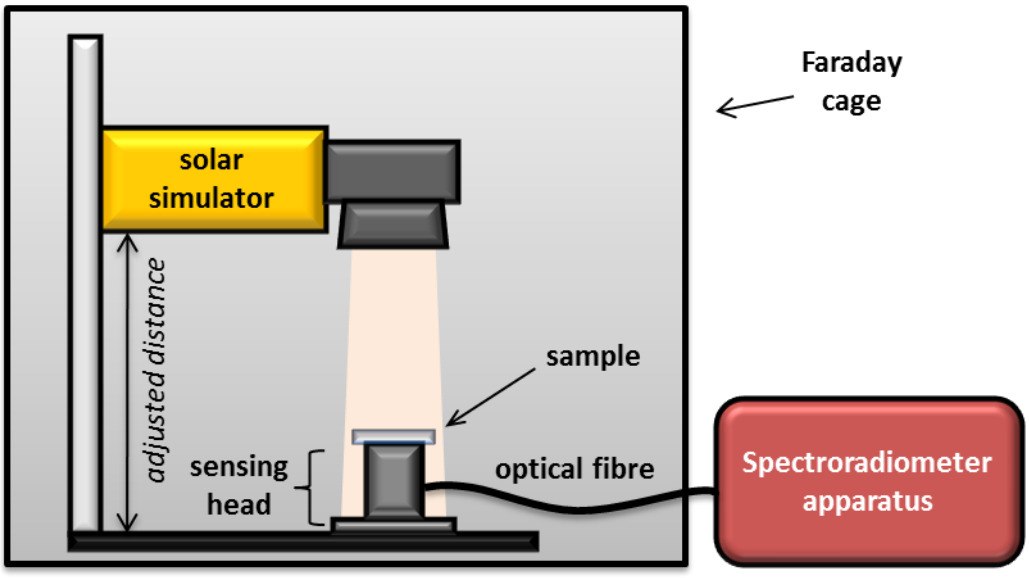

Figure 4.16: Measurement setup for light transmittance measurement of the prepared samples.

The bare FTO glass substrate was also measured in order to establish the transmittance of the uncoated substrate used for titanium oxide film growth. The following measurements were taken individually for all glass samples containing titanium oxide film deposited via PLD. The range of measuring the spectral irradiance of the light that passed through the sample, as well as the measurement step length were the same as for measuring the incident light. After the measurement of all the samples, another measurement of the incident light from the solar simulator was taken to detect any alteration in spectral radiation of the incident light or a change in sensitivity of the spectroradiometer that could develop during the experiment.

As the direct result from each measurement of a sample was only the spectral irradiance of the light that passed through, to know the value of the transmittance (T) it was necessary to calculate it using the general equation 4.3.1.

$$T = \frac{\Phi^t}{\Phi^i} \qquad (4.3.1)$$

Where:

Φ^t is the radiant flux transmitted by the sample;

Φ^i is the radiant flux received by the sample from solar simulator

The obtained data from measurement were calculated in three ways. First, by dividing the irradiance transmitted over the irradiance received for each corresponding wavelength of entire measured range, from 280 nm to 800 nm. This calculation was done separately for each sample and allows to obtain set of data that can be plot as a spectral transmittance of a sample. The second type of calculations required integration of entire measured spectrum of transmitted irradiance as well as integration of entire measured spectrum of received irradiance. Then, obtained values were employed into the equation 4.3.1 to calculate the transmission for each sample individually. The third type of calculations required division of measured spectrum into three categories. The first category incorporated Ultraviolet B (UVB) spectrum over a wavelength range of 280 nm to 315 nm. The second category incorporated Ultraviolet A (UVA) spectrum over a wavelength range of 315 nm to 400 nm. The third spectrum category was the visible spectrum over a wavelength range of 400 nm to 750 nm. After division of obtained datasets, the data were integrated within the groups for both measured irradiance of samples and solar simulator. Then, obtained values were employed into the equation 4.3.1 so the transmittance of samples for UVA, UVB and VIS spectrum was calculated. All the obtained data and their analysis are presented in the following sections.

4.4.2 Influence of deposition duration

Figure 4.17 shows spectral transmittance that was calculated, using the equation (1), from measurement of spectral irradiance of light that passed through a sample. Presented samples are those with the thin film used as a blocking layer in

DSSCs, which were deposited via PLD at 300°C, under oxygen partial pressure of 0.26 mTorr, at different deposition duration. Therefore, measured films have identical structure and composition, and variant thickness. Also calculated transmittance for bare FTO glass substrate is presented for comparison and a baseline, which represents spectral irradiance received by surface of the samples. Data are for wavelengths of light in a range between 280 nm and 800 nm.

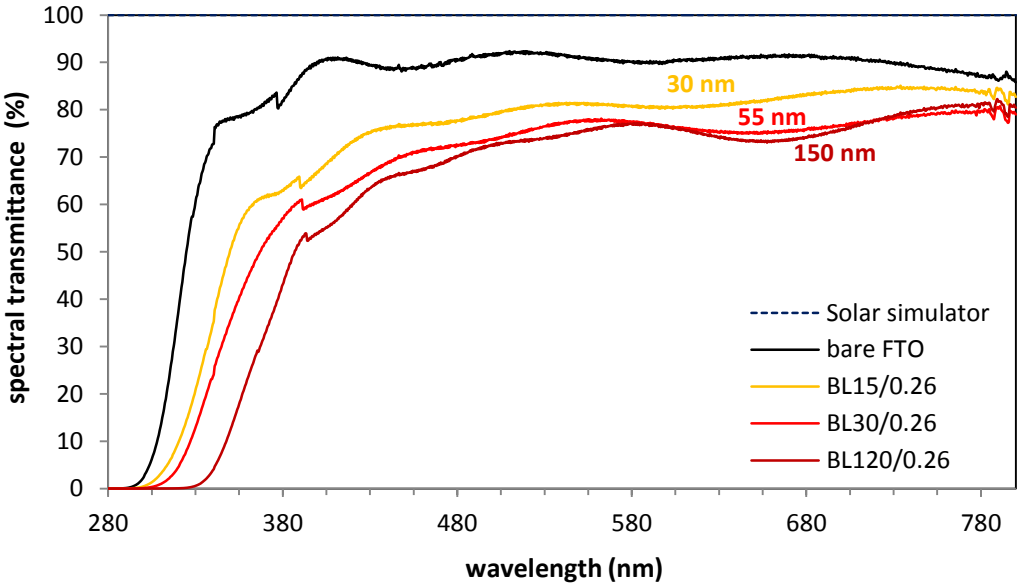

Figure 4.17: Spectral transmittance of FTO glass and samples with BL obtained at p_{O_2} = 0.26 mTorr and at different deposition duration; data in range of 280 - 800 nm. The discontinuities around 380 nm arise from filter changes in the apparatus.

It was observed that light passing through the samples is partially attenuated within entire spectrum of measurement. It noticeably differs from attenuation that occurs in the FTO glass substrate. It can be seen that the spectral transmittance decreases proportionally with increase of the film thickness, that is expected based on Beer-Lambert law. However, the attenuation does not show to be constant within the measured spectrum. Possible explanation is that the absorption coefficient might not be constant throughout the measured spectrum, but it is rather wavelength-dependant. Moreover, a certain inconsistency of

transmittance between results for samples of different thickness might result from the measurement setup and used equipment as well as from optical properties of prepared films.

The source of light in this experiment is the solar simulator that is class ABB. Temporal instability of this solar simulator is classified as 5%, which means that output light intensity varies over short periods of time, which is an order of several seconds. Measurement of spectral intensity by spectroradiometer is performed wavelength by wavelength and it takes few second per each nanometre of wavelength. Therefore, temporal deviation from assumed intensity might fall for every couple of nanometres of wavelength that was measured. As different deviation might occur for each sample within identical range of wavelength, measured intensities of wavelength and calculated transmittance might locally differ from true values.

Irradiance spatial non-uniformity of the solar simulator is classified as 5%, which means that irradiance uniformity over the work area is disturbed. This is a result from the fact that rays of the radiation are not parallel to some extent. Even if globally surface of the sample is directed perpendicularly to the beam of incident light, locally, closer to the edges, sample can be irradiated from a certain small angles. In this situation, if refractive index of the film is wavelength dependant, a certain portion of certain wavelengths of incident light might be directed towards the sensing head of the spectroradiomter, or might be directed away from it. As films thickness in this group of measured samples is different, the shift of possible redirected beams at particular wavelengths will be different as well, resulting in small local variations of calculated spectral transmittance. In spite of a certain local deviations, the general trend of spectral transmittance of analysed samples is conserved, where the transmittance decreases proportionally to increase of the film thickness.

Figure 4.18 presents the calculated transmittance of the deposited films as a function of the deposition duration, where the latter is directly proportional to the film thickness, in spectral range between 280 nm and 800 nm. It can be seen

that transmittance of sample that consists of glass with FTO layer and thinnest titanium oxide layer is decreased of further 11% against drop in transmittance through the bare FTO glass sample. Drop of additional 6% is seen for sample with nearly doubled thickness of the titanium oxide layer. The lowest transmittance of a value of about 70%, which is another drop of around 2% within the considered spectrum, was obtained in sample with thickness of about 150 nm. Calculated values of transmittance within this range are presented in Table 4.5.

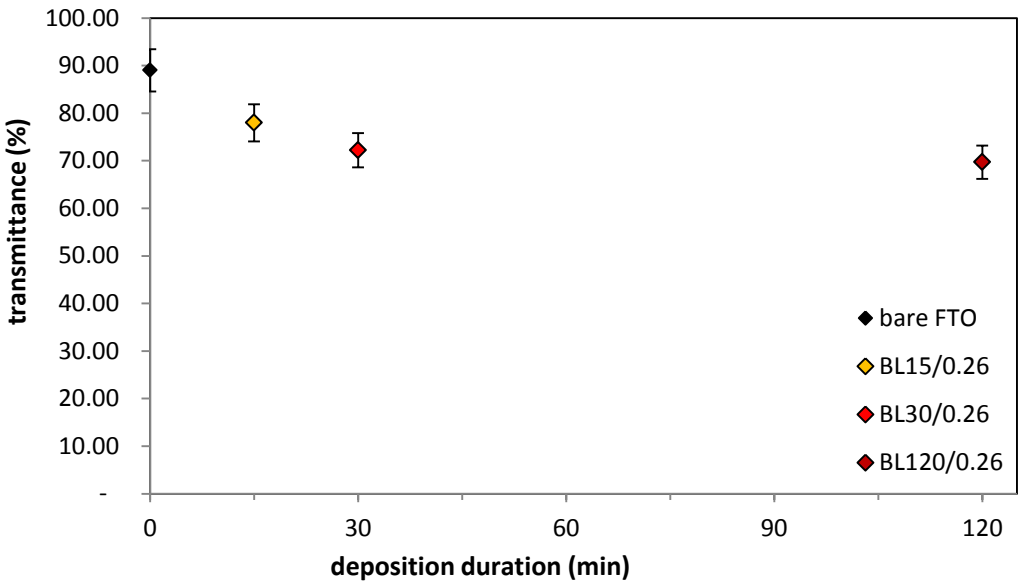

Figure 4.18: Calculated transmittance of FTO glass and samples with BL obtained at p_{O_2} = 0.26 mTorr and at different deposition duration; data in range of 280 - 800 nm. Values are encumbered with 5% error resulting from class B solar simulator.

Table 4.5: Calculated transmittance of FTO glass and samples with BL obtained at p_{O_2} = 0.26 mTorr and at different deposition duration. Values are encumbered with 5% error resulting from class B solar simulator.

sample	deposition duration, t_d (min)	measured spectrum (nm)	transmittance, T (%)
bare FTO	-	280 - 800	89.01 ± 4.450
BL15/0.26	15		77.97 ± 3.899
BL30/0.26	30		72.19 ± 3.609
BL120/0.26	120		69.70 ± 3.485

Figure 4.19 shows the calculated transmittance of the samples in the spectral range corresponding to ultraviolet B, which is between 280 nm and 315 nm. Despite the fact that FTO glass has significantly low transmittance in UVB range, the sample containing thinnest deposited film of 30 nm, attenuates this light of almost 4.5 times more reaching the value of transmittance of 0.94%. Doubled thickness of titanium oxide layer transmits the UVB over 3 times more poorly reaching the value of 0.28%. According to prediction, the lowest transmittance of UVB was obtained for the thickest sample, which reached only 0.01% that can be practically considered as UVB light blocking thickness for this type of titanium oxide film on FTO glass. Calculated values of transmittance within the UVB spectrum are presented in Table 4.6.

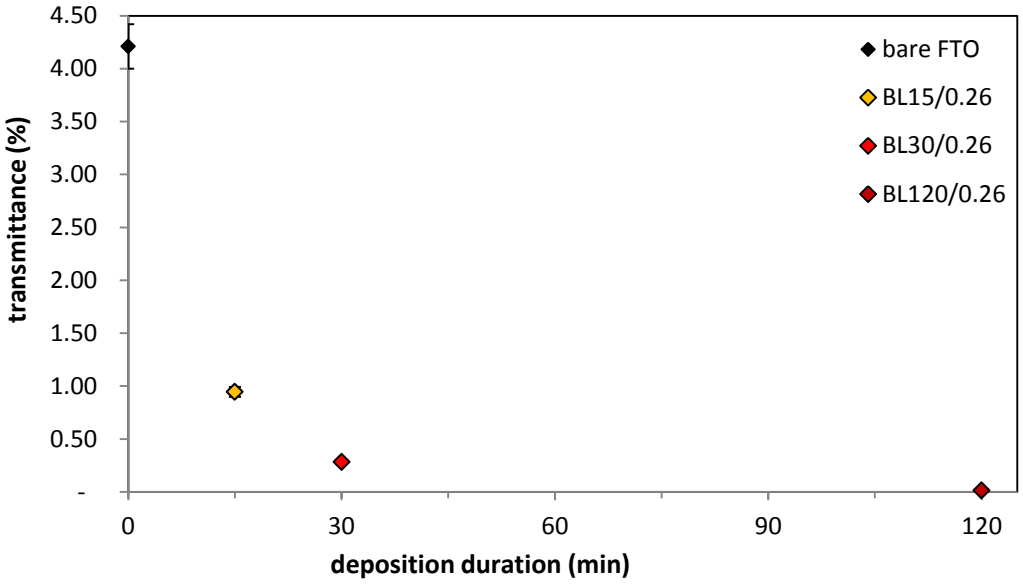

Figure 4.19: Calculated transmittance of FTO glass and samples with BL obtained at p_{O_2} = 0.26 mTorr and at different deposition duration; data in range of 280 - 315 nm. Values are encumbered with 5% error resulting from class B solar simulator.

Table 4.6: Calculated transmittance of FTO glass and samples with BL obtained at p_{O_2} = 0.26 mTorr and at different deposition duration. Values are encumbered with 5% error resulting from class B solar simulator.

sample	deposition duration, t_d (min)	measured spectrum (nm)	transmittance, T (%)
bare FTO	-	280 - 315 (UVB)	4.21 ± 0.211
BL15/0.26	15		0.94 ± 0.047
BL30/0.26	30		0.28 ± 0.014
BL120/0.26	120		0.01 ± 0.001

Transmittance of the samples that was calculated for spectral range corresponding to ultraviolet A, which is between 315 nm and 400 nm, is presented in Figure 4.20. It was observed that the FTO glass transmits the UVA light vastly better than it transmits the UVB. Similarly, the analysed titanium oxide layer

deposited on the FTO glass impairs the transmittance of UVA to a lesser extent than it does with UVB. About 1.5 times less transmitting for UVA is the sample with the thinnest deposited film against the initial transmittance of the bare FTO glass, reaching the value of about 55%. Sample with doubled thickness of deposited film lessens the transmittance further and consequently reaching the value close to 47%. Significant additional attenuation of this light is observed with further increased the film thickness, approaching to 32% of transmittance. Calculated values of transmittance of the UVA light through the samples are presented in Table 4.7.

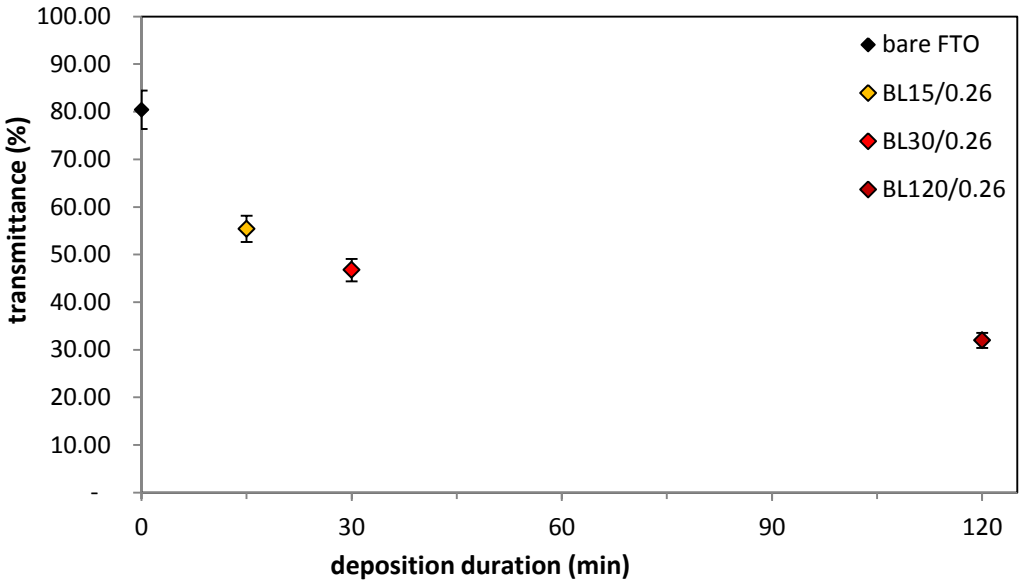

Figure 4.20: Calculated transmittance of FTO glass and samples with BL obtained at p_{O_2} = 0.26 mTorr and at different deposition duration; data in range of 315–400 nm. Values are encumbered with 5% error resulting from class B solar simulator.

Table 4.7: Calculated transmittance of FTO glass and samples with BL obtained at p_{O_2} = 0.26 mTorr and at different deposition duration. Values are encumbered with 5% error resulting from class B solar simulator.

sample	deposition duration, t_d (min)	measured spectrum (nm)	transmittance, T (%)
bare FTO	-	315 – 400 (UVA)	80.40 ± 4.020
BL15/0.26	15		55.38 ± 2.769
BL30/0.26	30		46.74 ± 2.337
BL120/0.26	120		31.97 ± 1.598

Calculated transmittance of the samples for spectral range corresponding to visible light, which is between 400 nm and 750 nm, is shown in Figure 4.21. It can be seen that for this range of wavelength the attenuation of light is smaller than it was for ultraviolet range. The transmittance of the sample with the thinnest deposited film reached about 80% that is around 10% less than transmittance of the bare FTO. On the other hand, it is still significant drop of transmittance in this range of wavelengths in terms of applications which requires extremely high transmittance of visible light. When thickness of the layer was doubled, additional 6% drop of transmittance was observed, so this sample features about 74% transmittance of incident visible light. However, when thickness of the film was further increased, only about 2% drop of transmittance was observed, where it reached close to 73%. Values of transmittance that were calculated for visible light passing through the samples are listed in Table 4.8.

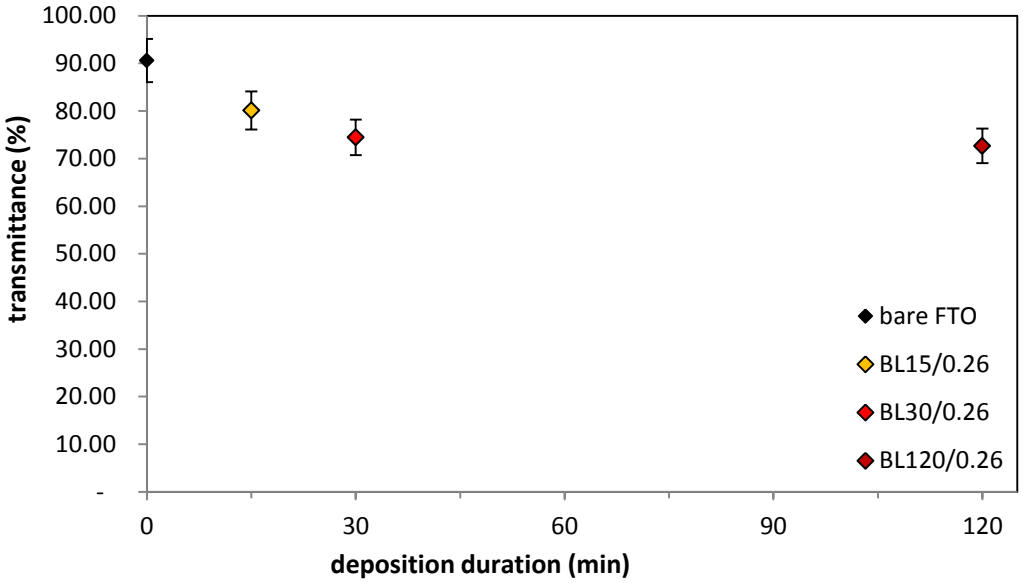

Figure 4.21: Calculated transmittance of FTO glass and samples with BL obtained at p_{O_2} = 0.26 mTorr and at different deposition duration; data in range of 400 – 750 nm. Values are encumbered with 5% error resulting from class B solar simulator.

Table 4.8: Calculated transmittance of FTO glass and samples with BL obtained at p_{O_2} = 0.26 mTorr and at different deposition duration. Values are encumbered with 5% error resulting from class B solar simulator.

sample	deposition duration, t_d (min)	measured spectrum (nm)	transmittance, T (%)
bare FTO	-	400 - 750 (VIS)	90.59 ± 4.529
BL15/0.26	15		80.12 ± 4.006
BL30/0.26	30		74.45 ± 3.722
BL120/0.26	120		72.67 ± 3.634

All the three samples of deposited thin films from TiO target, at 300°C, under low pressure conditions, at oxygen partial pressure of 0.26 mTorr, and at three variant deposition durations, feature light attenuation to some extent within entire range of wavelengths considered in the measurement. Moreover, even the

sample obtained at the shortest deposition time of 15 minutes present noticeable diminishment of transmittance for all studied wavelengths. Light attenuation was found to be enhanced at lower wavelengths of incident light, especially at ultraviolet B, whereas it was less pronounced at longer wavelengths corresponding to visible light when compared to transmittance of bare FTO as reference point. This trend was observed for all three samples of different thickness. Therefore, attenuation coefficient within analysed spectral range will be wavelength dependent. It was also observed that at shorter wavelengths light transmittance was strongly dependent on the film thickness, where quickly approached close to zero percent, whereas transmittance became less dependent at longer wavelengths, where tripled thickness showed only 1% drop and remained considerably high. Therefore it can be assumed that within analysed spectrum of irradiance there is a certain wavelength at which transmittance of the film of this composition will approach to 0% if would be infinitely thick, so its absorbance at this wavelength of light could approach to 100%. At this particular case, relation between sample thickness and light absorbance will be linear thus will follow ideal Beer-Lambert's law calibration curve. At wavelengths shorter than that, there would be positive deviation from linearity and the film thickness will be more critical for good transmittance in that range of spectrum. On the other hand, at wavelengths longer than that, sample of this composition would present negative deviation from linearity and the film thickness will be less important and never reach 0%. For even longer wavelengths of irradiance the transmittance might approach close to 100%, considering the film only, regardless the thickness of the film. From application point of view, use of this film composition in solar cells which are responsive to moderate and shorter wavelengths of visible light might adversely influence their performance due to detectable light attenuation. On the other hand, for solar cells which lifetime performance is strongly decreased due to cell components degradation by ultraviolet light, application of this film might occur beneficial.

4.4.3 Influence of oxygen partial pressure

Figure 4.22 presents spectral transmittance which was calculated, using the equation 4.3.1, from the measurement of spectral irradiance of the light source and the light from that source when it passed through a sample. Analysed samples are those with thin films used as blocking layer in DSSCs, which were deposited via PLD at 300°C, at identical deposition duration and under different oxygen partial pressure. Therefore, analysed films have similar thickness and possible variant structure and composition to some extent. Also calculated transmittance for the bare FTO glass substrate is presented for comparison. A baseline represents the spectral irradiance received by surface of the samples, calculated as reference line. Obtained data are for light spectrum in a range between 280 nm and 800 nm.

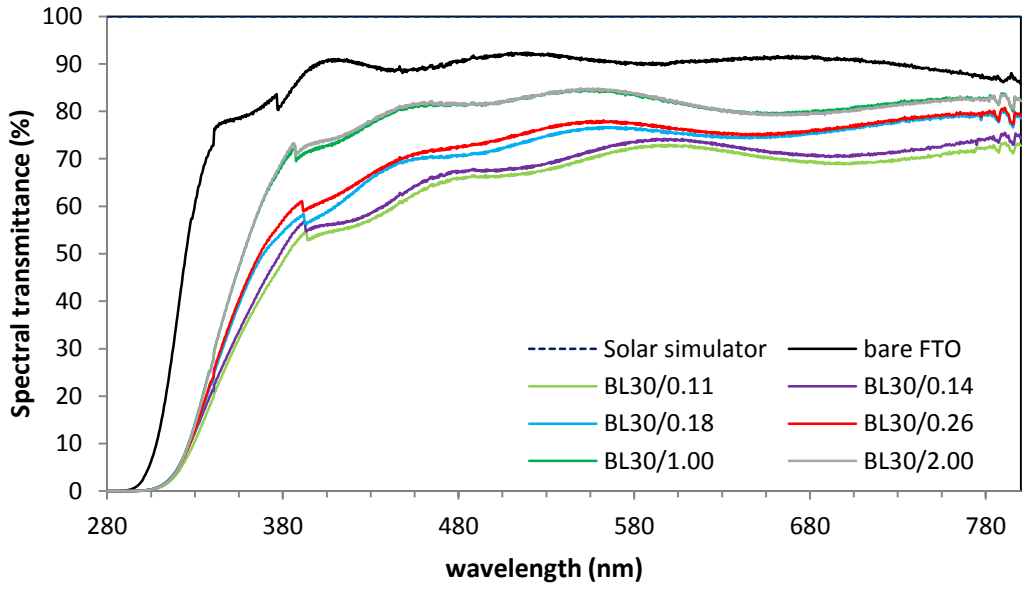

Figure 4.22: Spectral transmittance of FTO glass and samples with BL obtained at t_d = 30 min and under different oxygen partial pressure; data in range of 280 - 800 nm. The discontinuities around 380 nm arise from filter changes in the apparatus.

It was seen that spectral transmittance of each sample with deposited film is lower than spectral transmittance of the bare FTO glass substrate. It was also

observed that transmittance for all six samples is significantly lower than that of the uncoated substrate at vary short wavelengths of analysed spectrum. Moreover, there is no distinct difference between the samples in that region. On the other hand, at moderate and longer wavelengths, a demarcation between the samples can be observed as well as a peculiar trend shows up on the graph. The spectrum of transmittance tends to group in pairs. Each pair is created by samples with neighbouring values of oxygen partial pressure thus three pairs can be recognised. Spectral characteristics of transmittance of each pair is distinguishable and the groups create another trend where a pair of relatively lower p_{O_2} features the lowest spectral transmittance, a pair of relatively higher p_{O_2} features the highest transmittance, and spectral transmittance of samples with relatively moderate values of p_{O_2} is located roughly in the middle of the two other groups. Furthermore, the samples within the pairs seem to follow identical pattern of spectral transmittance with similar values which only differs locally usually presenting higher transmittance for the sample with film deposited at higher oxygen partial pressure.

Transmittance of samples calculated for entire analysed spectrum is plotted in Figure 4.23 as a function of oxygen partial pressure used during the deposition. The general tendency of grouping of values in pairs was repeated. A certain local deviations in spectral transmittance with pairs diversified the samples to some extent, therefore, the group of lowest transmittance consists of samples with values of about 65% and around 67% at oxygen partial pressure of 0.11 mTorr and 0.14 mTorr, respectively. Second group, with relatively moderate transmittance, with calculated values of around 71% and about 72%, consists of samples which oxygen partial pressure during the deposition was 0.18 mTorr and 0.26 mTorr, respectively. Last group of samples, which poses highest transmittance, nearly 79%, comprise of samples obtained at p_{O_2} of 1.00 mTorr and 2.00 mTorr. It can be seen that oxygen partial pressure during the deposition has higher influence on attenuation of light, for entire analysed spectrum, by obtained

films at lower values than it has at higher partial pressures. All calculated values of transmittance for each sample at this spectrum range are listed in Table 4.9.

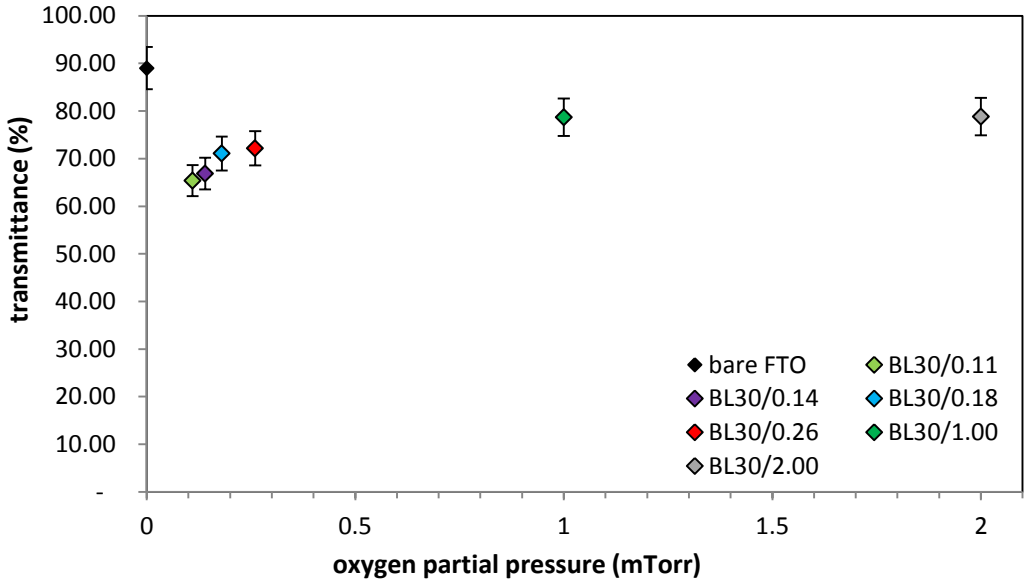

Figure 4.23: Calculated transmittance of FTO glass and samples with BL obtained at t_d = 30 min and under different oxygen partial pressure; data in range of 280 - 800 nm. Values are encumbered with 5% error resulting from class B solar simulator.

Table 4.9: Calculated transmittance of FTO glass and samples with BL obtained at t_d = 30 min and under different oxygen partial pressure. Values are encumbered with 5% error resulting from class B solar simulator.

sample	oxygen partial pressure, p_{O_2} (mTorr)	measured spectrum (nm)	transmittance, T (%)
bare FTO	-	280 - 800	89.01 ± 4.450
BL30/0.11	0.11		65.38 ± 3.269
BL30/0.14	0.14		66.84 ± 3.342
BL30/0.18	0.18		71.08 ± 3.554
BL30/0.26	0.26		72.19 ± 3.609
BL30/1.00	1.00		78.72 ± 3.936
BL30/2.00	2.00		78.81 ± 3.940

Figure 4.24 shows transmittance of samples calculated for spectral range corresponding to ultraviolet B, which is between 280 nm and 315 nm, as a function of oxygen partial pressure used during the deposition. For this spectrum of irradiance the samples do not show any of the trends observed for entire measured spectrum. The only distinct feature is that the transmittance for all samples is about 16 times lower than transmittance of the bare FTO glass. The sample with film deposited at highest oxygen partial pressure has transmittance of 0.26% and samples for which used oxygen partial pressure was less and less present increase of transmittance to some extent, where reach value of 0.30% for samples at p_{O_2} of 0.18 mTorr and 0.14 mTorr. In contradiction to this tendency, sample with film obtained at lowest oxygen partial pressure feature also the lowest transmittance, which equals to 0.22%. Therefore, it can be concluded that presence of any titanium oxide film deposited within these conditions has significant influence on attenuation of UVB light, but variation in oxygen partial pressure during their deposition does not affect the transmittance largely. List of all calculated values of transmittance for each sample at UVB spectrum of radiation is in Table 4.10.

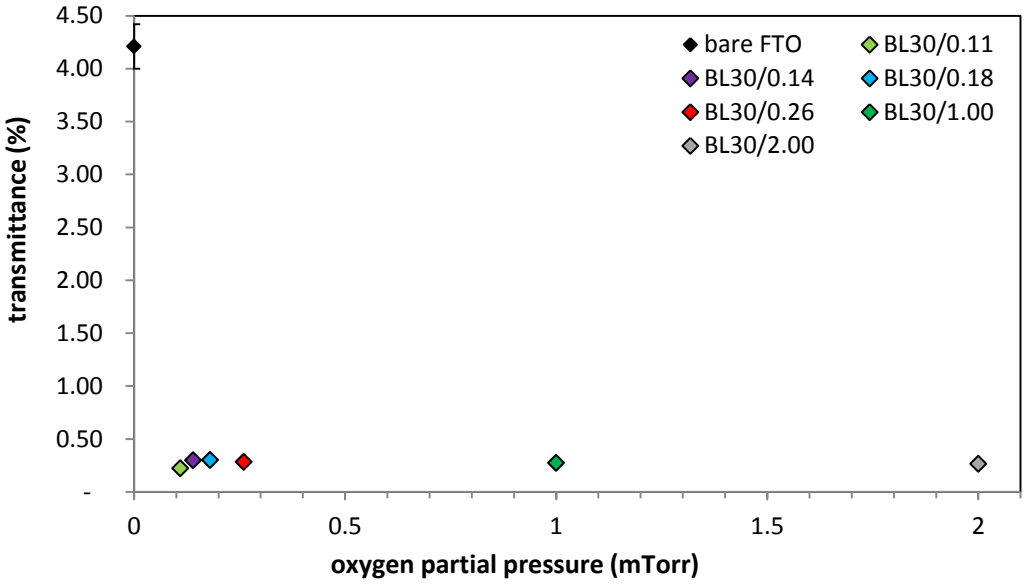

Figure 4.24: Calculated transmittance of FTO glass and samples with BL obtained at t_d = 30 min and under different oxygen partial pressure; data in range of 280 - 315 nm. Values are encumbered with 5% error resulting from class B solar simulator.

Table 4.10: Calculated transmittance of FTO glass and samples with BL obtained at t_d = 30 min and under different oxygen partial pressure. Values are encumbered with 5% error resulting from class B solar simulator.

sample	oxygen partial pressure, p_{O_2} (mTorr)	measured spectrum (nm)	transmittance, T (%)
bare FTO	-	280 - 315 (UVB)	4.21 ± 0.211
BL30/0.11	0.11		0.22 ± 0.011
BL30/0.14	0.14		0.30 ± 0.015
BL30/0.18	0.18		0.30 ± 0.015
BL30/0.26	0.26		0.28 ± 0.014
BL30/1.00	1.00		0.27 ± 0.014
BL30/2.00	2.00		0.26 ± 0.013

Transmittance of the samples calculated for spectral range corresponding to ultraviolet A, which is between 315 nm and 400 nm, as a function of oxygen partial pressure used during the deposition, is shown in Figure 4.25. In this spectrum of irradiation values of transmittance begin to diverge and resemble the global tendency noticed for entire spectrum of the measurement. However, the sizable difference between transmittance of samples with thin film and that of the bare FTO glass is still observed. Despite it largely improved, in this case it totals over one third of the transmittance of the bare FTO substrate. Two samples with film deposited at highest oxygen partial pressure feature the highest transmittance of about 56% and noticeably deviate from the other samples, which transmittance towards lower values of p_{O_2} tend to nonlinearly decay. These four samples do not group in pairs of similar value of transmittance at this spectrum of irradiance. The lowest obtained value of transmittance, close to 40%, presents the sample with film deposited at oxygen partial pressure of 0.11 mTorr. Change in transmittance of the samples at UVA spectrum of irradiance shows property of transition stage of transmittance where its value for all samples evolve from low at UVB to higher at longer wavelengths. As transmittance of the two samples of film deposited at highest p_{O_2} demonstrate this transition earlier and group in pair quicker than for other samples, it can be assumed that samples prepared under this conditions contain bigger amount of a component which features higher transmittance in ultraviolet light. All calculated values of transmittance for the samples at UVA spectrum of radiation are listed in Table 4.11.

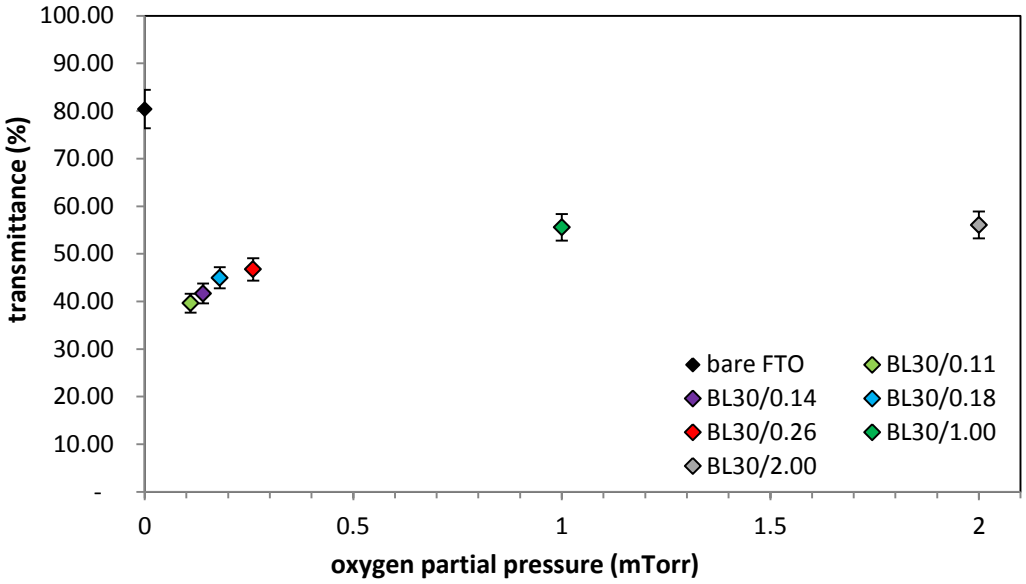

Figure 4.25: Calculated transmittance of FTO glass and samples with BL obtained at t_d = 30 min and under different oxygen partial pressure; data in range of 315 - 400 nm. Values are encumbered with 5% error resulting from class B solar simulator.

Table 4.11: Calculated transmittance of FTO glass and samples with BL obtained at t_d = 30 min and under different oxygen partial pressure. Values are encumbered with 5% error resulting from class B solar simulator.

sample	oxygen partial pressure, p_{O_2} (mTorr)	measured spectrum (nm)	transmittance, T (%)
bare FTO	-	315 - 400 (UVA)	80.40 ± 4.020
BL30/0.11	0.11		39.63 ± 1.981
BL30/0.14	0.14		41.68 ± 2.084
BL30/0.18	0.18		44.97 ± 2.249
BL30/0.26	0.26		46.74 ± 2.337
BL30/1.00	1.00		55.54 ± 2.777
BL30/2.00	2.00		56.07 ± 2.803

Figure 4.26 presents the relation between transmittance of prepared samples and oxygen partial pressure used for their preparation, where the transmittance was calculated for spectrum of visible light, which is between 400 nm and 750 nm. In this wide range of wavelengths, all observed trends of the data are approximations of observed trends and values obtained for entire measured spectrum of transmitted light, which are decoupled from influence of extreme values that are portions of ultraviolet and infrared spectrum. Therefore, in this case values of transmittance tend to group in pairs in a sequence of decreasing partial pressure. The highest transmittance, of 81% was obtained for samples prepared at highest oxygen partial pressure. Noticeable drop of the value to about 74% is observed for samples at moderate content of oxygen used during their preparation and then the lowest values of about 69% were obtained for samples prepared at lowest p_{O_2}. Most of the values of transmittance are increased of 2% against their equivalent calculations for entire measured spectrum. This is mostly related with transmittance of the FTO glass, used as substrate for the films, which is also higher of 2% in visible range than it is calculated for entire spectrum. Only sample with the film deposited at the lowest oxygen gas concentration has more enhanced value of transmittance, of additional 3%, which means that the transmittance of this sample considering entire measured spectrum is more affected by transmittance in ultraviolet than it occurs for all other samples. It is clearly seen from observed trends that samples with film deposited under higher oxygen partial pressure present higher transmittance than samples prepared under lower oxygen pressure conditions and small variations in oxygen concentration during the process affect the transmittance to much smaller extent thus values tend to group. All values of transmittance calculated for the samples at visible spectrum of radiation are listed in Table 4.12.

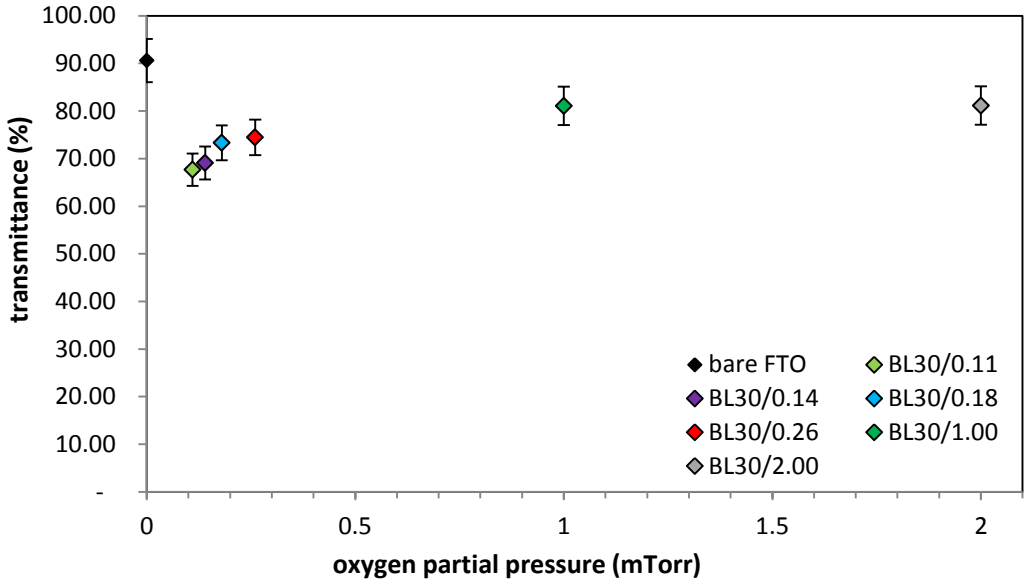

Figure 4.26: Calculated transmittance of FTO glass and samples with BL obtained at t_d = 30 min and under different oxygen partial pressure; data in range of 400 - 750 nm. Values are encumbered with 5% error resulting from class B solar simulator.

Table 4.12: Calculated transmittance of FTO glass and samples with BL obtained at t_d = 30 min and under different oxygen partial pressure. Values are encumbered with 5% error resulting from class B solar simulator.

sample	oxygen partial pressure, p_{O_2} (mTorr)	measured spectrum (nm)	transmittance, T (%)
bare FTO	-	400 - 750 (VIS)	90.59 ± 4.529
BL30/0.11	0.11		67.65 ± 3.383
BL30/0.14	0.14		69.06 ± 3.453
BL30/0.18	0.18		73.34 ± 3.667
BL30/0.26	0.26		74.45 ± 3.722
BL30/1.00	1.00		81.07 ± 4.054
BL30/2.00	2.00		81.14 ± 4.057

All the six samples of deposited thin films from TiO target, at 300°C, at identical deposition duration of 30 minutes, under low pressure conditions, at six

variant oxygen partial pressures between 0.11 mTorr and 2.00 mTorr, feature light attenuation to some extent within entire range of wavelengths considered in the measurement. The reduction of transmittance of theses samples was at least 10% when compared with transmittance of their bare substrate, which was the FTO glass. The highest light attenuation occurred in ultraviolet B spectrum, couple of times less significant in ultraviolet A spectrum, and even less considerable in visible range of incident light, but detectable as 10% or more drop of transmittance. In the global range, oxygen partial pressure used for the deposition has evident influence on transmittance in entire considered spectrum of light, especially in VIS spectrum, and the transmittance decrease with the decrease of oxygen gas pressure. On the other hand, in the local ranges, big difference between used oxygen partial pressures has smaller influence on change in transmittance at shortest wavelengths, where global trend of transmittance decay towards lower pressures declines. Also, relatively small differences between oxygen pressures have much less effect on the transmittance in all considered spectrums. Due to those small variations, values of transmittance tend to group in pairs in relation to closely related values of oxygen partial pressure. Therefore, it might indicate that samples of films prepared under these paired conditions have similar composition and structure thus result in similar optical properties.

Due to the global trend of transmittance increase towards higher oxidative deposition conditions, it can be assumed that the amount of a component or a structure featuring higher transmittance must increase in the films when chosen oxygen partial pressure increases. Consequently, a bandgap of the film must somewhat increase as well. Among all possible compounds of Ti-O system, a material that can poses high visible transmittance and also partially ultraviolet transmittance is titanium dioxide (TiO_2). Moreover, it can form at least two crystallographic phases that are stable and have good ultraviolet transmittance to some extent. These are anatase and rutile, and their main difference is width of the bandgap. Anatase phase has bandgap of about 3.2 eV thus feature higher ultraviolet and visible transmittance than rutile phase, which has bandgap of about

3.0 eV. Increased light transmittance for films deposited at higher oxygen partial pressure suggests that increased formation of anatase phase must occur at these conditions. XRD analysis showed that anatase phase is present, and with higher oxygen partial pressures intensity of some peaks related to this phase was enhanced, which means that the content of this phase could increase. However, rutile phase was found as well and amount of this phase was found to be greater than anatase. Moreover, intensities of some of the peaks related to rutile also were enhanced by higher oxygen partial pressure thus amount of this phase was found to increase even more, therefore, in total, amount of rutile phase in the film was assumed to increase with increase of oxygen partial pressure. Thus, these two hypothesis, where higher oxygen gas concentration during the process favours formation of rutile phase and in the same time favours formation of the phase with wider bandgap, that is anatase, are in contradiction. On the other hand, it was also assumed that the amount of TiO_2, due to increased intensities of some peaks of both phases, could increase with increased oxygen partial pressure. Therefore, this could increase transmittance of the films obtained at higher oxygen gas concentrations. However, in this case, some other compound or compounds must be present in the films obtained at low oxygen partial pressures and it or their amount should be significant to affect the transmittance, but XRD analysis did not match any other phases to the diffraction patterns of the prepared films. Thus, this hypothesis cannot be unambiguously confirmed or denied.

From application point of view, use of these films in solar cells which are responsive to moderate and shorter wavelengths of visible light and ultraviolet might to some extent adversely influence their performance due to detectable light attenuation in that spectrum. On the other hand, for solar cells which lifetime performance is strongly dependent on ultraviolet light, due to cell components decomposition by UV, application of these films might occur beneficial. Moreover, possibility of selection of oxygen partial pressure and duration of the deposition of such films by PLD can be used for fine tuning of ultraviolet

transmittance of the film, even with division into UVA and UVB light without changing visible transmittance very significantly.

4.5 Electrical resistance

4.5.1 2-point probes measurement method

Electrical resistance (R) is one of the electrical properties of materials. It quantifies the difficulty to pass an electrical current through a material and is defined as the ratio of voltage (V) across the material to current (I) passing through it. Many different materials feature direct proportionality between the voltage and the current thus the resistance is constant, which is known as Ohm's law. Materials or objects that fulfil this law are called *ohmic*. In other cases, when materials or objects do not feature direct proportionality between the current and the voltage, thus the resistance varies, they do not obey this law and are called *non-ohmic*.

Measurement of resistance is often performed by using an ohmmeter. Those meters of simpler design apply the voltage to the resistance and measure the current through the resistance. More accurate ohmmeters are capable of passing a constant current through the resistance and measuring the voltage across it. Measurement of resistance can be carried out in one of two configurations. In the one that is often called 2-point probes method a test current is passed through the same pair of leads that measure the voltage across the resistance. This method is simpler and more usual. In the other one which is often called 4-point probes method the pair of current-currying probes is separated from the pair of voltage-sensing probes. This method is more accurate, especially for low resistances measurements, as reduces the effect of test lead resistance.

In this research, two types of measurements were conducted to characterise the electrical resistance of deposited films. Both types of measurements were performed using 2-point probes method. First measurement

was carried out with use of a high-performance digital multimeter, and second as current-voltage (I-V) characteristics with the aid of a potentiostat.

First measurement was done by contacting two probes at the surface of the deposited film. Electrical contacts were achieved by pressure contact between the probes and the sample. The probes were components of a multifunctional probes apparatus (García-Cañadas & Min 2014), which were fabricated using a Cu tube, which tip was swaged into a pencil point and eventually electroplated with Cu to ensure that the measured sample is always in contact with copper. The probes were held by micropositioners (Quarter Research XYZ-300-M), which were attached to a top platform. The use of micropositioners allows to move the probes in all directions to approach them to the sample, regardless its geometries. The probes in this measurement were set to a fixed distance of 1 mm. The measured sample was located on a motorised vertical stage (8MVT100-25-1, Standa) fixed to a bottom platform. The stage was controlled via computer which allowed to approach the sample to the probes slowly and apply them on the film each time with the same pressure, as overall thickness of the samples was constant and the probes were fixed at their positions throughout the experiment. The probes were connected to a digital multimeter (2000 Multimeter, Keithley), which allowed to measure a static resistance between the test probes. All the samples have exactly the same geometry, therefore, there was no need to reposition the probes. The measurement of the resistance was taken nine times for each sample. Three measurements were taken with probes positioned along the axis of symmetry of the sample. Then, the probes were repositioned twice by shifting the sample perpendicularly to the line created by the probes, and the measurements were taken three times consecutively at each new location. This was done in order to avoid a measuring error that could arise from possible damage of the surface of the sample by the probes. Identical contacts for each measurement were provided by repositioning or replacing the sample on the sample holder and elevating it along with the motorised stage towards the probes fixed at their positons. The measuring setup allows to avoid the need to use solder

or conductive paints in order to achieve satisfactory contacts with the sample due to use of the micropositioners which arms are mounted with optimal contacting angle. Setup for this measurement is shown in Figure 4.27. Using this method, all the samples deposited as BL for DSSC were investigated.

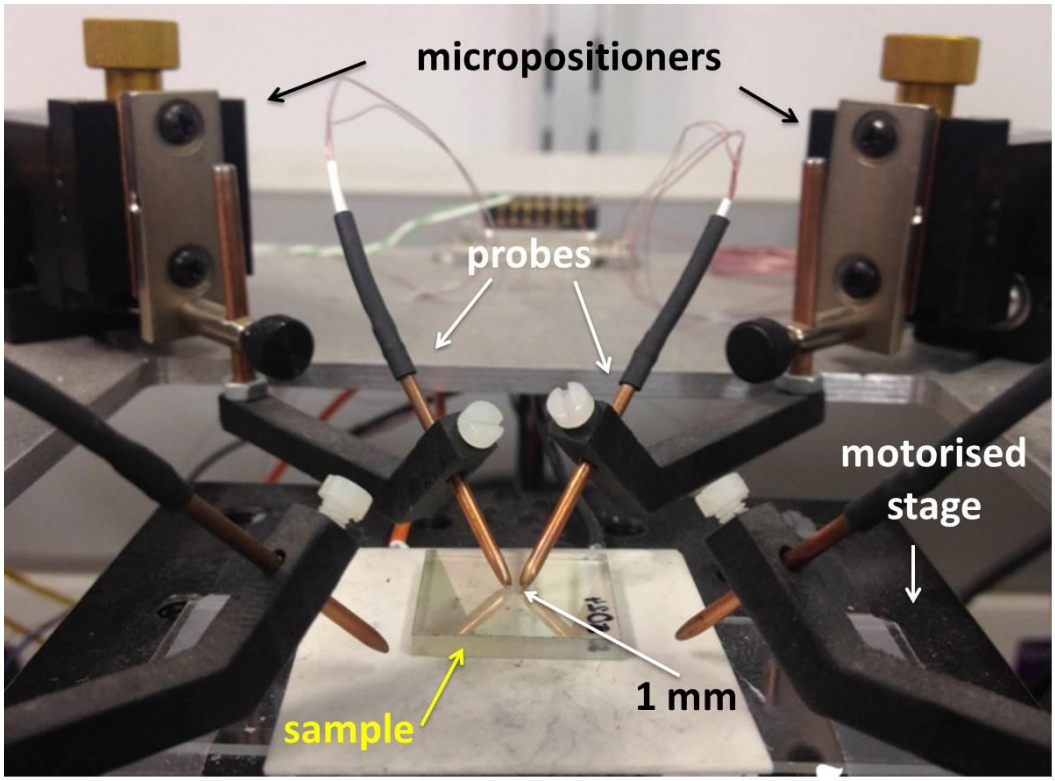

Figure 4.27: Setup for measurement of resistance using 2-point probes method by digital multimeter.

A second method of measuring the resistance was performed to study an interfacial resistance by investigating the charge transfer characteristic at the interface of the deposited layer and FTO substrate via I-V characteristics. In this measurement, one probe was contacted with the sample in the centre of the deposited film, where normally mesoporous TiO_2 nanostructure is screen-printed during fabrication of DSSCs. Another probe was contacted with the sample at fixed distance of 1 cm from the first probe, in the centre of the exposed edge of the FTO substrate, where normally silver paint is applied for electrical contact

during fabrication of DCCS. In this way, the current that passes through the sample during the measurement has to come the same way as current that flows during DSSC operation. The probes used in this setup were standard multimeter test leads probes. In order to achieve equal pressure contact between the probes and the sample, an appropriate weight was attached to each probe. The contact force applied by the probes was tested by applying probes on a portable electronic balance placed under the probes at the position where the samples were tested. The weight on each probe was adjusted to give about 45 g of weight on the balance. Each probe was fixed to a lever, with optimal contacting angle, which allowed to raise the probes individually after each measurement ensuring that the contact pressure between the probes and the sample is constant throughout the experiment. The measured sample was located on a stationary stage and the probes were individually contacted with the sample at appropriate position and at the fixed distance from each other. Entire setup was enclosed in the Faraday cage to avoid any influence of electromagnetic radiation that would be for instance absorbed by the sample and alter the measured value. The measurement setup is shown in Figure 4.28. The leads from the probes were plugged into a potentiostat (PGSTAT302N, Metrohm Autolab). All the measurement procedure was controlled using computer control software. The range of applied potential for current-voltage characteristics of the samples was from -1 V to 1 V, thus the current flow between the deposited film and the FTO layer was measured under forward bias, which was from the film to the FTO, and under reverse bias, which was from the FTO to the film, which correspond to the forward and reverse bias conditions during the I-V characterisation of fabricated DSSCs. Each sample was measured three times, and each measurement consisted of two cycles of forward and revers bias. Between each measurement, the probes were raised and reapplied on the sample. The first two measurements were taken with probes applied in the same position, and the third measurement was taken with the off-set of 1 mm from the previous position. This was done to test the repeatability of the results obtained via the setup. The measurements were taken with step potential of 5 mV

and at the scan rate of 50 mV/s. Initial test of the measurement setup was performed on bare FTO glass substrate and a practise test sample of thin film, which obtained at 300°C, at deposition duration of 120 minutes, under total pressure of 2 mTorr and oxygen partial pressure of 0.40 mTorr. Next samples studied with use of this measurement setup were samples of thin films deposited as blocking layers for DSSCs. However, these samples were earlier studied in the SEM microscopy where had to be coated with a thin layer of electrically conductive carbon-coating, due to the fact that although the samples consist of well conducting FTO layer, the vast majority of their volume is made of glass, thus at large are considered as electrically insulating samples. It was found that the carbon coating adversely influenced the properties of the deposited films of titanium oxide, therefore, only results obtained from the practise test sample, bare FTO glass – uncoated, and FTO glass – carbon coated are presented and discussed in this chapter, and all other data obtained for carbon coated BL samples are presented in the appendix.

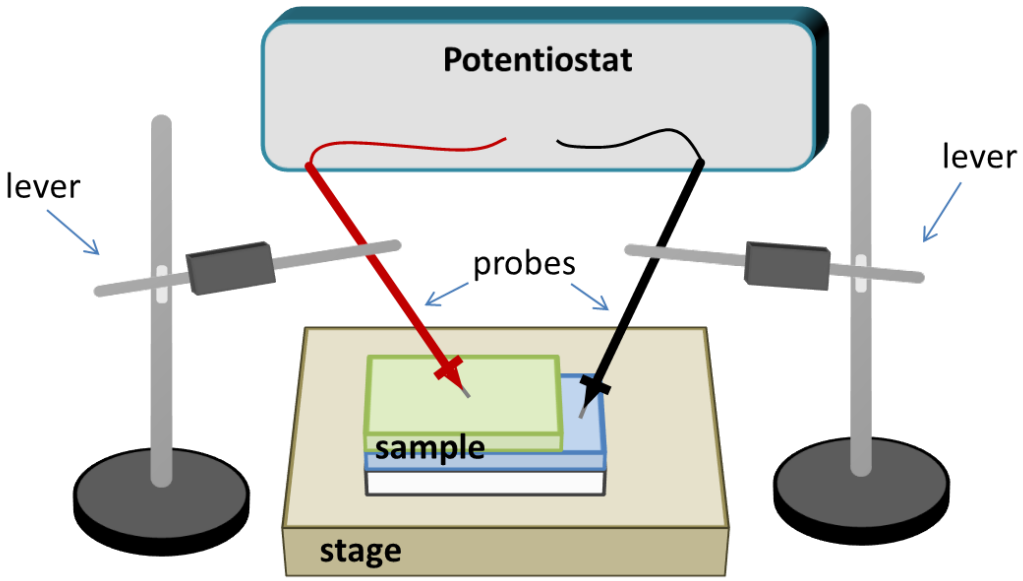

Figure 4.28: Setup for I-V characterisation using 2-point probes method by potentiostat. The distance between the electrodes is fixed and equals 1 cm.

4.5.2 Influence of deposition duration

Figure 4.29 shows data of electrical resistance of bare FTO substrate and thin films, deposited via PLD under oxygen partial pressure of 0.26 mTorr, as a function of deposition duration. Presented data are averaged values of several measurements of the resistance taken for each sample via the high-performance digital multimeter. Each averaged value is presented along with error bars that represent one standard deviation (SD) of uncertainty of the measurement. The averaged values and their errors of estimation along with other discussed parameters are detailed in Table 4.13.

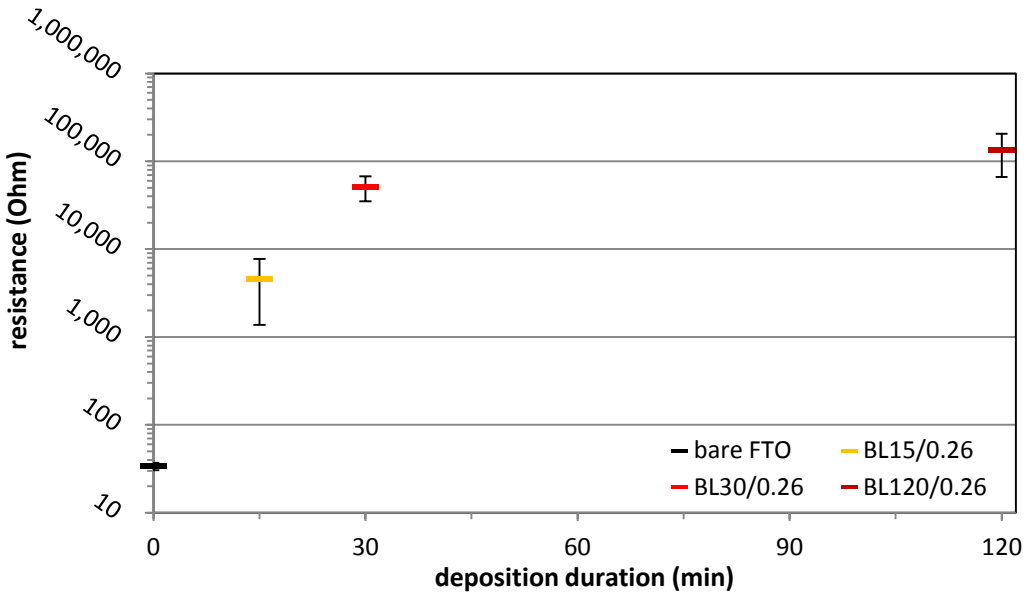

Figure 4.29: Electrical resistance of the bare FTO substrate and samples with BL obtained at p_{O_2} = 0.26 mTorr, at different deposition durations.

Table 4.13: Results from electrical resistance measurement for the bare FTO substrate and samples with BL obtained at p_{O_2} = 0.26 mTorr; including errors of estimation and deposition conditions.

sample	deposition duration, t_d (min)	oxygen partial pressure, p_{O_2} (mTorr)	approximate film thickness, d_f (nm)	electrical resistance - averaged (Ω)	standard deviation, *SD* (Ω)	standard error, *SE* (Ω)
bare FTO	-	-	-	34	3	1
BL15/0.26	15	0.26	30	4,554	3,185	1,062
BL30/0.26	30		54	51,222	16,269	5,423
BL120/0.26	120		149	135,722	69,514	23,171

It can be explicitly seen that the averaged resistance of the sample with thin film deposited at shortest deposition duration is 4554 Ω and is higher by two orders of magnitude in comparison to the resistance obtained for the bare FTO substrate, which is 34 Ω. As the thickness analysis showed that this film has the thickness of about 30 nm, it is immediately seen that the deposited film, even if it is such thin, has strong influence on the resistance and other resulting electrical properties. However, the technique of the resistance measurement conducted in this experiment does not provide enough information about the actual path of the current flowing through the sample, therefore, does not inform about possible obstacles. It rather gives information about the current flow through the sample as a whole, which is a multi-stack of layers, where current is injected and collected at the top layer. Thus, this measurement technique can give useful preliminary information about the sample at large as, for instance, in case of the bare FTO sample it confirmed its good conductivity as well as provided information about possible type of contact between this layer and the test probes. As the resistance in this case was very law, there was no considerable obstacle for current to be injected to and collected from the FTO. Therefore, the created contact between the probes and the FTO was ohmic-type. In the case of the thinnest titanium oxide film sample, it can be assumed that there was some difficulty for current flow that could be assigned to high resistance of the deposited film, or non-ohmic contact

between the probes and the deposited film, or non-ohmic contact between the titanium oxide film and the FTO layer, or any combination of these. Other possibilities, like poor quality contact between the probes and the sample or poor quality contact between the deposited film and the FTO layer can be negated as the measurement setup was design to eliminate the former, and the cross-sectional images of the deposited films clearly showed that each deposited film has intimate contact with the FTO substrate, which eliminates the latter possibility.

The averaged resistance of the sample deposited at 30 minutes is over 51.2 kΩ, which is higher by one order of magnitude in comparison with its thinner analogue sample. Thickness analysis showed that the thickness of the deposited film for this sample was close to 54 nm. All deposition conditions, except the deposition duration, were identical for both samples thus the only difference between them is their thickness. Similar trend was observed for the thickest sample. Its thickness was assessed to be about 149 nm, and obtained averaged resistance is about 135.7 kΩ that falls into next range of resistance which is higher by one order of magnitude in comparison to the previous sample. All thin films in this group were deposited under identical conditions other than the deposition duration thus their structure and composition is assumed to be identical. All these films were deposited on identical substrate of the same size which was subsequently cut into quadrants, and properties of one quadrant of each full-sized sample is analysed in this chapter. Therefore, only the thickness of the films is the difference between the samples, whereas other dimensions of the films remain the same. Although the variation between each measurement of the resistance for a sample is significant, which is represented by considerable values of standard deviations, the general trend of thickness dependence of the resistance is conserved, and shows that the thicker the deposited film the higher is the resistance.

Two possible types of paths of the current flow through the analysed samples during this experiment can be proposed for this measurement technique, which are shown in the Figure 4.30. First possibility occurs when the test current

passes through the deposited film only or when this path of the current is dominant. Second possibility occurs when the only or dominating path for test current is across the deposited film towards the FTO layer and through the barrier, next through that layer, and then through the barrier again and afterwards away from it across the deposited film to another contacted probe.

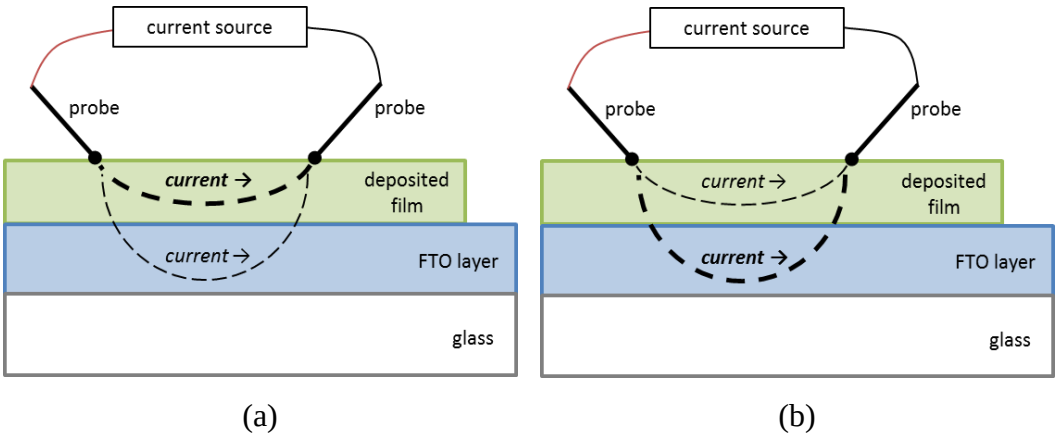

(a) (b)

Figure 4.30: Proposed paths of the current flow through the sample during the measurement; (a) dominant path through deposited film, (b) dominant path across the deposited film and mainly through FTO layer.

As the composition and structure of analysed group of samples is invariable, the type of electrical contacts between the probes and deposited film as well as between the film and the FTO layer does not change, regardless of their kind, when the thickness of the film is different among these samples. Consequently, the specific electrical resistance of the material itself that composes the film is constant, as it is an intrinsic property of the material considered to be independent of its geometry.

In the case of the first proposed path of the current flow, the increase of the thickness of the deposited film should result in decrease of the resistance, as the distance between the probes for each measurement was constant and the area through which the current passes was increased by the film thickness. However, the trend of the relation between the measured resistance and obtained thickness for the samples is opposite. Therefore, the second proposed path of the current

flow is more plausible. In this scenario, the path of the current flow takes place along different lines in relation to the film geometry. Therefore, increase of the film thickness leads to increase of the length of the path of the current. Although the contribution of the film thickness to the total length of the path is extremely small, thousand times due to the distance between the probes, this part of the path is through the very resistive material thus it plays an important role in current flow in this setup. For this reason, the increase of the film thickness leads to proportional increment of contribution of the very resistive section of the path, and consequently increases a total resistance in the created electrical circuit. The total resistance is the value that is at bottom measured in this setup. Obtained results of the electrical resistance do not determine what type of electrical contact was created between the deposited film and the FTO layer or between the film and the probe. Nevertheless, they indicate that most probable path of the current flow is like that presented in Figure 4.30(b), where all encountered resistances at contacts between the film and the FTO layer and through the FTO layer are a smaller obstacle than the resistance along the deposited film itself (see Figure 4.30(a)).

4.5.3 Influence of oxygen partial pressure

Figure 4.31 presents data of electrical resistance of the bare FTO substrate and thin films, deposited via PLD at deposition duration of 30 minutes, as a function of oxygen partial pressure used for their deposition. Presented data of the resistance are averaged values of several measurements taken for each sample via the high-performance digital multimeter. All averaged values are presented along with their error bars represented by one standard deviation (SD) of uncertainty of the measurement. All the averaged resistances and their errors of estimation are detailed in Table 4.14 along with other discussed parameters.

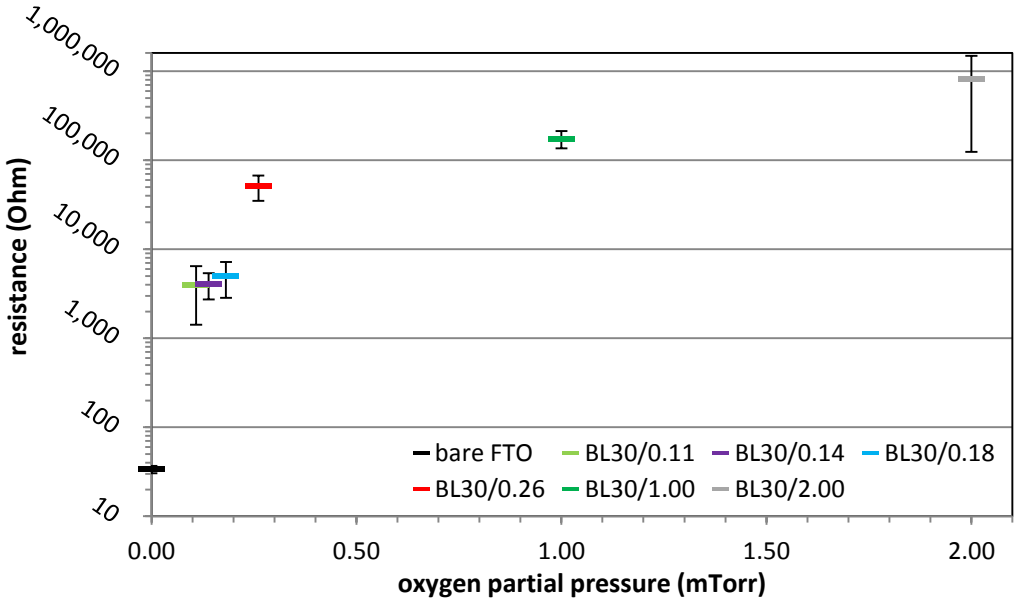

Figure 4.31: Electrical resistance of the bare FTO substrate and samples with BL obtained at t_d = 30 min, under different oxygen partial pressures.

Table 4.14: Results from electrical resistance measurement for the bare FTO substrate and samples with BL obtained at t_d = 30 min; including errors of estimation and deposition conditions.

sample	deposition duration, t_d (min)	oxygen partial pressure, p_{O_2} (mTorr)	approximate film thickness, d_f (nm)	electrical resistance - averaged (Ω)	standard deviation, *SD* (Ω)	standard error, *SE* (Ω)
bare FTO	-	-	-	34	3	1
BL30/0.11	30	0.11	53	3,939	2,520	840
BL30/0.14		0.14		4,056	1,331	444
BL30/0.18		0		5,019	2,182	727
BL30/0.26		0		51,222	16,269	5,423
BL30/1.00		1		174,889	38,459	12,820
BL30/2.00		2		808,611	684,299	228,100

It can be notably seen that the resistance of any measured sample is higher than the resistance of bare FTO substrate by at least two orders of magnitude. Averaged resistance for the film deposited at the lowest oxygen partial pressure, which was 0.11 mTorr, amounts to almost 4 kΩ and is the lowest value obtained for this group of samples. This indicates that the presence of titanium oxide films deposited on the FTO increases the total electrical resistance of the sample as a whole in the created electrical circuit of this measurement setup. However, the contribution of the specific electrical resistance of the material itself that composes the film as well as type of created electrical contacts between the deposited film and FTO layer or applied probes cannot be defined. Nonetheless, indication of a certain trends of the influence of the oxygen partial pressure on resistance of the samples is still possible to conclude.

Measurement of two subsequent samples of films deposited under oxygen partial pressure of 0.14 mTorr and 0.18 mTorr demonstrated the resistances of about 4 kΩ and 5 kΩ, respectively. All of the analysed films in this group were deposited at identical deposition duration of 30 minutes and on identical FTO glass substrate thus their thickness was assumed to be similar, which was confirmed by thickness analysis where values of the thickness oscillated about 53 nm. Therefore, all the differences of measured resistances for these compared samples should result only from the composition and the structure of the films, not from their geometry. In that case, obtained similar values of the resistance for all three mentioned samples might indicate that they possess similar specific resistance and create similar types of electrical contacts, and are probably similar in terms of structure and composition. The calculated values of standard deviations for measurement of those samples are fairly large and they overlap significantly thus in terms of order of magnitude of the resistance, those samples are very alike. Results from the optical transmittance measurement showed meaningful similarity between two films deposited at the lowest used oxygen partial pressure, therefore observation of similar electrical resistance can support the conclusion about their similarity. Close value of the sample BL30/0.18 might

result from the measurement setup that measures the resistance of the sample at large, including all contact resistances.

The resistance of the sample deposited at oxygen partial pressure of 0.26 mTorr was estimated to about 51.2 kΩ, which is higher by one order of magnitude compared to the prior samples. This sample was also analysed in terms of film thickness dependence of the measured resistance and it was concluded that for this particular conditions of oxygen partial pressure the path of the current flow is most likely as proposed in Figure 4.30(b). However, based on the results obtained in this experiment for those samples with possible varied compositions but with only one exemplary thickness for each, it is not possible to conclude the path of the current flow in those.

Two another samples of thin films deposited at 1.00 mTorr and 2.00 mTorr of oxygen partial pressure demonstrated the electric resistance of about 174 kΩ and 809 kΩ, respectively. Although these two values of resistance fall into the same order of magnitude, they are close to the extremes of this range of resistance. Therefore, they should be considered as a further, significant, and gradual gain in resistance.

Despite large variations in measurement of resistance for each sample, the general trend of the electrical resistance of the samples as a function of oxygen partial pressure used for the films depositions is conserved. The higher the partial pressure the higher is the resistance. Considering chosen setup of the measurement, it cannot be clearly concluded which current flow mechanism is responsible for this increase. There are several possibilities, like change of the path of the current flow through the sample, change of the specific electrical resistance of the film material, change of the type of the electric contacts at interfaces or any combination of those possibilities. Nevertheless, the origin of those changes has to indicate to some change in the structure or composition of the films influenced by oxygen partial pressure during their growth. The only unambiguously noticed change in the films structure and composition was increased formation of rutile phase of TiO_2 over anatase phase of TiO_2 with

increase of oxygen partial pressure. However, the rutile phase has bandgap of about 3.0 eV while Anatase phase has bandgap of about 3.2 eV, therefore, with increase amount of the former, it was expected to observe decrease of the resistance. The observed increase of the resistance is, however, substantial and indisputable. On the other hand, it was also proposed that amount of TiO_2 as a whole could increase along with increase of the p_{O_2}. In that case, it will cause increase of the amount of the compound possessing the highest possible bandgap among all common compounds from Ti-O system. Consequently, the specific electrical resistance of the deposited film would be expected to increase as well. This hypothesis cannot be verified based on conducted experiments and obtained results in this study.

4.5.4 I-V characteristics

Figure 4.32 presents data of current-voltage (I-V) characteristics of the bare FTO substrate that were obtained with the aid of the potentiostat. The range of applied potential was from -1 V to 1 V. The sample was measured three times and results from each single measurement are presented in Figure 4.32(a)-(c). Each measurement consisted of two cycles of forward and revers bias. Between each measurement, the probes were raised and reapplied on the sample. First two measurements were taken with probes applied in the same position, and third measurement was taken with the off-set of 1 mm from the previous position of the probes. General position of the probes on the measured sample is depicted in Figure 4.32(d).

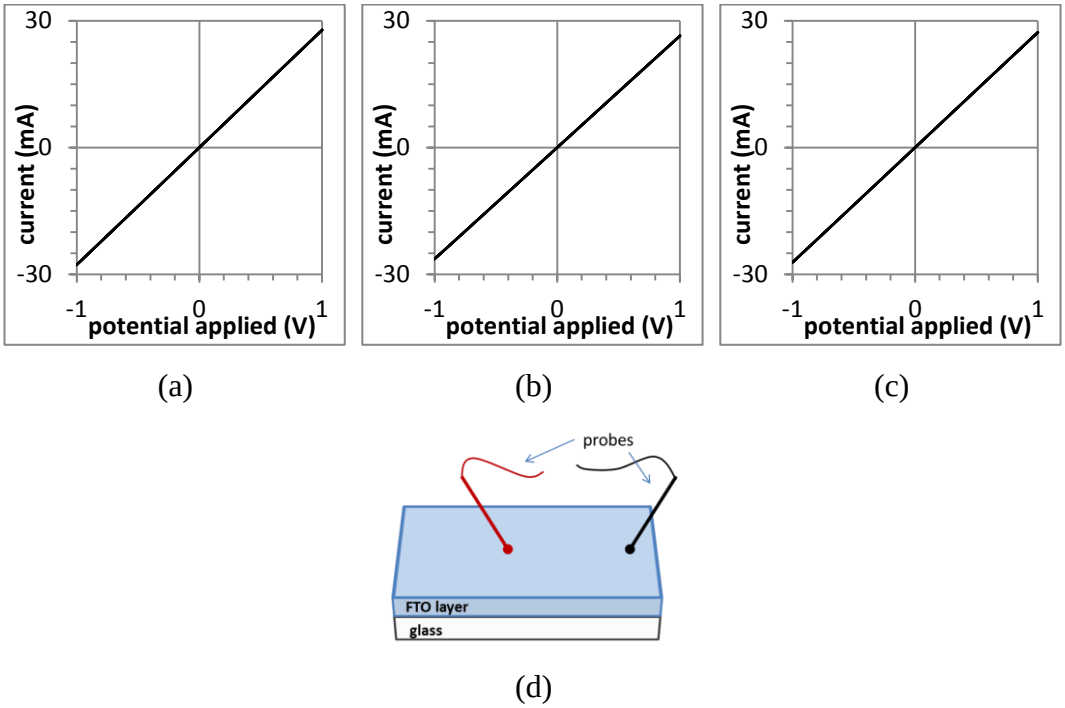

Figure 4.32: Dark I-V characteristics of the bare FTO in three separate measurements (a)-(c); (d) general position of probes on the sample during the measurements. The distance between the probes is fixed and equals 1 cm.

It was observed that both cycles of a measurement as well as each measurement gave nearly identical results as was expected. Both forward and reverse biases are represented by a straight line on the graphs. Absolute values of products of current and voltage for each bias in a graph are identical. Measured current was directly proportional to applied voltage thus the resistance of the FTO is constant and fulfil the Ohm's law so this sample is ohmic. This also results from the ohmic contact obtained between the probes and the FTO layer. All these observations comply with the expectations, therefore, this measurement setup was confirmed to be reliable.

Figure 4.33 shows data of I-V characteristics of the FTO glass substrate that was carbon coated for the sake of SEM imaging. Results from each measurement of this sample are presented in Figure 4.33(a)-(c). Each measurement consisted of two cycles of forward and revers bias. Between each

measurement, the probes were raised and reapplied on the sample. First two measurements were taken with probes applied in the same axial position as shown in Figure 4.33(d). This part of the surface of the sample was largely coated with thin layer of carbon. Third measurement was taken with the probes applied close to the edge of the sample as shown in Figure 4.33(e). This part of the sample was less coated with carbon, which is shown as brighter shading in the figure.

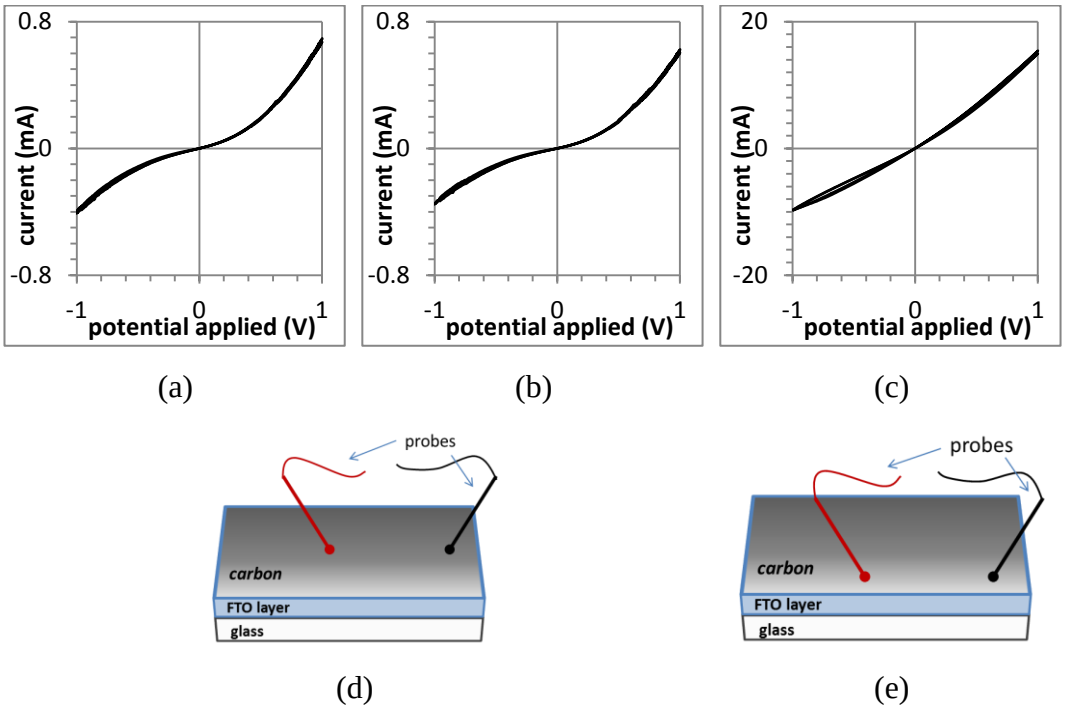

Figure 4.33: Dark I-V characteristics of the carbon-coated (grey area) FTO substrate in three separate measurements (a)-(c); (d) general position of probes on the sample during the measurements a, and b,; (e) general position of probes on the sample during the measurement c. The distance between the probes is fixed and equals 1 cm.

It can be clearly seen that the results obtained for this sample are fundamentally different from those obtained for FTO glass without carbon coating. First difference is non-linear relationship between current and voltage, which occurred in all measurements for carbon-coated FTO glass. Therefore, it does not fulfil the Ohm's law anymore. Supposedly it can be attributed to non-ohmic type of electrical contact between the FTO layer and carbon coating or

between this coating and applied probes as well as it can be the feature of the carbon coating itself. Also range of measured current at applied identical potentials is significantly different. Third important difference is asymmetry between absolute values of products of current and voltage for each bias. Moreover, the results are not repeatable when probes were relocated to different position on the surface of the carbon-coated sample. Therefore, it was concluded that obtained data for all samples with thin films deposited with prospective application as blocking layers in DSSCs are not reliable or verifiable and are not discussed in this study.

Figure 4.34 presents data of current-voltage characteristics of the practise test sample that was not carbon coated. The film on this sample was deposited at 300°C, at deposition duration of 120 minutes, under total pressure of 2 mTorr and oxygen partial pressure of 0.40 mTorr. Results from each measurement of this sample are presented in Figure 4.34(a)-(c). Each measurement consisted of two cycles of forward and reverse bias. The probes were raised and reapplied on the sample between each measurement. First two measurements were performed with probes applied in the same axial position (see Figure 4.34(d)) and third measurement was taken with the off-set of 1 mm from the previous position of the probes.

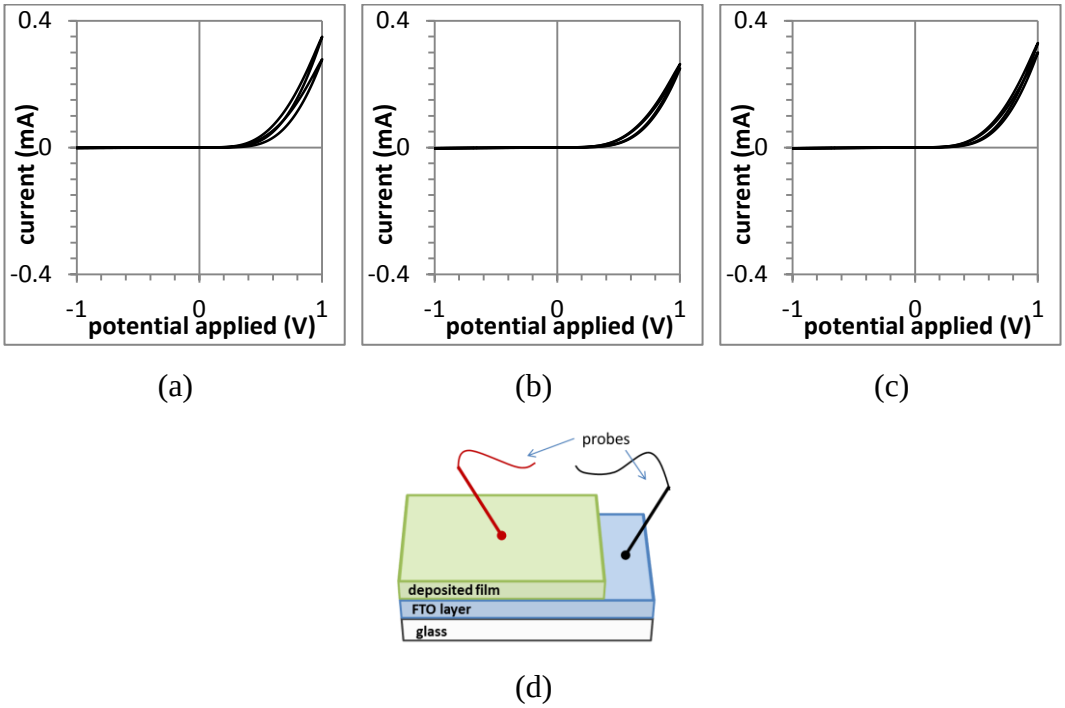

Figure 4.34: Dark I-V characteristics of the sample with thin film deposited under p_{O_2} = 0.40 mTorr, at t_d = 120 min, obtained in three separate measurements a-c); d) general position of probes on the sample during the measurements. The distance between the probes is fixed and equals 1 cm.

The results obtained for the practice test sample are reproducible thus can be considered as reliable. The obtained I-V characteristics are distinctive and differ from that obtained for the bare FTO substrate. These characteristics are nonlinear and similar to diode characteristics. The forward voltage for this type of diode can be estimated to about 0.5 V. The maximum current obtained at applied maximum forward bias voltage of 1 V is about 0.3 mA that is lower by at least one order of magnitude in comparison with the current obtained for the bare FTO sample at the same voltage. The leakage current of such diode is very small and applied reverse biased potential did not reach the breakdown voltage for that diode-like sample. If this behaviour of the sample entirely originates from the created junction between the deposited titanium oxide film and FTO layer, such prepared sample can be beneficial in applications in DSSC where current flow in reverse bias should be

minimized. On the other hand, the amount of current flowing in forward bias for this sample is smaller than in the case of the bare FTO sample at the same applied electrical potential. This suggests that the current flow through this sample in forward bias is partially diminished by the created junction. Application of this type of deposited film on FTO substrate in dye-sensitized solar cells has not been tested in this study. However, oxygen partial pressure used for deposition of this film fall into the range of partial pressures used in this study for preparation of other thin films that were used as BL in DSSCs, therefore, such non-ohmic behaviour of some of these samples can be possible.

Chapter 5: Current-voltage characteristics of fabricated DSSCs with BL under illumination

5.1 Introductions

The purpose of this chapter is to give the description of all characterisation techniques used in this research for characterisation of photovoltaic parameters of fabricated solar cells that include different types of blocking layers. This chapter also shows all the obtained results from the measurements and presents detailed discussion and conclusions on each measured parameter of fabricated solar cells.

5.2 Characterisation methods

The standard characterisation technique of the photovoltaic performance of Dye-Sensitized Solar Cells is based on direct current-voltage characterisation under illumination conditions. The photocurrent-voltage characteristics were obtained by use of a potentiostat (PGSTAT302N, Metrohm Autolab) in combination with a known light source coming from a solar simulator (LCS-100 Solar Simulator, Newport) to perform the photovoltaic performance characterisation of the fabricated DSSCs. The measurement was performed inside a Faraday cage to protect the equipment from external electromagnetic fields that would influence the measurement conditions. All the measurements were carried out with use of computer control software (NOVA). All the measurements were performed on DSSCs listed in Table 5.1.

Table 5.1: List of fabricated DSSCs with BL, which photocurrent-voltage characteristic was tested.

DSSC sample	type of BL	deposition duration (min)	Oxygen partial pressure (mTorr)	Number of cells	active area of the DSSC (cm^2)	total intensity of the incident light for JV characteristics (W/m^2)
C_{ST}	-	-	-	9	0.283	1000
C_{BL}15/0.26	BL15/0.26	15	0.26	3		
C_{BL}120/0.26	BL120/0.26	120		3		
C_{BL}30/0.11	BL30/0.11	30	0.11	3		
C_{BL}30/0.14	BL30/0.14		0.14	3		
C_{BL}30/0.18	BL30/0.18		0.18	3		
C_{BL}30/0.26	BL30/0.26		0.26	3		
C_{BL}30/1.00	BL30/1.00		1.00	3		
C_{BL}30/2.00	BL30/2.00		2.00	3		

The source of radiation in the solar simulator is a xenon lamp, which passes through a set of optics including light filters before it exits the simulator. The spectrum of radiation exiting the solar simulator is, therefore, very similar to the spectrum of the sun incident on the earth surface. This particular spectrum of the sun is standardized to a spectrum known as AM1.5 which represents the overall yearly average spectrum at mid-latitudes. Light intensity for the characterisation of the DSSCs was set to 1000 W/m^2, which corresponds to full sun illumination. The adjustment of the intensity of the incident light intensity was performed by regulating the distance between the light source and a plane of incident light. The plane of incidence was dictated by a plane of a photoactive component of a pyranometer (CM11, Kipp & Zonen) that was positioned on a base under the solar simulator. The pyranometer is commonly used device for measuring solar irradiance on a planar surface. To measure the solar radiant flux density of the solar simulator, the pyranometer was placed on a levelled surface

directly under the incident light, perpendicularly to the light beam. The entire solar simulator was attached to a vertically moving stage that facilitates change of light intensity in relation to plane of incidence by moving the solar simulator further or closer to the illuminated plane. Therefore, this feature was used to adjust the light intensity by setting the appropriated distance between the solar simulator and the pyranometer. Setup for calibration the light intensity from the solar simulator is shown in Figure 5.1.

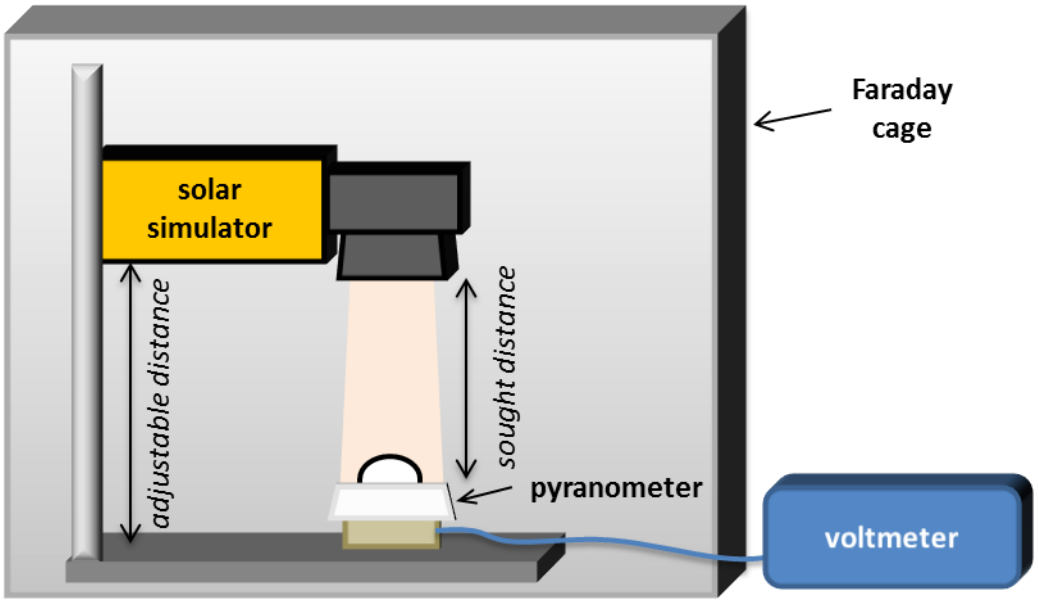

Figure 5.1: Setup for calibration light intensity to 1000 W/m^2.

During the photocurrent-voltage characterisation of the DSSCs, the samples were placed perpendicularly under the incident light, on a laboratory jack, which height was adjusted to the level of photoactive component of pyranometer that after calibration of the position of the solar simulator received full sun illumination. The samples were measured individually and were facing their working electrodes towards the light source thus were characterised with conventional front illumination. The working electrode and counter electrode from the measured cell were connected to the potetiostat. The setup for photocurrent-voltage characterisation is shown in Figure 5.2.

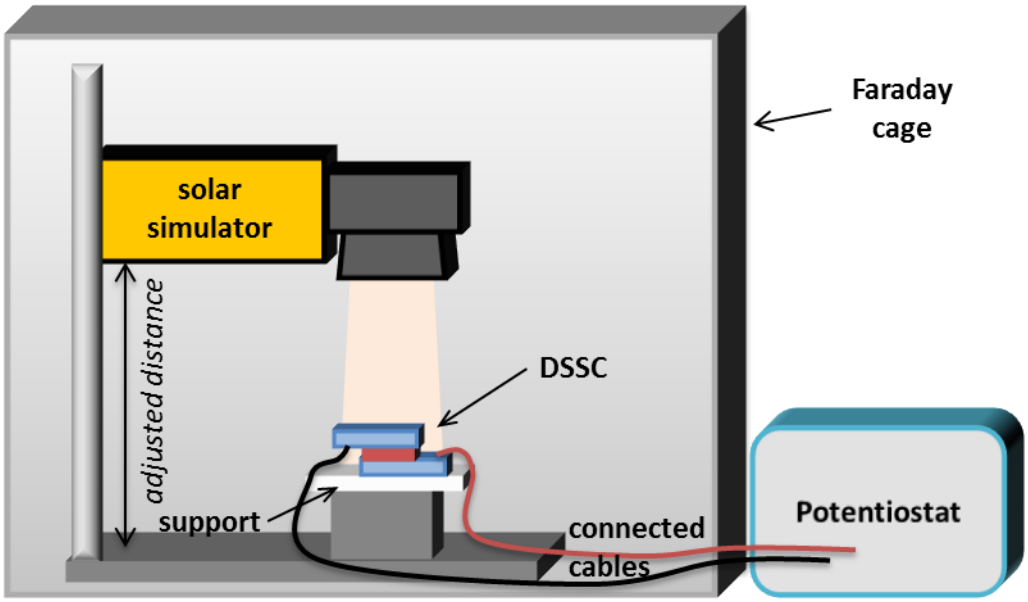

Figure 5.2: Setup for photocurrent-voltage characterisation of the DSSCs.

The current-voltage measurements were obtained by applying a potential scan, from short-circuit conditions to the open-circuit potential, under constant illumination. Each sample was measured in one process consisting of three cycles, and each cycle consisted of potential increasing and decreasing. The obtained results from the measurement are usually presented as IV curves that are plot as measured photocurrent as a function of applied voltage. Considering an active area of the cell equal to 0.283 cm^2, the measured photocurrent was divided by this value and expressed as photocurrent density. All photocurrents presented in this work are averaged values of the second cycle calculated as the mean value of current between increasing and decreasing potential at each applied potential. The samples were measured under forward bias conditions. The measurements were taken with step potential of 2 mV and at the scan rate of 20 mV/s. The photocurrent density-voltage curves allow obtaining the following basic parameters of the solar cell:

- the maximum current density that was obtained at an applied potential of 0 V and is called the short-circuit current density, J_{SC}.

- the maximum applied voltage at which the obtained current density is equal to 0 A/cm^2 and is called the open-circuit voltage, V_{OC}.
- the point on the JV curve where the maximum power density is generated and is called the maximum power point, P_{max}.
- the ratio of the maximum power density to the product of the values of the short-circuit current density and open-circuit voltage and is called the fill factor, FF. This relation is given by

$$FF = \frac{P_{max}}{J_{SC} \cdot V_{OC}} \qquad \text{(equation 5.1)}$$

- the ratio of the developed power density under illumination to the total intensity of the incident light, P_{in}, and it is known as the efficiency, η. This relation is given by

$$\eta = \frac{P_{max}}{P_{in}} \qquad \text{(equation 5.2)}$$

5.3 Influence of BLs deposition duration on performance of DSSCs

5.3.1 Characterisation of best performing cells

Figure 5.3 shows photocurrent-voltage characteristics of fabricated standard-type DSSC without blocking layer, named as C_{ST}, and fabricated DSSCs that incorporate deposited titanium oxide thin films as blocking layers, which names begin with C_{BL}. The cells with the blocking layers are those where titanium oxide BLs were deposited under identical oxygen partial pressure of 0.26 mTorr and at different deposition duration between 15 minutes and 120 minutes. Shown characteristics of the cells represent only one best-performing cell, based on its efficiency η, which belongs to a set of identically prepared cells. The photocurrent-voltage characteristics were obtained under illumination conditions of simulated sunlight of AM1.5 spectrum with total irradiance of 100 mW/cm^2. Size of an active area of each cell was constant and equal to 0.283 cm^2.

Photovoltaic parameters of each presented cell that were calculated based on their photocurrent-voltage characteristics are detailed in Table 5.2.

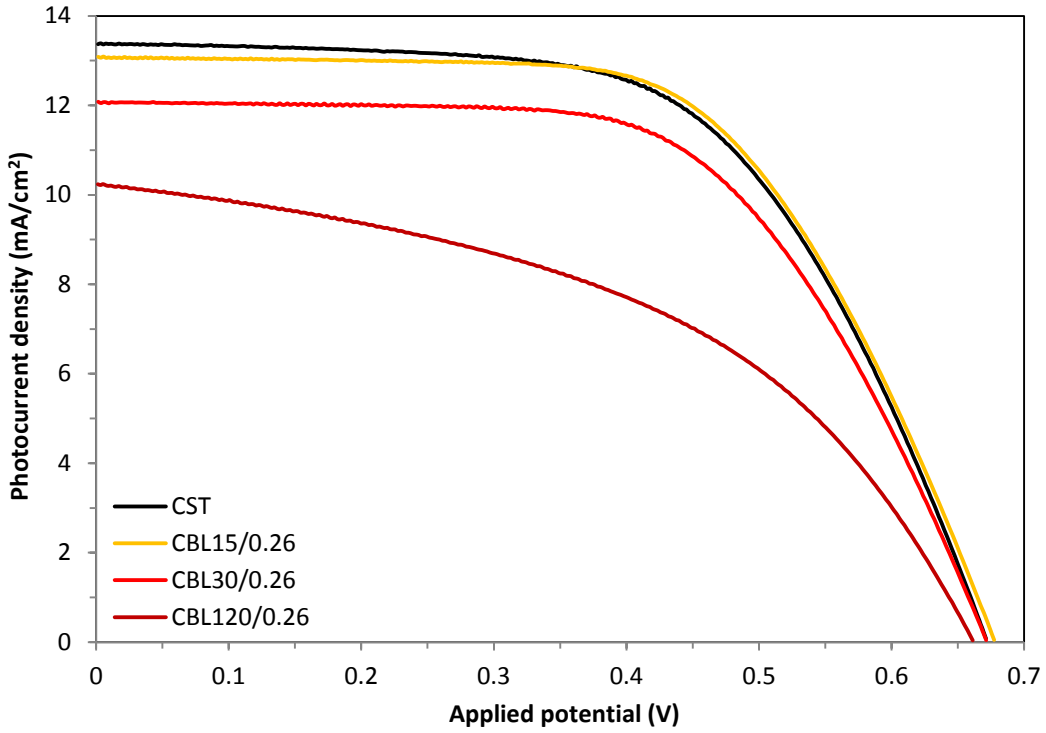

Figure 5.3: Photocurrent density-voltage characteristics of best-performing DSSCs without and with BLs deposited under the oxygen partial pressure of 0.26 mTorr. The measurement was taken under AM1.5 simulated-sunlight illumination (100 mW/cm^2). Initial temperature for each measurement was 25^{o}C.

Table 5.2: Photovoltaic parameters of best-performing DSSCs without and with BLs deposited under the oxygen partial pressure of 0.26 mTorr. The measurement was taken under illumination of AM1.5 simulated solar light (100 mW/cm^2).

sample	deposition duration (min)	Oxygen partial pressure (mTorr)	cell efficiency, η (%)	cell short-circuit current density, J_{SC} (mA/cm^2)	cell open-circuit voltage, V_{OC} (mV)	cell Fill Factor, FF
C_{ST}	-	-	5.32	13.37	671	0.59
C_{BL}15/0.26	15	0.26	5.41	13.08	677	0.61
C_{BL}30/0.26	30		4.90	12.08	671	0.60
C_{BL}120/0.26	120		3.16	10.24	661	0.47

From the presented photocurrent-voltage characteristics it can be seen that the cells performed differently depending on what type of blocking layer was incorporated in their structure. Generally, the cell C_{BL}15/0.26, which is the best of all 3 cells prepared with the thinnest blocking layer, performed very similarly to the cell C_{ST}, which was the best of all 9 prepared standard-type DSSCs. The current-voltage curves of these two are very close to each other thus most of their photovoltaic parameters were expected to be similar, which was confirmed after calculations. The best cell with BL of the same composition and structure, but with typical thickness in this study, of about 53 nm, presents similar shape of the curve to those previous cells, which indicates that their series resistances and shunt resistances are comparable between these cells. However, the photocurrent obtained from the cell C_{BL}30/0.26 is lower to some extent. The best cell of those fabricated with the thickest blocking layer of the same composition performed significantly differently than the other cells discussed in this section. Its current-voltage curve explicitly shows that both parasitic resistances, the series resistance and the shunt resistance, differ from the resistances in other cells. The series resistance is distinctly higher, which can be directly related with observed high resistance of this type of thin film as used in this cell as the blocking layer.

The shunt resistance is notably lower that indicates increase of a leakage current in the cell. This may result from increased electron recombination processes occurring in the cell, however this cannot be confirmed based on the results obtained in this study. Both changes in these resistances are unfavourable in terms of high performance of the DSSC.

Figure 5.4 presents efficiencies of fabricated standard-type DSSC without blocking layer and fabricated DSSCs incorporating deposited titanium oxide thin films as blocking layers. The blocking layers were deposited under oxygen partial pressure of 0.26 mTorr and at different deposition durations. The values of efficiencies are presented as a function of deposition duration of the BL that was included in the solar cell structure. The efficiencies were calculated based on the photocurrent-voltage characteristics of best-performing DSSCs that were obtained under simulated full sunlight illumination conditions. Each efficiency value was computed from the second cycle of the three-cycle current-voltage characterisation. The exact values of the efficiencies can be found in Table 5.2.

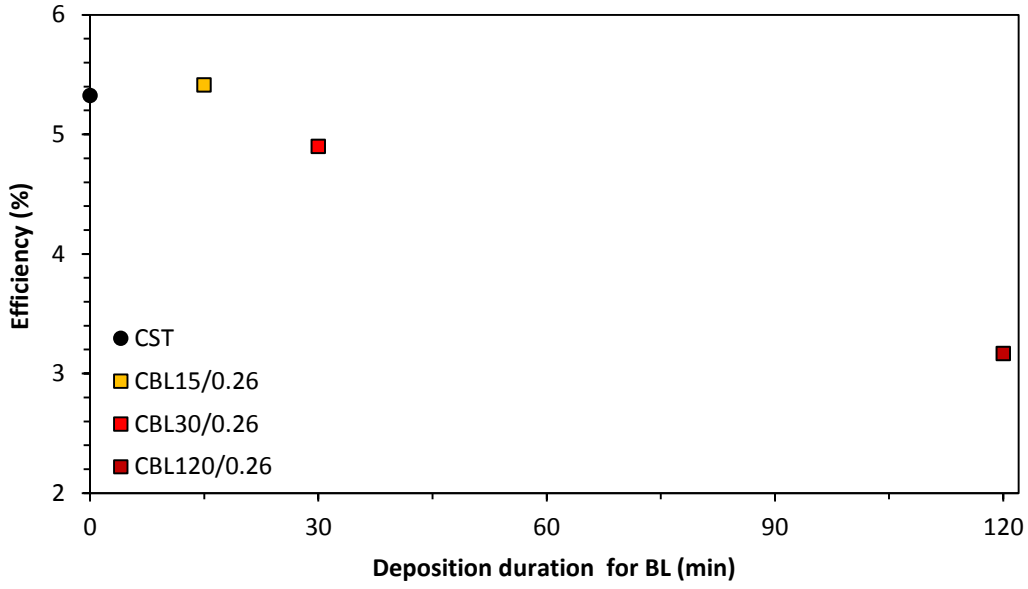

Figure 5.4: Efficiencies of illuminated best-performing DSSCs without and with BLs deposited under the oxygen partial pressure of 0.26 mTorr against the deposition duration of these BLs.

Comparison of calculated efficiencies of these cells shows that the highest conversion efficiency was obtained by the cell with the thinnest blocking layer. Although this efficiency is higher by only small amount than the efficiency of standard DSSC, it should be considered that the visible light transmittance value of the working electrode including this thin blocking layer was decreased by over 12% (see chapter 4.3) compared to the transmittance of the working electrode without PLD-coating used for standard-type DSSC. Therefore, the amount of possible photogenerated current in the cell with this blocking layer and resulting conversion efficiency was already decreased at the beginning. Comparison of the cells in terms of the deposition duration for the blocking layer, which impinges upon the thickness of the blocking layer, shows the decreasing trend of cell performance. The thicker the deposited blocking layer the lower is the efficiency of the cell. Except the observed increase of light attenuation of the blocking layer, also increased electrical resistance (see section 4.5) occurring along with the increment of the thickness could adversely influence the overall performance of the fabricated cells.

Figure 5.5 shows short-circuit current densities of the fabricated standard DSSC without blocking layer and DSSCs incorporating deposited thin film blocking layers of titanium oxide. These blocking layers were deposited under the oxygen partial pressure of 0.26 mTorr and with different deposition durations. The values of short-circuit current densities are presented as a function of deposition duration of the BL that was incorporated in the solar cell structure. The short-circuit current densities were calculated based on the current-voltage characteristics of best-performing DSSCs, which were obtained under-simulated sunlight conditions. Each value of the short-circuit current density was calculated from the second cycle of the current-voltage characterisation performed in three cycles. The exact values of the short-circuit current densities can be found in Table 5.2.

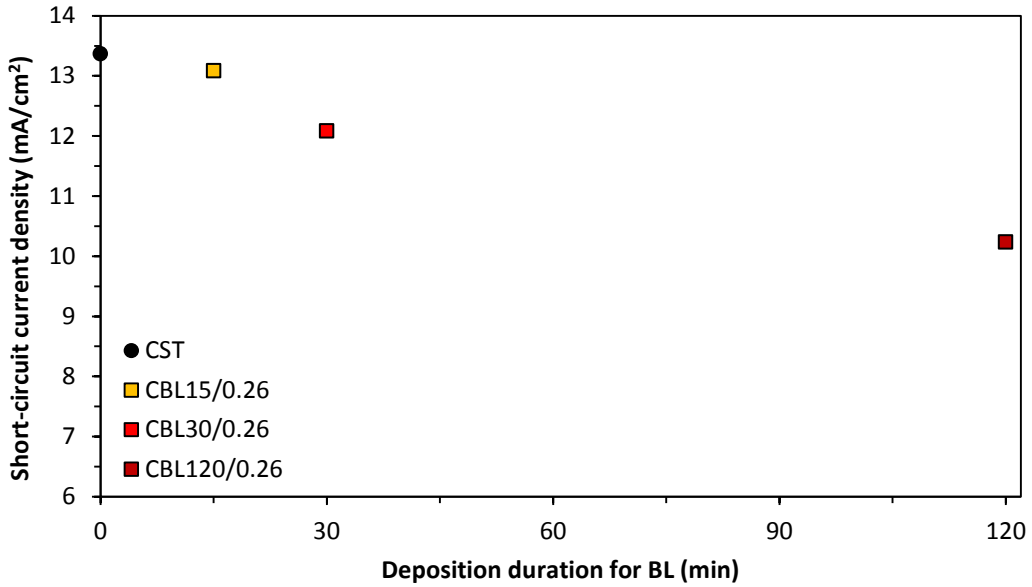

Figure 5.5: Short-circuit current densities of illuminated best-performing DSSCs without and with BLs deposited under the oxygen partial pressure of 0.26 mTorr against the deposition duration of these BLs.

Observed decrease of the short-circuit current densities for these cells along with increase of the thickness of the blocking layer complies with the relation between the light transmittance and deposition duration of the blocking layer. This proves the possible effect of the thickness of BL on the concentration of photogenerated carriers inside the fabricated DSSCs due to change of the number of incident photons that permeate into the cell. However, the short-circuit current depends not only on number of incident photons that reach the photoactive part of the solar cell but also on other factors, like charge collection probability that is related with minority carrier lifetime in the cell. The data from the current-voltage characteristics of the cells show that the short-circuit current density obtained from the cell with the thinnest PLD-deposited blocking layer is similar to that obtained from the standard cell without blocking layer. Therefore it can be assumed that although the concentration of photogenerated electrons in the cell $C_{BL}15/0.26$ was diminished, the amount of collected electrons at the contacts of this cell was comparably higher. This possible increase in charge collection

efficiency can be attributed to increase of the minority carrier lifetime, where minority carrier is the electron. This is possible when, for instance, the photoelectrons recombination at the interface of transparent conductive oxide / electrolyte in DSSC is suppressed. As the blocking layer was incorporated into these cells at that interface, the supposed blocking effect of this recombination process was probably achieved to some extent with the blocking layer with thickness of about 30 nm that was PLD-deposited under oxygen partial pressure of 0.26 mTorr.

Open-circuit voltages of the fabricated standard DSSC without blocking layer and DSSCs that include deposited blocking layers of titanium oxide thin films are presented in Figure 5.6. These PLD-deposited blocking layers were obtained under the oxygen partial pressure of 0.26 mTorr and at different deposition durations. The values of open-circuit voltages are presented as a function of deposition duration of the BL which was included in the structure of the solar cell. Values of the open-circuit voltages were obtained from the current-voltage characteristics of best-performing DSSCs which were characterised under conditions of simulated full sunlight. The obtained values of the open-circuit voltages were retrieved from the second cycle of the current-voltage characteristics performed in three cycles. The exact values of the open-circuit voltages are included in Table 5.2.

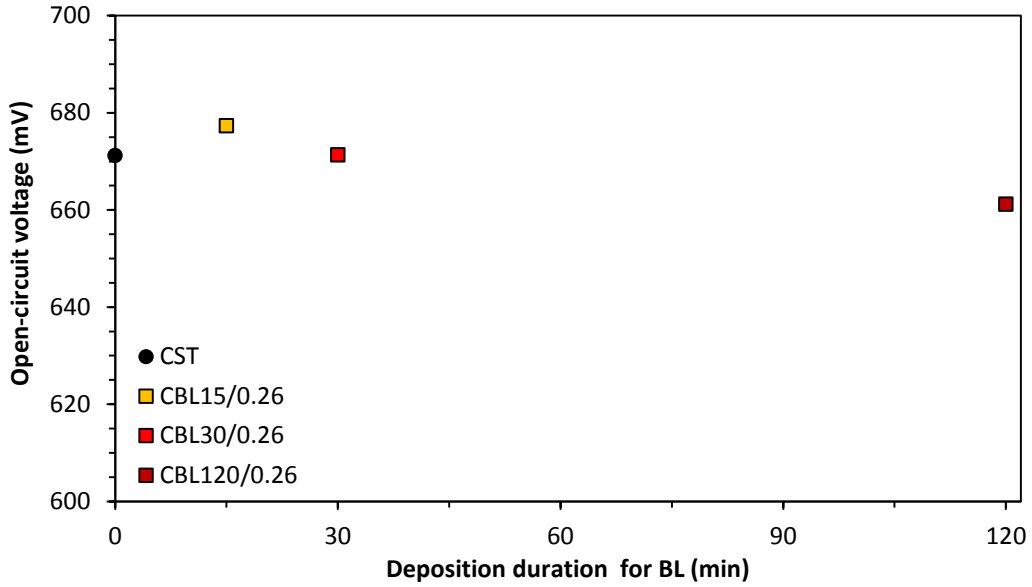

Figure 5.6: Open-circuit voltages of illuminated best-performing DSSCs without and with BLs deposited under the oxygen partial pressure of 0.26 mTorr against the deposition duration of these BLs.

The relation between the open circuit voltage and the thickness of the blocking layer, derived from the deposition duration, shows a certain increase of the voltage, when the thinnest BL was included in the cell structure, and is followed by steady decrease with increase of the thickness. The open-circuit voltage depends to some extend on light generated current that as mentioned before was adversely affected by thickness-related transmittance of the front side component of the DSSC. Therefore, the decrease in the open-sircuit voltage can be attributed to this effect as well. On the other hand, the cell $C_{BL}15/0.26$ and $C_{BL}30/0.26$ obtained higher and equal voltage, respectively, to the voltage of the cell C_{ST}. This is possible to explain by the fact that another factor that has influence on the open-circuit voltage is saturation current, which is dependent on recombination processes in the cell. For this reason the value of V_{OC} is sometimes used as a measure of the amount of recombination processes in the solar cell. Therefore, comparing the values of the open-circuit voltages obtained for these

two cells against the standard cell, it can be assumed that a certain amount of recombination process was reduced.

Fill factors of the prepared standard DSSC without blocking layer and cells with PLD-deposited blocking layers of titanium oxide are presented in Figure 5.7. The blocking layers were deposited under the oxygen partial pressure of 0.26 mTorr and with different deposition durations. The fill factors values are presented as a function of the deposition duration relevant to the BL which was incorporated into the structure of the DSSC. The values of the fill factors were computed from the current-voltage characteristics of best-performing DSSCs that were characterised under conditions of simulated full sunlight. The computation of the values of the fill factors was based on the second cycle of the three-cycle current-voltage characteristics. The exact fill factors values are included in Table 5.2.

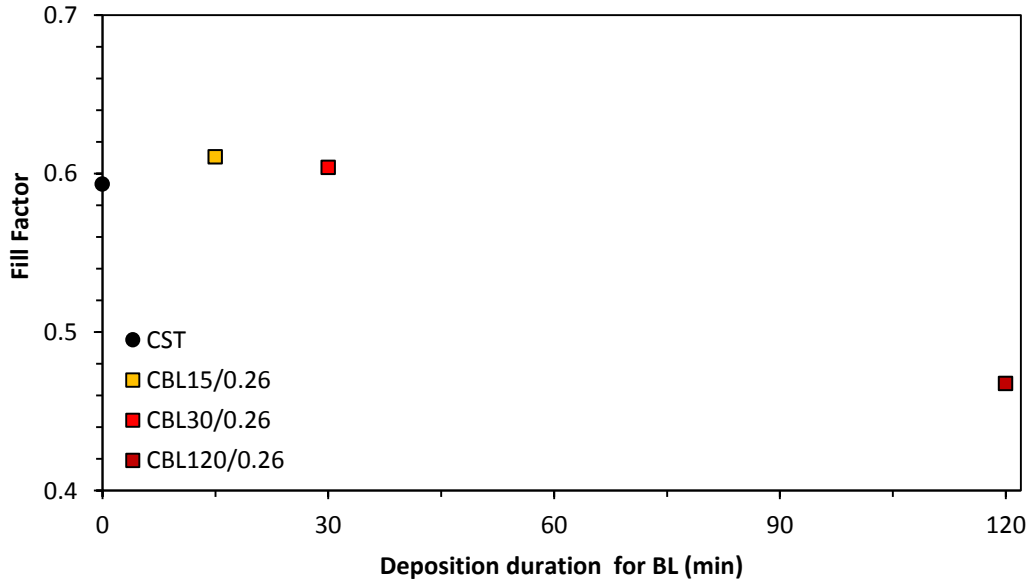

Figure 5.7: Fill factors of illuminated best-performing DSSCs without and with BLs deposited under the oxygen partial pressure of 0.26 mTorr against the deposition duration of these BLs.

The fill factor is dependent on the ideality factor and the latter is the measure of type of recombination in the solar cell. The fill factor can be impaired when undesired recombination reactions take place in the DSSC. As this is one of the main drawbacks in DSSC, the obtained fill factor value of 0.59 for standard-type DSSC, which is law and far from that of an ideal solar cell, was expected for this type of solar cells. The increase of fill factor to 0.61 and 0.60 for the cells with BLs of about 30 nm and 53 nm is another indicator that unwanted recombination reactions occurring in the cell have been reduced to some extent by incorporation of these two blocking layers. On the other hand, the cell with the thickest blocking layer of about 149 nm features significantly low obtained fill factor. This can be combination of two features of this PLD-deposited blocking layer. First is related with the fact that PLD-deposited films are usually compact and pin-hole free, which was also proven from cross-sectional images of deposited films. Therefore, if such layer consists of resistive material, it can effectively affect the current flow through it. Second feature is the thickness of this titanium oxide film in that cell, which is relatively thick. Therefore, all the electrical properties related with the thickness of this film were enhanced which was observed from electrical resistance measurements of this film. Therefore, increased electrical resistance contributed to the increase of series resistance of the cell, which was observed on the current-voltage curve, and consequently diminished the fill factor of that cell.

5.3.2 Characterisation of sets of fabricated cells

Figure 5.8 shows averaged efficiencies of sets of fabricated DSSCs. The averaged efficiencies are calculated for the set of standard-type DSSCs fabricated without blocking layer, called C_{ST}, and for the sets of DSSCs fabricated with different deposited titanium oxide thin films as blocking layers, which names begin with C_{BL}. The blocking layers were deposited under the oxygen partial pressure of 0.26 mTorr and with different deposition durations. The averaged values of efficiencies

are presented as a function of deposition duration relevant to the type of the BL which was incorporated into the structure of the set of DSSCs. The efficiencies average values were calculated from the cells efficiencies based on the photocurrent-voltage characteristics of the sets of DSSCs that were characterised under simulated full sunlight conditions. Each averaged value of the efficiency was computed from the efficiency of the second cycle of the current-voltage characteristics and is presented along with an error bar representing a standard error of the mean. The exact averaged values of the efficiencies can be found in Table 5.3 along with errors of estimation and BLs deposition conditions.

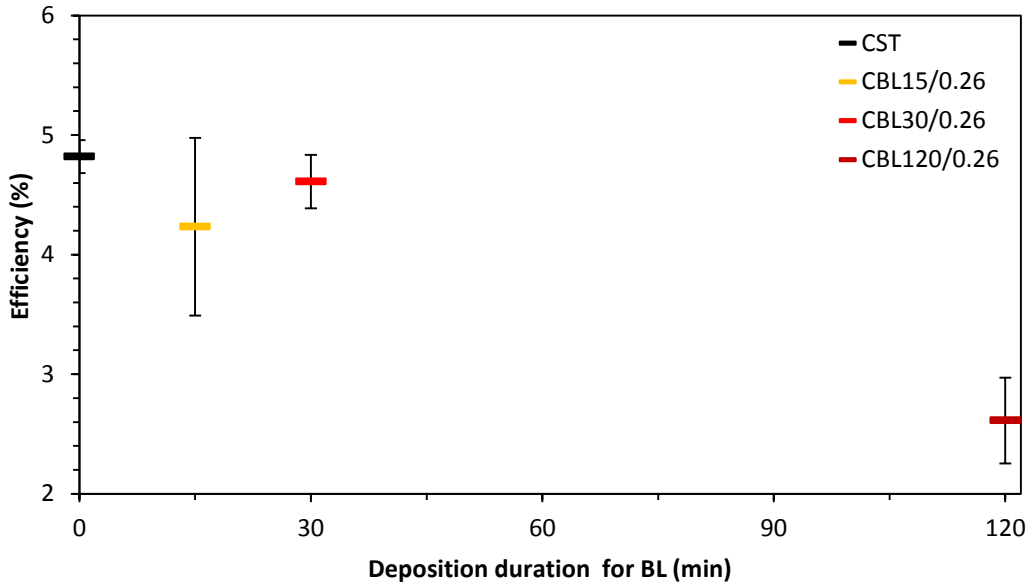

Figure 5.8: Averaged efficiencies of illuminated sets of DSSCs without and with BLs deposited under the oxygen partial pressure of 0.26 mTorr against the deposition duration of these BLs.

Table 5.3: Averaged efficiencies of illuminated sets of DSSCs without and with BLs deposited under the oxygen partial pressure of 0.26 mTorr including errors of estimation and deposition conditions.

sample	deposition duration (min)	Oxygen partial pressure (mTorr)	cell efficiency - averaged, η (%)	standard deviation (%)	standard error (%)
C_{ST}	-	-	4.82	0.41	0.14
C_{BL}15/0.26	15	0.26	4.23	1.29	0.74
C_{BL}30/0.26	30		4.61	0.39	0.22
C_{BL}120/0.26	120		2.61	0.62	0.36

The averaged efficiencies of the characterised cells show that none of the cells with blocking layer performed better than the standard cells. Moreover, on average, cells with the medium-thick blocking layer performed better than the cells with the thinnest BL. Therefore the trend observed based on the sets of samples does not comply with the trend observed for the best performing cells only. However, the calculated errors of estimations of the mean values suggest that within the set of the cells named as C_{BL}15/0.26 it is possible to obtain a cell that performs better than the standard type cell, but statistically possibility of obtaining such cell is low. That diversity of the results is related with the complexity of the manufacturing process of the DSSC and fact, that one of the crucial steps in obtaining small divergence of the performance of DSSCs is application of mesoporous TiO_2 layer on working electrode. Although using the scree-printing technique for that process to increase the similarity of thickness and uniformity of the layer quality, obtaining repeatable and reproducible results was one of the challenges in this research.

Figure 5.9 presents averaged short-circuit current densities of sets of fabricated DSSCs. The averaged short-circuit current densities are calculated for the set of standard-type DSSCs without blocking layer and for the sets of different

DSSCs incorporating deposited titanium oxide thin films as blocking layers. The blocking layers were deposited under the oxygen partial pressure of 0.26 mTorr and at different deposition durations. The averaged values of short-circuit current densities are presented as a function of deposition duration relevant to the type of the BL included in the structure of the set of DSSCs. The average values of short-circuit current densities were calculated from the cells short-circuit current densities based on the photocurrent-voltage characteristics of the sets of DSSCs that were tested under simulated full sunlight conditions. Each averaged value of the short-circuit current density was computed from the short-circuit current densities of the second cycle of the current-voltage characteristics and is presented along with the error bar representing the standard error of the mean. The exact averaged values of the short-circuit current densities can be found in Table 5.4 along with the errors of estimation and BLs deposition conditions.

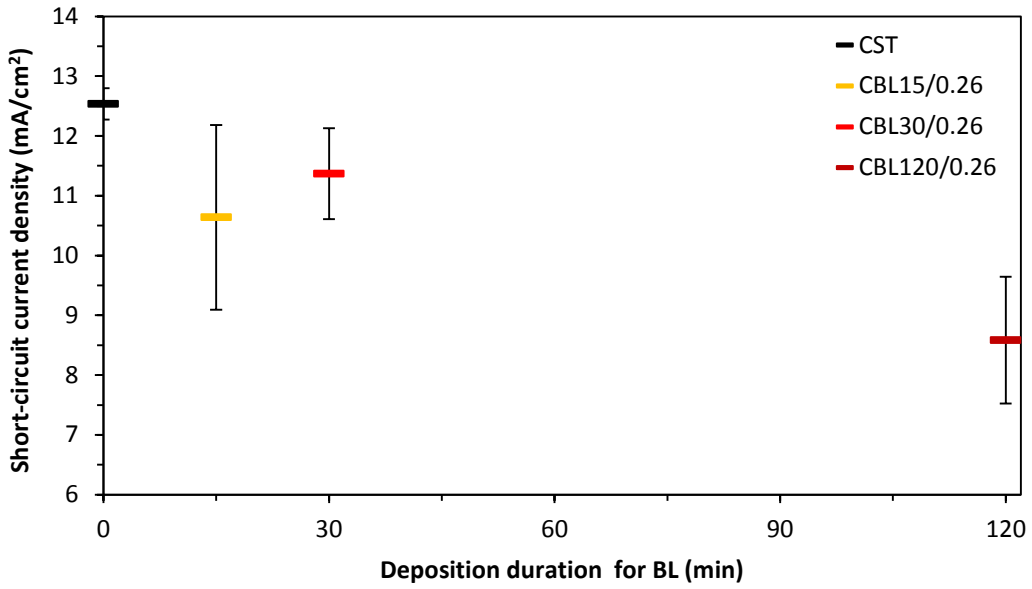

Figure 5.9: Averaged short-circuit current densities of illuminated sets of DSSCs without and with BLs deposited under the oxygen partial pressure of 0.26 mTorr against the deposition duration of these BLs.

Table 5.4: Averaged short-circuit current densities of illuminated sets of DSSCs without and with BLs deposited under the oxygen partial pressure of 0.26 mTorr including errors of estimation and deposition conditions.

sample	deposition duration (min)	Oxygen partial pressure (mTorr)	cell short-circuit current density - averaged, J_{SC} (mA/cm^2)	standard deviation (mA/cm^2)	standard error (mA/cm^2)
C_{ST}	-	-	12.53	0.79	0.26
C_{BL}15/0.26	15	0.26	10.64	2.67	1.54
C_{BL}30/0.26	30		11.37	1.31	0.76
C_{BL}120/0.26	120		8.58	1.83	1.06

As the value of short-circuit current obtained from the cell during illumination has strong influence on generated power by the cell, presented results of the averaged short-circuit current densities follow similar trend as presented averaged values of the efficiency. On average, the highest short-circuit current density, equal to 11.37 mA/cm^2, among the cells prepared with blocking layer was obtained for the cells with medium thick blocking layer. The standard error of the mean value of short-circuit current densities for cells with the thinnest blocking layer was relatively large and this was the effect of one of the three prepared cells with that blocking layer. This cell presented poor performance obtaining value of short-circuit current density equal to only 7.78 mA/cm^2. As a result, its calculated conversion efficiency was only 2.86%. Possible reason for this is unrepresentative thickness of screen-printed porous TiO_2 layer. Under the circumstances, such fabricated working electrode will have lower surface area thus leaving less space for dye adsorption during sensitization process. Consequently such cell with significantly less amount of adsorbed dye molecules, produces less amount of photogenerated carriers, which results in general in lower values of current

obtained from the cell. However, no experiment was conducted in this research to confirm the reason of lower performance of this cell.

Figure 5.10 shows averaged open-circuit voltages of the sets of prepared DSSCs. The averaged open-circuit voltages are calculated for the set of standard DSSCs without blocking layer and for the sets of DSSCs including various deposited titanium oxide films as blocking layers. The blocking layers were deposited under the oxygen partial pressure of 0.26 mTorr and at various deposition durations. The averaged values of the open-circuit voltages are presented as a function of deposition duration relevant to the type of the BL incorporated into the structure of the set of DSSCs. The average values of open-circuit voltages were calculated from the open-circuit voltages of the cells of the sets of DSSCs retrieved from their photocurrent-voltage characteristics that were performed under simulated full sunlight conditions. Each averaged value of the open-circuit voltage was calculated from the open-circuit voltages of the second cycle of the current-voltage characteristics and is presented along with the error bar representing the standard error of the mean. The exact averaged values of the open-circuit voltages can be found in Table 5.5 along with the errors of estimation and BLs deposition conditions.

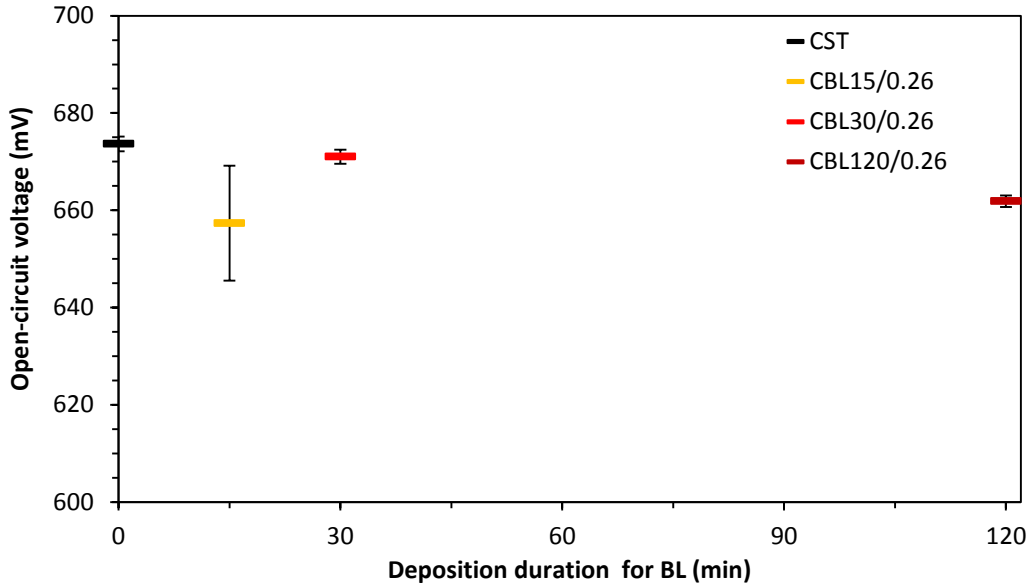

Figure 5.10: Averaged open-circuit voltages of illuminated sets of DSSCs without and with BLs deposited under the oxygen partial pressure of 0.26 mTorr against the deposition duration of these BLs.

Table 5.5: Averaged open-circuit voltages of illuminated sets of DSSCs without and with BLs deposited under the oxygen partial pressure of 0.26 mTorr including errors of estimation and deposition conditions.

sample	deposition duration (min)	Oxygen partial pressure (mTorr)	cell open-circuit voltage - averaged, V_{OC} (mV)	standard deviation (mV)	standard error (mV)
C_{ST}	-	-	673.7	4.6	1.5
C_{BL}15/0.26	15	0.26	657.4	20.5	11.8
C_{BL}30/0.26	30		671.0	2.5	1.4
C_{BL}120/0.26	120		661.9	2.1	1.2

The calculated averaged values of open-circuit voltages of these cells have relatively small errors of estimation except the set of cells with the thinnest

blocking layer. The trend observed for this set of data suggests that the optimum thickness for highest open circuit voltage is around 53 nm.

Averaged fill factors of the sets of prepared DSSCs are shown in Figure 5.11. The averaged fill factors are calculated for the set of standard-type DSSCs without blocking layer and for the sets of DSSCs that includes different PLD-deposited titanium oxide blocking layers. The blocking layers were deposited under the oxygen partial pressure of 0.26 mTorr and with different deposition durations. The averaged values of the fill factors are presented as a function of deposition duration relevant to the type of the BL included in the structure of the set of DSSCs. The average values of fill factors were computed from the fill factors of the cells of the sets of DSSCs calculated from their current-voltage characteristics that were performed under simulated sunlight conditions. Each averaged value of the fill factor was calculated from the fill factors of the second cycle of the current-voltage characteristics and is presented along with the error bar representing the standard error of the mean. The exact averaged values of the fill factors are presented in Table 5.6 along with the errors of estimation and BLs deposition conditions.

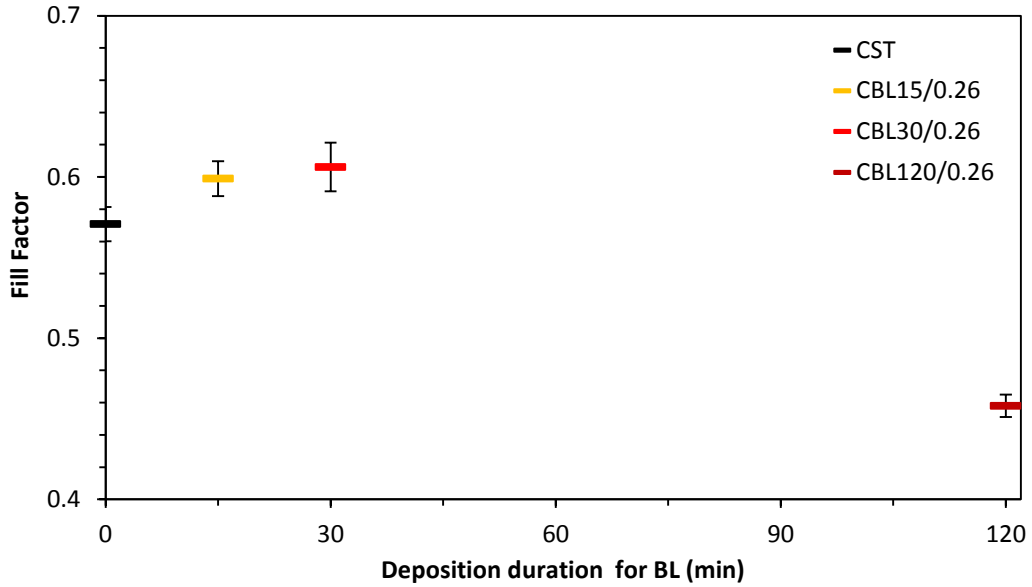

Figure 5.11: Averaged fill factors of illuminated sets of DSSCs without and with BLs deposited under the oxygen partial pressure of 0.26 mTorr against the deposition duration of these BLs.

Table 5.6: Averaged fill factors of illuminated sets of DSSCs without and with BLs deposited under the oxygen partial pressure of 0.26 mTorr including errors of estimation and deposition conditions.

sample	deposition duration (min)	Oxygen partial pressure (mTorr)	cell Fill Factor - averaged, FF	standard deviation	standard error
C_{ST}	-	-	0.57	0.03	0.01
C_{BL}15/0.26	15	0.26	0.60	0.02	0.01
C_{BL}30/0.26	30		0.61	0.03	0.02
C_{BL}120/0.26	120		0.46	0.01	0.01

The averaged fill factor values clearly show the difference between two sets of cells including blocking layer and the set of standard sets without it. On average, cells with the thinnest blocking layer of obtained under the oxygen partial pressure of 0.26 mTorr, have higher fill factor by about 5.2% than those

without the BL. Moreover, cells with blocking layer of the same composition and of typical thickness of about 53 nm shows even higher fill factor by about further 1.7%. Calculated standard error of the mean for fill factor is relatively low, therefore, obtained averaged values of this photovoltaic parameter are good indicators of influence of blocking layer on performance of DSSCs. Observed poor performance of the sample wit thickest deposited blocking layer on current-voltage characteristics of best-performing cells is confirmed in the average value of FF equal to 0.46.

From analysed photovoltaic parameters of deposited cells under identical oxygen partial pressure and with different deposition durations it can be concluded that generally DSSCs with this type of blocking layer are able to perform better to some extent than those without BL even if some of their physical parameters, like for instance light transmittance, are in contradiction with the objectives. Some of these contradictions are related with the thickness of the blocking layer. In order to not adversely affect the performance of the DSSC, the thickness of this type of blocking layer as discussed in this section should be significantly lower than 150 nm. In order to enhance the performance of the DSSC by this type of blocking layer, its preferable thickness is between 30 nm and 50 nm. Possibly, lower thicknesses can also be beneficial.

5.4 Influence of oxygen partial pressure during BLs deposition on performance of DSSCs

5.4.1 Characterisation of best performing cells

Figure 5.12 presents photocurrent-voltage characteristics of prepared standard-type DSSC without blocking layer, called C_{ST}, and fabricated DSSCs that include deposited titanium oxide thin films as blocking layers, which names begin with C_{BL}. The cells with blocking layers are those which titanium oxide BLs were deposited at identical deposition duration equal to 30 minutes and under different

oxygen partial pressure between 0.11 mTorr and 2.00 mTorr. Presented characteristics of the cells represent only one best-performing cell, based on its efficiency η, which belongs to a set of identically fabricated cells. The photocurrent-voltage characteristics were obtained under illumination conditions of simulated sunlight of AM1.5 spectrum with total irradiance of 100 mW/cm^2. Size of an active area of each cell was identical and equal to 0.283 cm^2. Photovoltaic parameters of each presented cell that were calculated based on their photocurrent-voltage characteristics are detailed in Table 5.7.

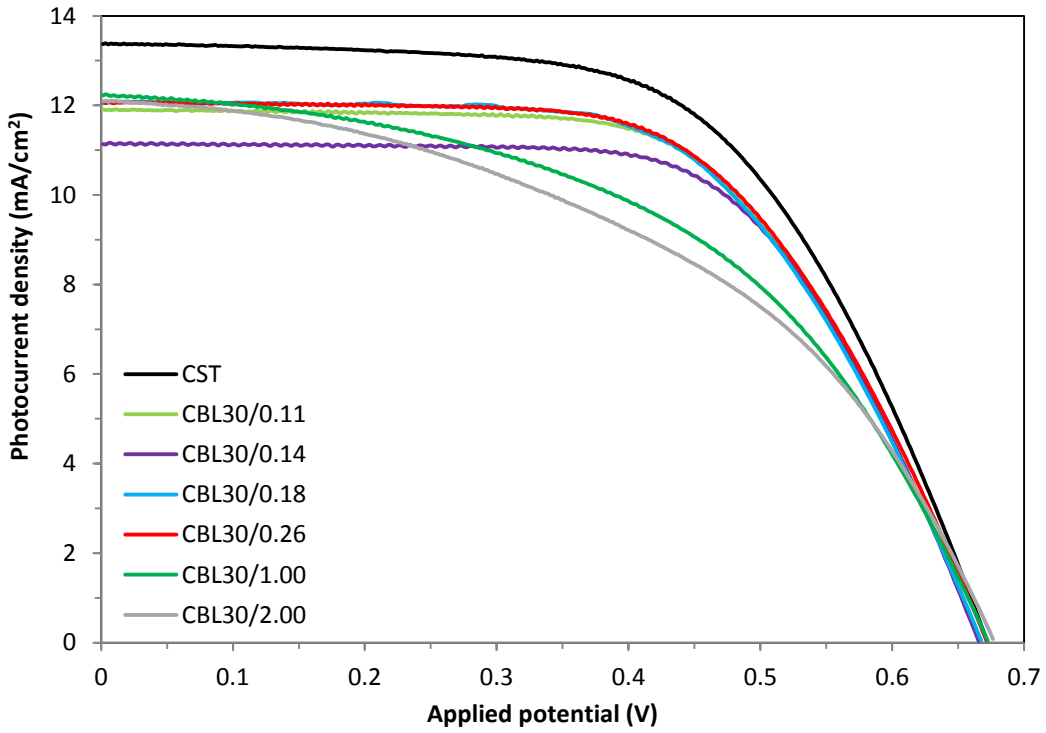

Figure 5.12: Photocurrent density-voltage characteristics of best-performing DSSCs without and with BLs deposited at deposition duration of 30 minutes. The measurement was taken under AM1.5 simulated-sunlight illumination (100 mW/cm^2). Initial temperature for each measurement was 25^{o}C.

Table 5.7: Photovoltaic parameters of best-performing DSSCs without and with BLs deposited at deposition duration of 30 minutes. The measurement was taken under illumination of AM1.5 simulated solar light (100 mW/cm^2).

sample	deposition duration (min)	Oxygen partial pressure (mTorr)	cell efficiency, η (%)	cell short-circuit current density, J_{SC} (mA/cm^2)	cell open-circuit voltage, V_{OC} (mV)	cell Fill Factor, FF
C_{ST}	-	-	5.32	13.37	671	0.59
C_{BL}30/0.11	30	0.11	4.88	11.91	666	0.62
C_{BL}30/0.14		0.14	4.74	11.14	665	0.64
C_{BL}30/0.18		0.18	4.86	12.05	667	0.60
C_{BL}30/0.26		0.26	4.90	12.08	671	0.60
C_{BL}30/1.00		1.00	4.09	12.22	672	0.50
C_{BL}30/2.00		2.00	3.81	12.09	676	0.47

Presented photocurrent-voltage characteristics of this group of cells reveal some differences between the cells fabricated with incorporation of different blocking layers. In this case, the best performing cell was that without a blocking layer. Among the rest of the cells discussed in this section, they can be divided into three groups based on the characteristics of their current voltage curves. First group consist of three cells which curves look very similar thus their photovoltaic parameters in general are similar as well. These sells are C_{BL}30/0.11, C_{BL}30/0.18 and C_{BL}30/0.26. Their main difference comparing their curves with the curve of the standard-type cell is lower short-circuit current. Second distinguished type of curve belongs to cell C_{BL}30/0.14. In general it differs from the previous group by the amount of short circuit current. The last group of cells is more distinctive from all other cells. This group consist of the cells C_{BL}30/1.00 and C_{BL}30/2.00. Their curves clearly shows that the series resistance was significantly increased and the shunt resistance was notably decreased with increase of the oxygen partial

pressure in this case thus the performance was diminished even though the short circuit-current densities were only lower than that of the standard DSSC. More differences can be observed from detailed view on the photovoltaic parameters of all those cell.

Figure 5.13 presents efficiencies of fabricated standard-type DSSC without blocking layer and prepared DSSCs incorporating deposited titanium oxide thin films as blocking layers. The blocking layers were deposited at deposition duration of 30 minutes and under different oxygen partial pressure conditions. The values of efficiencies are presented as a function of oxygen partial pressure used for the deposition of the BL that was included in the solar cell structure. The efficiencies were calculated based on the photocurrent-voltage characteristics of best-performing DSSCs that were obtained under simulated full sunlight illumination conditions. Each efficiency value was calculated from the second cycle of the three-cycle current-voltage characterisation of the cells. The exact values of the efficiencies can be found in Table 5.7.

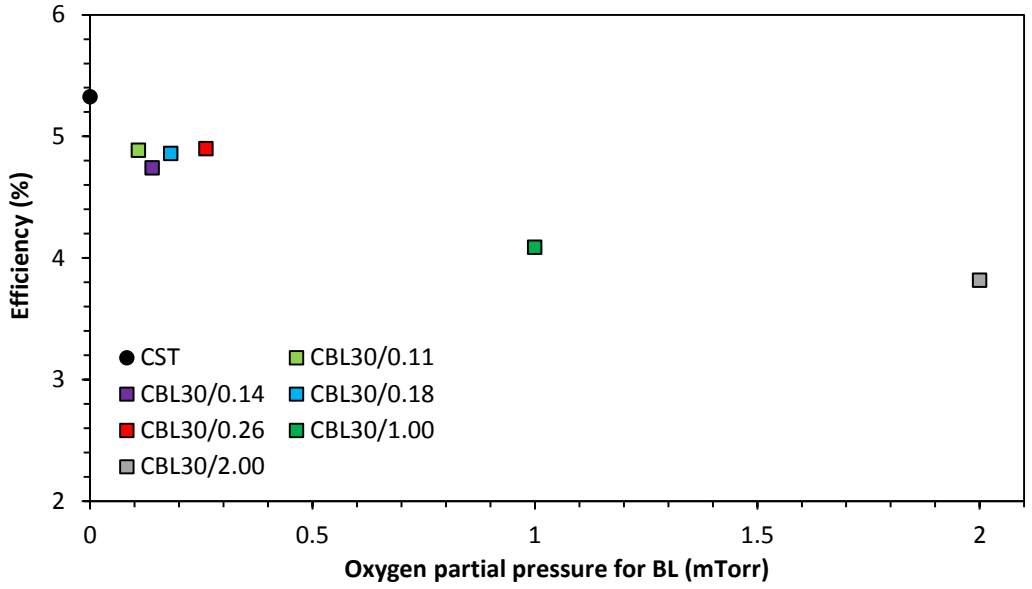

Figure 5.13: Efficiencies of illuminated best-performing DSSCs without and with BLs deposited at deposition duration of 30 minutes against the oxygen partial pressure used for deposition of these BLs.

Closer look at the calculated efficiencies of the cells shows that the best conversion efficiency was obtained from the standard cell, as was assumed from the current-voltage curve. It is also confirmed that the three distinguished cells with blocking layer, which curves were very similar, feature very similar efficiencies. Although the current-voltage curve of the cell $C_{BL}30/0.14$ was tangibly separated from those three cells, its conversion efficiency is not that distinctively different. The two other cells presented efficiencies notably lower and also shows some difference between themselves. Generally, clear trend can be seen among all the cells with blocking layers deposited under different oxygen partial pressure. The higher the partial pressure the lower is the efficiency of the cell.

Short-circuit current densities of fabricated standard-type DSSC without blocking layer and DSSCs incorporating deposited titanium oxide thin films as blocking layers are presented in Figure 5.14. The blocking layers were PLD-deposited with deposition duration of 30 minutes and under different oxygen partial pressure conditions. The values of the short-circuit current densities are presented as a function of oxygen partial pressure used for the deposition of the BL that was incorporated into the structure of the DSSC. The short-circuit current densities were computed based on the current-voltage characteristics of best-performing DSSCs of each type that were characterised under simulated full sunlight illumination conditions. Each value of the short-circuit current density was calculated from the second cycle of the three-cycle current-voltage characterisation of the cells. The exact values of the short-circuit current densities are presented in Table 5.7.

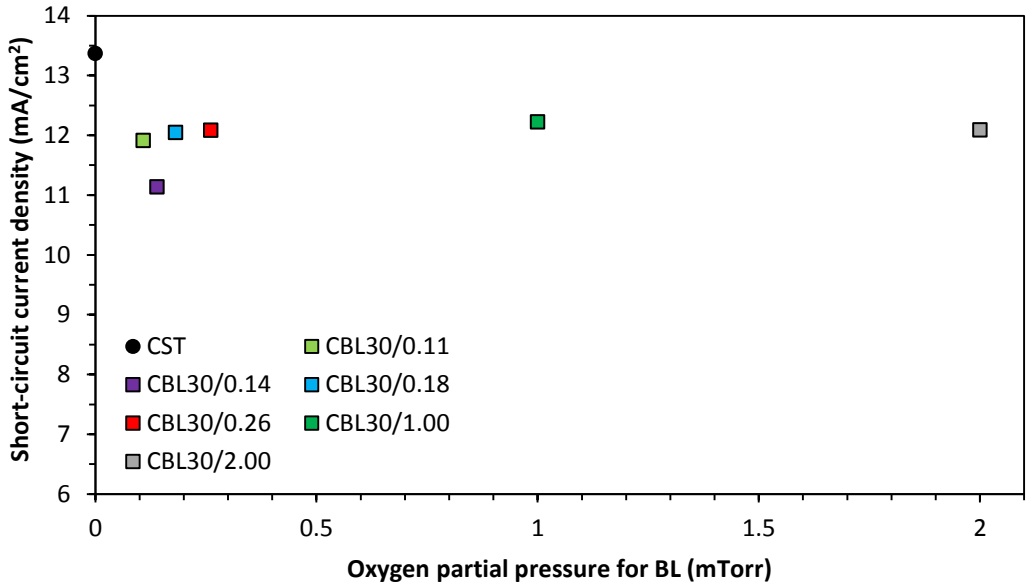

Figure 5.14: Short-circuit current densities of illuminated best-performing DSSCs without and with BLs deposited at deposition duration of 30 minutes against the oxygen partial pressure used for deposition of these BLs.

Presented values of short-circuit current densities for best performing cells indicates that in general almost all of these cells produced similar amount of the current. Only some not very distinctive trend can be seen, where current is slightly higher for cells with blocking layer obtained under higher oxygen partial pressure. Besides, one cell produced relatively smaller current when blocking layer was obtained under small oxygen partial pressure. It can be concluded that most of the cells presented in this section was capable of producing similar amount of current regardless the light transmittance aspect of deposited thin film of titanium oxide.

Open-circuit voltages of prepared standard DSSC without blocking layer and DSSCs including PLD-deposited blocking layers of titanium oxide thin films are presented in Figure 5.15. The blocking layers were deposited with deposition duration of 30 minutes and under various oxygen partial pressure conditions. The values of the open-circuit voltages are presented as a function of oxygen partial pressure used for the deposition of the BL that was included in the structure of the DSSC. The values of the open-circuit voltages were obtained from

the current-voltage characteristics of best-performing DSSCs of each type that were tested under simulated sunlight illumination conditions. Each value of the open-circuit voltage was retrieved from the second cycle of the three-cycle current-voltage characterisation of the cells. The exact values of the open-circuit voltages are detailed in Table 5.7.

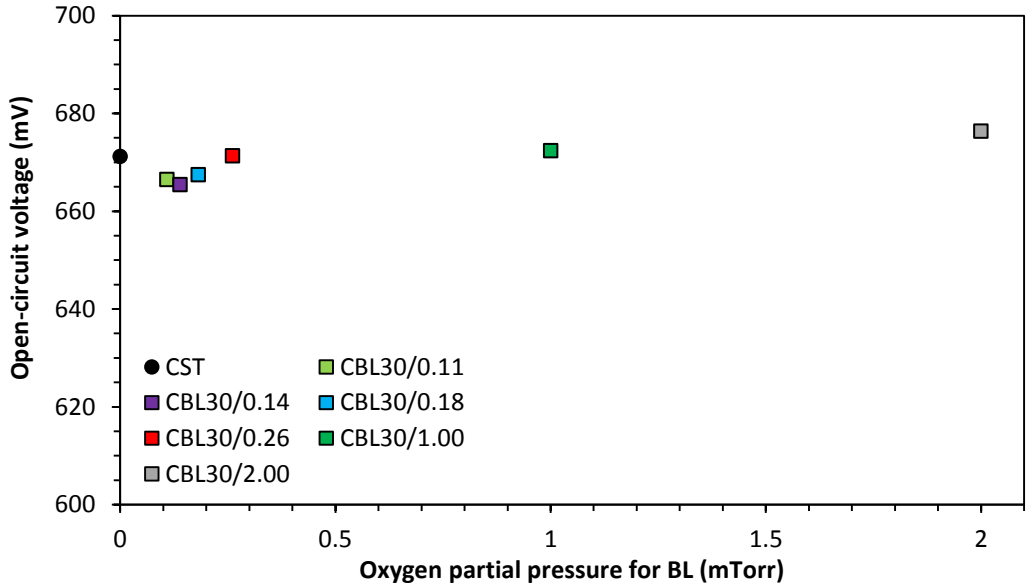

Figure 5.15: Open-circuit voltages of illuminated best-performing DSSCs without and with BLs deposited at deposition duration of 30 minutes against the oxygen partial pressure used for deposition of these BLs.

Presented results of open-circuit voltages shows that for cells with blocking layer deposited under lower oxygen partial pressures the obtained voltage is somewhat smaller than that of the standard-type DSSC and the cells where blocking layer was deposited under higher oxygen partial pressure the V_{OC} tends to increase and somewhat exceed the voltage of standard DSSC. However, the differences between the voltages in this group of presented cells are not significant enough to univocally state this conclusion.

Figure 5.16 shows fill factors of the fabricated standard DSSC without blocking layer and DSSCs including deposited titanium oxide blocking layers.

The thin film blocking layers were deposited at deposition duration of 30 minutes and under different oxygen partial pressure conditions. The values of the fill factors are presented as a function of oxygen partial pressure used for the deposition of the BL that was incorporated in the structure of the DSSC. Computations of the values of the fill factors were based on the current-voltage characterisation of best-performing DSSCs of each type which were characterised under simulated full sunlight conditions. Each value of the fill factor was calculated from the second cycle of the current-voltage characteristics of the cells. The exact values of the fill factors are presented in Table 5.7.

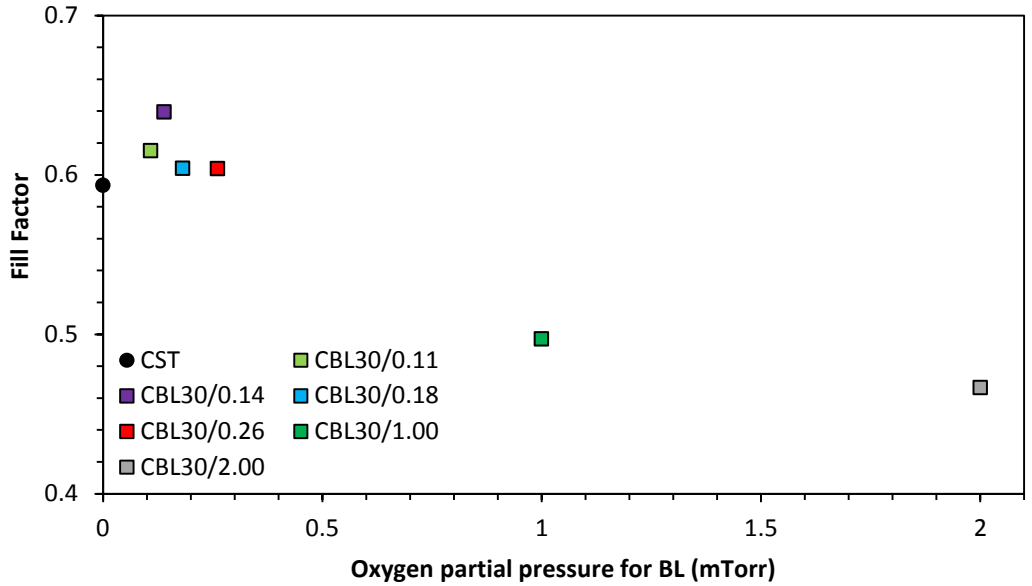

Figure 5.16: Fill factors of illuminated best-performing DSSCs without and with BLs deposited at deposition duration of 30 minutes against the oxygen partial pressure used for deposition of these BLs.

Presented values of fill factors of the cells with blocking layer are distinctively different from each other as well as they differ from the standard cell. It is clearly seen that the blocking layers that include blocking layer deposited under lower oxygen partial pressure conditions feature large increase of the fill factor. The highest fill factor equal to 0.64 was achieved for the cell with blocking

layer obtained under p_{O_2} equal to 0.14 mTorr, and second best fill factor equal to 0.62 was obtained for the cell with blocking layer deposited under somewhat smaller oxygen partial pressure. Also two cells with blocking layer obtained under oxygen partial pressures of 0.18 mTorr and 0.26 mTorr present enhancement of the fill factor to some extent. As the fill factor depends on the ideality factor, which is related with the type of recombination processes occurring in the cell, it can be assumed that the increase of the fill factor or these cells indicates suppression of some od the undesired recombination processes. It can be also seen that the further increase of the oxygen partial pressure used for deposition of BL result in largely decrease of the fill factor value.

5.4.2 Characterisation of sets of fabricated cells

Figure 5.17 shows averaged efficiencies of the sets of fabricated DSSCs. The averaged efficiency values are calculated for the set of standard-type DSSCs prepared without blocking layer, named as C_{ST}, and for the sets of DSSCs prepared with various deposited titanium oxide films as blocking layers, which names begin with C_{BL}. The thin film blocking layers were deposited at deposition duration of 30 minutes and under different oxygen partial pressure between 0.11 mTorr and 2.00 mTorr. The averaged values of the efficiencies are presented as a function of oxygen partial pressure relevant to the type of the BL which was incorporated into the cell structure of the set of DSSCs. Calculations of the average values of efficiencies were based on the cells efficiencies computed form the photocurrent-voltage characteristics of the sets of DSSCs that were tested under simulated full sunlight conditions. Each averaged value of the efficiency was calculated from the efficiency of the second cycle of the current-voltage characteristics and is presented along with an error bar representing a standard error of the mean. The exact averaged values of the efficiencies are presented in Table 5.8 along with errors of estimation and BLs deposition conditions.

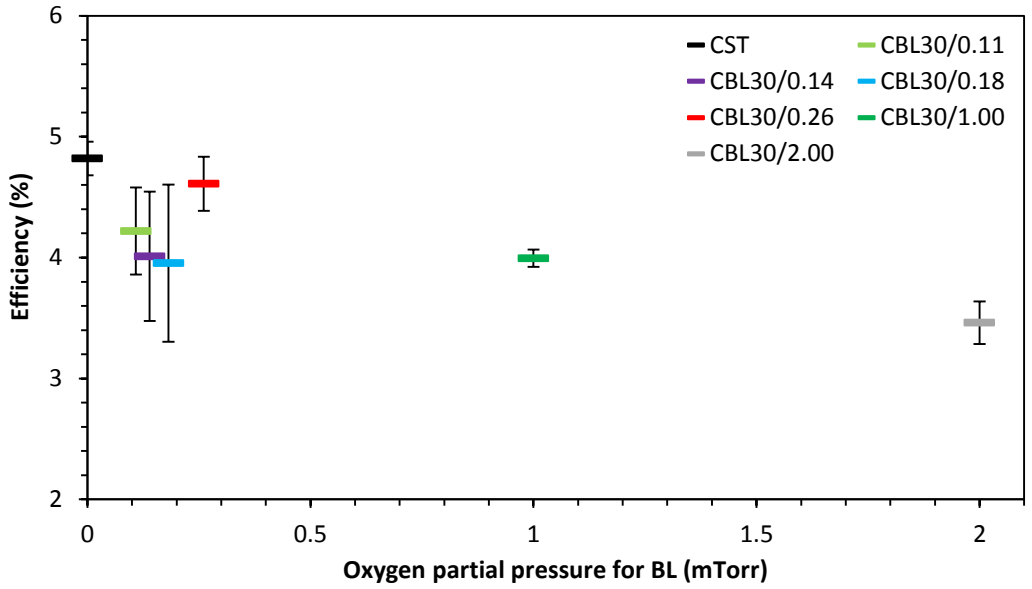

Figure 5.17: Averaged efficiencies of illuminated sets of DSSCs without and with BLs deposited at deposition duration of 30 minutes against the oxygen partial pressure used for deposition of these BLs.

Table 5.8: Averaged efficiencies of illuminated sets of DSSCs without and with BLs deposited at deposition duration of 30 minutes including errors of estimation and deposition conditions.

sample	deposition duration (min)	Oxygen partial pressure (mTorr)	cell efficiency - averaged, η (%)	standard deviation (%)	standard error (%)
C_{ST}	-	-	4.82	0.41	0.14
$C_{BL}30/0.11$	30	0.11	4.22	0.62	0.36
$C_{BL}30/0.14$		0.14	4.01	0.92	0.53
$C_{BL}30/0.18$		0.18	3.95	1.13	0.65
$C_{BL}30/0.26$		0.26	4.61	0.39	0.22
$C_{BL}30/1.00$		1.00	3.99	0.12	0.07
$C_{BL}30/2.00$		2.00	3.46	0.31	0.18

The averaged values of the efficiencies shows that majority of the cells with different blocking layers of the typical thickness of 53 nm did not perform better than the standard cells without any blocking layer. Based on the average values, only cells with blocking layer deposited under the oxygen partial pressure of 0.26 mTorr were able to obtain efficiency close to that of the standard-type DSSCs. Other samples show trend to decrease the efficiencies if the oxygen partial pressure used for deposition of BLs increase. This trend takes place when the value of p_{O_2} is above or below the 0.26 mTorr. It may indicate that optimal oxygen partial pressure for BL deposition is about this value. The transmittance measurements showed that samples of thin film deposited under 0.26 mTorr and 0.18 mTorr of oxygen partial pressure feature intermediate transmittance among all samples analysed in this section. On the other hand, results from the electrical resistance measurement showed that sample of thin film deposited under p_{O_2} equal to 0.26 mTorr possess intermediate value of the electrical resistance among other analysed samples. Considering both properties of the films and results from DSSCs characterisation it can be assumed that the performance of DSSCs with this type of blocking layers is negatively affected either by lower transmittance as a consequence of use of oxygen partial pressure below 0.26 mTorr, or the performance is adversely affected by higher resistance as a consequence of use of oxygen partial pressure above 0.26 mTorr. From sample composition point of view, it was shown that samples prepared about this value of oxygen concentration possess different ratio between rutile phase and anatase phase. However, considering intrinsic properties of these two phases and direction of change of their ratio, towards more rutile phase with increase of p_{O_2}, suggests opposite trend in change of the electrical and optical properties than obtained in this study. On the other hand, possible increase of amount of TiO_2 over other compound from Ti-O system can match the trend of changes in the electrical and optical properties, however presence of other compounds in the film was not unambiguously confirmed by composition analysis.

Figure 5.18 presents averaged short-circuit current densities of the sets of prepared DSSCs. The averaged values of short-circuit current densities are calculated for the set of standard DSSCs fabricated without blocking layer and for the sets of DSSCs fabricated with various deposited titanium oxide films as blocking layers. The blocking layers were deposited with deposition duration of 30 minutes and under different oxygen partial pressure. The averaged values of the short-circuit current densities are presented as a function of oxygen partial pressure relevant to the type of the BL which was incorporated as a part of the structure of the cell of set of DSSCs. The average values of short-circuit current densities were calculated based on the cells short-circuit current densities computed form the current-voltage characteristics of the sets of DSSCs that were characterised under simulated sunlight conditions. Each averaged value of the short-circuit current density was calculated from the short-circuit current densities of the second cycle of the current-voltage characteristics and is presented along with the error bar representing the standard error of the mean. The exact averaged values of the short-circuit current densities are included in Table 5.9 along with the errors of estimation and BLs deposition conditions.

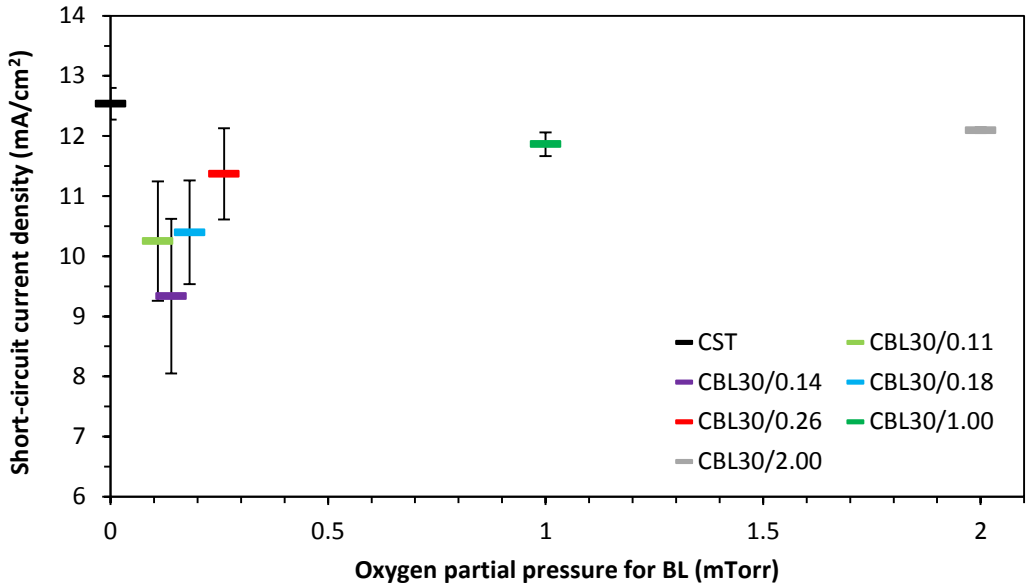

Figure 5.18: Averaged short-circuit current densities of illuminated sets of DSSCs without and with BLs deposited at deposition duration of 30 minutes against the oxygen partial pressure used for deposition of these BLs.

Table 5.9: Averaged short-circuit current densities of illuminated sets of DSSCs without and with BLs deposited at deposition duration of 30 minutes including errors of estimation and deposition conditions.

sample	deposition duration (min)	Oxygen partial pressure (mTorr)	cell short-circuit current density - averaged, J_{SC} (mA/cm^2)	standard deviation (mA/cm^2)	standard error (mA/cm^2)
C_{ST}	-	-	12.53	0.79	0.26
$C_{BL}30/0.11$	30	0.11	10.25	1.72	0.99
$C_{BL}30/0.14$		0.14	9.34	2.23	1.29
$C_{BL}30/0.18$		0.18	10.40	1.49	0.86
$C_{BL}30/0.26$		0.26	11.37	1.31	0.76
$C_{BL}30/1.00$		1.00	11.86	0.34	0.20
$C_{BL}30/2.00$		2.00	12.09	0.08	0.05

The averaged values of the short-circuit current densities shows a trend of decrease the short-circuit current when the value if used p_{O_2} was decreased. This trend occurs until the value of oxygen partial pressure equal to 0.14 mTorr when the shirt-circuit current start to increase with further decrease of used oxygen partial pressure for BL deposition. Calculated errors of estimation for averaged values in lower pressure region are not very different from each other, therefore observed trend possibly originate from the properties of the blocking layer rather than from randomness of the results. Possibly, the value of p_{O_2} where the trend changes the direction is the point where effect of improvement of electrical resistance overcomes the effect of deterioration of optical transmittance of the film used as blocking layer. At large, none of the samples with BLs exhibited higher averaged short-circuit current density than the DSSCs without BL.

Averaged open-circuit voltages of the sets of fabricated DSSCs are presented in Figure 5.19 The averaged values of open-circuit voltages are calculated for the set of standard DSSCs fabricated without blocking layer and for the sets of DSSCs fabricated with different deposited films of titanium oxide as blocking layers. The blocking layers were PLD-deposited with deposition duration of 30 minutes and under different oxygen partial pressure. The averaged values of the open-circuit voltages are presented as a function of oxygen partial pressure relevant to the type of the BL which was incorporated into the cell structure of the set of DSSCs. The average values of open-circuit voltages were calculated based on the cells open-circuit voltages retrieved from the current-voltage characteristics of the sets of DSSCs that were tested under simulated full sunlight conditions. Each averaged value of the open-circuit voltages was calculated from the open-circuit voltages obtained from the second cycle of the current-voltage characteristics and is presented along with the error bar representing the standard error of the mean. The exact average values of the open-circuit voltages are detailed in Table 5.10 along with the errors of estimation and BLs deposition conditions.

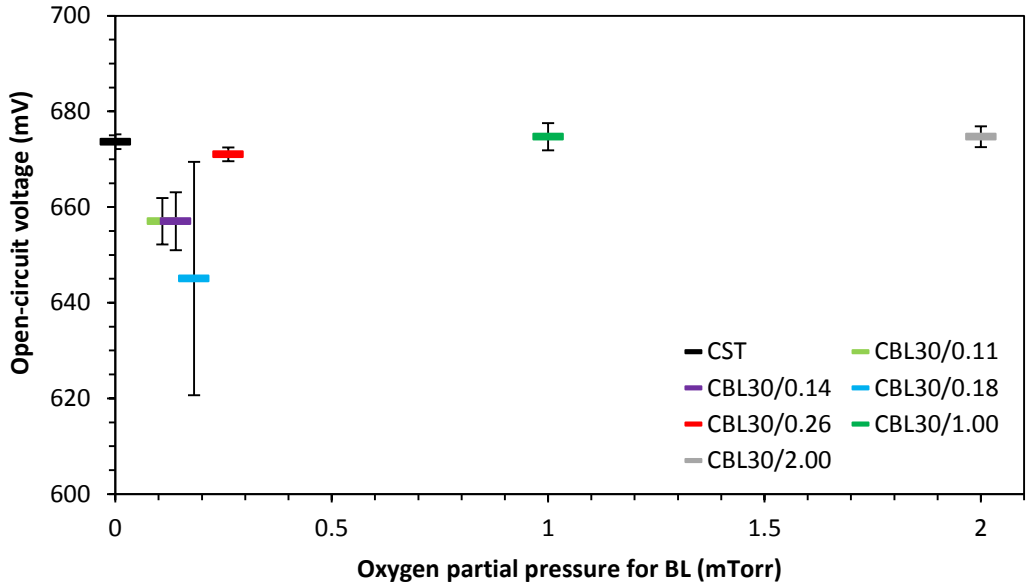

Figure 5.19: Averaged open-circuit voltages of illuminated sets of DSSCs without and with BLs deposited at deposition duration of 30 minutes against the oxygen partial pressure used for deposition of these BLs.

Table 5.10: Averaged open-circuit voltages of illuminated sets of DSSCs without and with BLs deposited at deposition duration of 30 minutes including errors of estimation and deposition conditions.

sample	deposition duration (min)	Oxygen partial pressure (mTorr)	cell open-circuit voltage - averaged, V_{OC} (mV)	standard deviation (mV)	standard error (mV)
C_{ST}	-	-	673.7	4.6	1.5
$C_{BL}30/0.11$	30	0.11	657.0	8.4	4.9
$C_{BL}30/0.14$		0.14	657.0	10.4	6.0
$C_{BL}30/0.18$		0.18	645.1	42.2	24.4
$C_{BL}30/0.26$		0.26	671.0	2.5	1.4
$C_{BL}30/1.00$		1.00	674.7	4.9	2.8
$C_{BL}30/2.00$		2.00	674.7	3.8	2.2

The averaged values of the open-circuit voltages does not show to be strongly affected by type of the blocking layer within the region between 0.26 mTorr and 2.00 mTorr and their values are similar to that of the standard-type DSSC. However for lower values of oxygen partial pressures the open-circuit voltage is notably lower. Although the averaged value of the open-circuit voltages for the set of cells $C_{BL}30/0.18$ is the lowest, it should be noted that among these three samples one of them performed outstandingly worse which probably originate from its manufacturing process. Except this cell, two others obtained the open circuit voltage similar to that of the set of $C_{BL}30/0.26$.

Averaged fill factors of the sets of fabricated DSSCs are shown in Figure 5.20. The averaged values of the fill factors are calculated for the set of standard-type DSSCs fabricated without blocking layer and for the sets of DSSCs fabricated with different blocking layers that were PLD-deposited as thin film of titanium oxide. The blocking layers were deposited at deposition duration of 30 minutes and under different oxygen partial pressure. The averaged values of the fill factors are presented as a function of oxygen partial pressure relevant to the type of the BL which was included in the cell structure of the set of DSSCs. The average values of fill factors were computed based on the cells fill factors calculated from the current-voltage characteristics of the sets of DSSCs tested under simulated full sunlight conditions. Each averaged value of the fill factor was calculated from the fill factors obtained from the second cycle of the current-voltage characteristics and is presented on the graph along with the error bar representing the standard error of the mean. The exact average values of the fill factors are shown in Table 5.11 along with the errors of estimation and BLs deposition conditions.

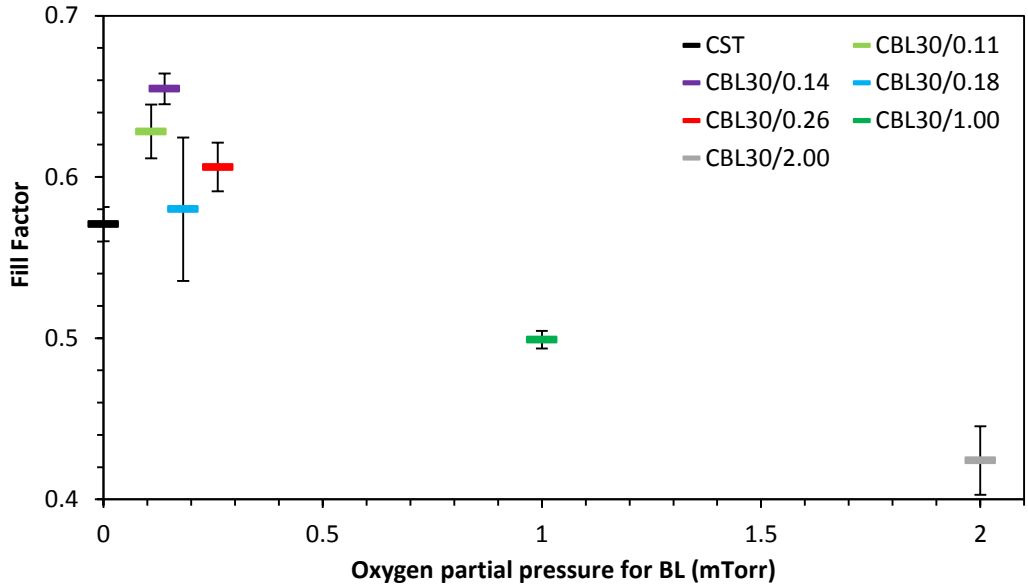

Figure 5.20: Averaged fill factors of illuminated sets of DSSCs without and with BLs deposited at deposition duration of 30 minutes against the oxygen partial pressure used for deposition of these BLs.

Table 5.11: Averaged fill factors of illuminated sets of DSSCs without and with BLs deposited at deposition duration of 30 minutes including errors of estimation and deposition conditions.

sample	deposition duration (min)	Oxygen partial pressure (mTorr)	cell Fill Factor - averaged, FF	standard deviation	standard error
C_{ST}	-	-	0.57	0.03	0.01
$C_{BL}30/0.11$	30	0.11	0.63	0.03	0.02
$C_{BL}30/0.14$		0.14	0.65	0.02	0.01
$C_{BL}30/0.18$		0.18	0.58	0.08	0.04
$C_{BL}30/0.26$		0.26	0.61	0.03	0.02
$C_{BL}30/1.00$		1.00	0.50	0.01	0.01
$C_{BL}30/2.00$		2.00	0.42	0.04	0.02

The averaged values of the fill factors shows clearly that the cells with blocking layers deposited under lower oxygen partial pressures up to 0.26 mTorr benefit from incorporation of the blocking layer into their structure. Among them, the biggest increment was obtained for the set of cells $C_{BL}30/0.14$ which obtained averaged value of the fill factor equal to 0.65 while the standard type cells average fill factor is only about 0.57. Considering the fact that the fill factor is strongly related with recombination processes occurring in the cell, it can be concluded that the use of this type of blocking layers can be beneficial especially when other related problems, like poorer optical transmittance will be overcame.

Chapter 6: Conclusions and future work

6.1 Conclusions

The project is aimed at developing novel blocking layers based on titanium oxides and investigating their effects on the performances of dye-sensitized solar cells. Major findings of this research project are summarized as follows:

1. A systematic investigation on growth of titanium oxide thin films by pulsed laser deposition was carried to determine the correlation between the deposition conditions and electrical properties of the deposited titanium oxide thin films. The results obtained from this work demonstrate that electrical resistivity of the deposited thin films can be manipulated by controlling partial oxygen pressure in the deposition chamber using a TiO target, while the thickness of the thin film is mainly determined by the duration of deposition. The process is repeatable and can be carried out in relatively low substrate temperature (300 ^{o}C). This is particularly an important feature when the titanium oxide thin films are required to be deposited on functional substrates such as transparent conductive glass for solar cells.

2. Attempts have been made to characterise the physical, chemical and structural properties of deposited titanium oxides of varied electrical resistivities. The results of XRD and SEM analysis indicate that the change of electrical resistivity of the deposited thin films is associated with compositional and structural changes, resulting in formation of titanium sub-oxides or their mixtures. The characterisation of the optical properties of the deposited titanium oxide thin films reveals a correlation between the light transmittance and the electrical resistivity.

3. In order to facilitate the study of the possibility of using the titanium oxides as the blocking layers, a good adherence between the titanium oxide thin film and the transparent conductive glass is essential. This work demonstrates

successfully that the titanium oxide thin films of varied electrical resistivities and thicknesses can be deposited on fluorine doped tin oxide glass substrates with good adhesion. The electrical and optical properties of the combined transparent conductor and blocking layers were characterised. The results of sheet resistance measurement show that the combined layers exhibit similar dependence of the layer resistance on the partial oxygen pressure. The results of I-V measurements indicate that non-linear behaviour appears in some samples of fluorine-doped-tin-oxide/titanium-oxide interface.

4. Dye-sensitized solar cells (DSSC) were fabricated with titanium oxide layers deposited on the FTO electrodes as blocking layers. The dye-sensitized solar cells were manufactured in-house at the Cardiff Thermoelectric Laboratory based on conventional structure and fabrication process with the aid of screen-printing of TiO_2 semiconductor layers. To date, this is the first time that PLD-deposited titanium sub-oxide thin films with different electrical conductivities have been investigated as potential blocking layers in dye-sensitized solar cells to prevent electron-hole recombination at the electrode/electrolyte interfaces.

5. A systematic study was carried out to identify the appropriate thickness of the blocking layers. The results obtained from this study show that all key performance parameters of the solar cells (i.e., open circuit voltage, short circuit current, fill factor and conversion efficiency) are affected by the thickness of the blocking layers. The solar cell with the thinnest blocking layer exhibit highest efficiency among all cells including the one without blocking layer. It is apparent that the blocking layer can improve the conversion efficiency of the dye-sensitized solar cells due to increase in the open circuit voltage and fill factor, even though the short circuit is slightly reduced.

6. The effect of the partial oxygen pressure on the performance of dye-sensitized solar cells has been investigated systematically. The change in the partial oxygen pressure during fabrication led to compositional and structural variation, which is proportionally related to the change in electrical resistivity of the deposited layers. The results obtained from this study show clearly that all key performance parameters of solar cells vary with the partial oxygen pressure of the blocking layers. Although no overall improvement in conversion efficiency has been obtained in this group of samples, it can be seen that the fill-factor is increased in a cell that has relatively low electrical resistivity. The maximum FF value is obtained in sample CBL 30/0.14, which corresponds to deposition duration of 30 minutes under a partial oxygen pressure of 0.14 millitorr, and hence a significantly small electrical resistance compared with that observed in the usual TiO_2 blocking layers. This result indicates that a better blocking layer may be found in electrically conductive titanium sub-oxide rather than in usual TiO_2, opening a new possibility of search for improved blocking layers.

6.2 Future work

The outcomes of this study demonstrated the promise of new type of blocking layers based on titanium sub-oxides rather than usual titanium dioxide. However, there are many questions that remain to be addressed. In order to assist in search for the best blocking layers, further investigations in the following aspects are required:

1. Explore advanced characterisation techniques to achieve more accurate determination of compositions and structures of deposited thin films. This will, in turn, facilitate an in-depth study of the relationship between the deposition conditions and the properties (phase and composition) of the deposited thin films. The improved knowledge of such relationship is

essential to preparation of well-defined titanium oxide layers for further detailed investigation.

2. The deposition of titanium oxides will be further investigated extensively to determine the optimal conditions, under which the best thickness of pinhole-free titanium oxide layers will be identified and the most appropriate oxygen content will be determined to produce the most effective blocking layers. The results of this work indicated that the blocking layers should be thin so that the electrons can tunnel through easily while still preventing the holes to react with electrons on the electrode. In addition, using a very thin blocking layer, the light transmittance across the blocking layer can be ensured even if using highly electrical conductive layers.

3. In order to achieve the accurate control of deposition conditions to produce well-defined blocking layers, fine-tune of the PLD machine may be required. This can be achieved by exploring the control of other deposition parameters such as laser repetition rate, substrate temperature and total gas pressure in the deposition chamber, etc.

4. I-V measurements of the interface between the titanium oxide layer and fluorine doped tin oxide layer reveal the non-linear characteristics in some samples, which would have very different impact on the performance of the blocking layers compared to those with linear characteristics. The effect of I-V characteristics of such interfaces on the performance of the blocking layer will be investigated.

5. Explore the possibility of growing titanium oxide layers on other transparent conductive substrates and investigate the optical and electrical properties of deposited layers.

References

Abdullah, M.H. et al., 2013. Novel encapsulated ITO/arc-ZnO:TiO2 antireflective passivating layer for TCO conducting substrate prepared by simultaneous radio frequency-magnetron sputtering. *Microelectronic Engineering*, 108, pp.138–144.

Abdullah, M.H. & Rusop, M., 2013. Multifunctional graded index TiO2 compact layer for performance enhancement in dye sensitized solar cell. *Applied Surface Science*, 284, pp.278–284.

Achutharaman, V.S. et al., 1994. Origin of RHEED intensity oscillations during the growth of (Y,Dy)Ba2Cu3O7-x thin films. *Physical Review B*, 50(11), pp.8122–8125.

Adams, W.G. & Day, R.E., 1877. The Action of Light on Selenium. *Proceedings of the Royal Society, London*, A25, p.113.

Alferov, Z.I. et al., 1971. Solar-energy converters based on pn AlxGa(1-x)As-GaAs heterojunctions. *Soviet Physics Semiconductors*, 4(12), p.2047.

Bailes, M. et al., 2005. Determination of the Density and Energetic Distribution of Electron Traps in Dye-Sensitized Nanocrystalline Solar Cells. *The Journal of Physical Chemistry B*, 109(32), pp.15429–15435.

Becquerel, A.E., 1841. Mémoire sur les effets électriques produits sous l'influence des rayons solaires. *Annalen der Physick und Chemie*, 54, pp.35–42.

Berginc, M. et al., 2007. The effect of temperature on the performance of dye-sensitized solar cells based on a propyl-methyl-imidazolium iodide electrolyte. *Solar Energy Materials and Solar Cells*, 91(9), pp.821–828.

Bergmann, L., 1931. Uber eine neue Selen- Sperrschicht Photozelle. *Physikalische Zeitschrift*, 32, p.286.

Bills, B., Shanmugam, M. & Baroughi, M.F., 2011. Effects of atomic layer deposited HfO2 compact layer on the performance of dye-sensitized solar cells. *Thin Solid Films*, 519(22), pp.7803–7808.

Blanchet, G.B. et al., 1993. Laser Ablation and the Production of Polymer Films. *Science*, 262(5134), pp.719–721.

Bryant, D. et al., 2016. Light and oxygen induced degradation limits the operational stability of methylammonium lead triiodide perovskite solar cells. *Energy & Environmental Science*, 9(5), pp.1655–1660.

Cahen, D. et al., 2000. Nature of Photovoltaic Action in Dye-Sensitized Solar Cells. *The Journal of Physical Chemistry B*, 104(9), pp.2053–2059.

Cameron, P.J. et al., 2004. Electrochemical studies of the Co(III)/Co(II)(dbbip)2 redox couple as a mediator for dye-sensitized nanocrystalline solar cells. *Coordination Chemistry Reviews*, 248(13–14), pp.1447–1453.

Cameron, P.J. & Peter, L.M., 2003. Characterization of titanium dioxide blocking layers in dye-sensitized nanocrystalline solar cells. *The Journal of Physical Chemistry B*, 107(51), pp.14394–14400.

Cameron, P.J. & Peter, L.M., 2005. How Does Back-Reaction at the Conducting Glass Substrate Influence the Dynamic Photovoltage Response of Nanocrystalline Dye-Sensitized Solar Cells? *The Journal of Physical Chemistry B*, 109(15), pp.7392–7398.

Cameron, P.J., Peter, L.M. & Hore, S., 2005. How Important is the Back Reaction of Electrons via the Substrate in Dye-Sensitized Nanocrystalline Solar Cells? *The Journal of Physical Chemistry B*, 109(2), pp.930–936.

Chang, W. et al., 1998. The Effect of (Ba,Sr) and (Mn,Fe,W) Dopants on the Microwave Properties of BaxSr1−xTiO3 Thin Films. *MRS Proceedings*, 541(January), p.699.

Chapin, D.M., Fuller, C.S. & Pearson, G.L., 1954. A new silicon p-n junction photocell for converting solar radiation into electrical power. *Journal of Applied Physics*, 25(5),

pp.676–677.

Chen, C.H., Kelder, E.M. & Schoonman, J., 1999. Electrostatic sol-spray deposition (ESSD) and characterisation of nanostructured TiO2 thin films. *Thin Solid Films*, 342(1–2), pp.35–41.

Chiba, Y. et al., 2006. Dye-sensitized solar cells with conversion efficiency of 11.1%. *Japanese Journal of Applied Physics, Part 2: Letters*, 45(24–28).

Christen, H.-M. et al., 1998. Long-range ferroelectric interactions in KTaO3/KNbO3 superlattice structures. *Applied Physics Letters*, 72(20), pp.2535–2537.

Christen, H. -M. et al., 1996. The growth and properties of epitaxial KNbO3 thin films and KNbO3/KTaO3 superlattices. *Applied Physics Letters*, 68(11), pp.1488–1490.

Cristescu, R. et al., 2003. New results in pulsed laser deposition of poly-methyl-methacrylate thin films. *Applied Surface Science*, 208–209, pp.645–650.

Czochralski, J., 1918. Ein neues Verfahren zur Messung der Kristallisationsgeschwindigheit der Metalle. *Zeitschrift für physikalische Chemie*, 92, pp.219–221.

Diamant, Y. et al., 2004. Core–shell nanoporous electrode for dye sensitized solar cells: the effect of shell characteristics on the electronic properties of the electrode. *Coordination Chemistry Reviews*, 248(13–14), pp.1271–1276.

Dürr, M. et al., 2005. Low-temperature fabrication of dye-sensitized solar cells by transfer of composite porous layers. *Nature materials*, 4(8), pp.607–11.

Durrant, J.R., Haque, S.A. & Palomares, E., 2004. Towards optimisation of electron transfer processes in dye sensitised solar cells. *Coordination Chemistry Reviews*, 248(13–14), pp.1247–1257.

Einstein, A., 1905. On a Heuristic Viewpoint Concerning the Production and Transformation of Light. *Annalen der Physik*, 17(6), pp.132–148.

Fabregat-Santiago, F. et al., 2003. Mott-Schottky Analysis of Nanoporous Semiconductor Electrodes in Dielectric State Deposited on SnO2 (F) Conducting Substrates. *Journal of The Electrochemical Society*, 150(6), pp.E293–E298.

Fritts, C.E., 1883. On a new form of selenium cell, and some electrical discoveries made by its use. *American Journal of Science*, s3-26(156), pp.465–472.

Fujishima, A. & Honda, K., 1972. Electrochemical Photolysis of Water at a Semiconductor Electrode. *Nature*, 238(5358), pp.37–38.

García-Cañadas, J. & Min, G., 2014. Multifunctional probes for high-throughput measurement of Seebeck coefficient and electrical conductivity at room temperature. *Review of Scientific Instruments*, 85(4), p.43906.

Gerischer, H. et al., 1968. Sensitization of charge injection into semiconductors with large band gap. *Electrochimica Acta*, 13(6), pp.1509–1515.

Góes, M.S. et al., 2012. Impedance Spectroscopy Analysis of the Effect of TiO2 Blocking Layers on the Efficiency of Dye Sensitized Solar Cells. *The Journal of Physical Chemistry C*, 116, pp.12415–12421.

Gong, J., Liang, J. & Sumathy, K., 2012. Review on dye-sensitized solar cells (DSSCs): Fundamental concepts and novel materials. *Renewable and Sustainable Energy Reviews*, 16(8), pp.5848–5860.

Goossens, A., Maloney, E.-L. & Schoonman, J., 1998. Gas-Phase Synthesis of Nanostructured Anatase TiO2. *Chemical Vapor Deposition*, 4(3), pp.109–114.

Goto, H. & Hattori, R., 2006. High Temperature Sputtered TiO2 Film as an Efficient Blocking Layer for the Dye-sensitized Solar Cells. *Electrochemistry*, 74(6), pp.484–486.

Grätzel, M., 2001. Photoelectrochemical cells. *Nature*, 414(November), pp.338–344.

Grätzel, M., 2009. Recent Advances in Sensitized Mesoscopic Solar. *Accounts of*

Chemical Research, 42(11), pp.1788–1798.

Grätzel, M., 2005. Solar Energy Conversion by Dye-Sensitized Photovoltaic Cells. *Inorganic Chemistry*, 44(20), pp.6841–6851.

Gregg, B.A. et al., 2001. Interfacial Recombination Processes in Dye-Sensitized Solar Cells and Methods To Passivate the Interfaces. *The Journal of Physical Chemistry B*, 105(7), pp.1422–1429.

Grondahl, L.O., 1933. The copper-cuprous-oxide rectifier and photoelectric cell. *Reviews of Modern Physics*, 5(2), pp.141–168.

Gueymard, C.A., 2006. Reference solar spectra: Their evolution, standardization issues, and comparison to recent measurements. *Advances in Space Research*, 37(2), pp.323–340.

György, E. et al., 2005. Anatase phase TiO2 thin films obtained by pulsed laser deposition for gas sensing applications. *Applied Surface Science*, 247(1–4), pp.429–433.

Hagfeldt, A. & Grätzel, M., 2000. Molecular Photovoltaics. *Acc. Chem. Res.*, 33(5), pp.269–277.

Hanaor, D.A.H. & Sorrell, C.C., 2011. Review of the anatase to rutile phase transformation. *Journal of Materials Science*, 46(4), pp.855–874.

Hart, J.N. et al., 2006. TiO2 sol–gel blocking layers for dye-sensitized solar cells. *Comptes Rendus Chimie*, 9(5–6), pp.622–626.

Hertz, H., 1887. Ueber einen Einfluss des ultravioletten Lichtes auf die electrische Entladung. *Annalen der Physik und Chemie*, 267(8), pp.983–1000.

Holzapfel, B. et al., 1992. Off-axis laser deposition of YBa2Cu3O7−δ thin films. *Applied Physics Letters*, 61(26), pp.3178–3180.

Hore, S. & Kern, R., 2005. Implication of device functioning due to back reaction of

electrons via the conducting glass substrate in dye sensitized solar cells. *Applied Physics Letters*, 87(26), p.263504.

Huang, S.Y. et al., 1997. Charge Recombination in Dye-Sensitized Nanocrystalline TiO2 Solar Cells. *The Journal of Physical Chemistry B*, 101(14), pp.2576–2582.

Hwang, I. & Yong, K., 2016. Novel CdS Hole-Blocking Layer for Photostable Perovskite Solar Cells. *ACS Applied Materials and Interfaces*, 8(6), pp.4226–4232.

Inam, A. et al., 1988. As-deposited high Tc and Jc superconducting thin films made at low temperatures. *Applied Physics Letters*, 53(10), pp.908–910.

Ito, S. et al., 2005. Control of dark current in photoelectrochemical (TiO2/I--I3-)) and dye-sensitized solar cells. *Chemical communications (Cambridge, England)*, (34), pp.4351–4353.

Ito, S. et al., 2008. Fabrication of thin film dye sensitized solar cells with solar to electric power conversion efficiency over 10%. *Thin Solid Films*, 516(14), pp.4613–4619.

Jena, A. et al., 2012. Dye Sensitized Solar Cells : A Review Dye Sensitized Solar Cells : A Review. *Transactions of the Indian Ceramic Society*, 71(1), pp.1–16.

Jennings, J.R.R. & Peter, L.M.M., 2007. A reappraisal of the electron diffusion length in solid-state dye-sensitized solar cells. *Journal of Physical Chemistry C*, 111(44), pp.16100–16104.

Jenny, D.A., Loferski, J. & Rappaport, P., 1956. Photovoltaic Effect in GaAs p-n Jubctions and Solar Energy Conversion. *Physical Review*, 101(3), pp.1208–1209.

Juarez-Perez, E.J. et al., 2016. Thermal degradation of CH3NH3PbI3 perovskite into NH3 and CH3I gases observed by coupled thermogravimetry–mass spectrometry analysis. *Energy & Environmental Science*, 9(11), pp.3406–3410.

Kang, M.-S. et al., 2005. Roles of terminal groups of oligomer electrolytes in determining photovoltaic performances of dye-sensitized solar cells. *Chemical Communications*,

1(21), pp.2686–2688.

Karakitsou, K.E. & Verykios, X.E., 1993. Effects of altervalent cation doping of titania on its performance as a photocatalyst for water cleavage. *The Journal of Physical Chemistry*, 97(6), pp.1184–1189.

Kavan, L. et al., 1996. Electrochemical and photoelectrochemical investigation of single-crystal anatase. *Journal of the American Chemical Society*, 118(28), pp.6716–6723.

Kavan, L. et al., 1993. Preparation of TiO2 (anatase) films on electrodes by anodic oxidative hydrolysis of TiCl3. *Journal of Electroanalytical Chemistry*, 346(1), pp.291–307.

Kavan, L. & Grätzel, M., 1995. Highly efficient semiconducting TiO2 photoelectrodes prepared by aerosol pyrolysis. *Electrochimica Acta*, 40(5), pp.643–652.

Kay, A. & Graetzel, M., 1993. Artificial photosynthesis. 1. Photosensitization of titania solar cells with chlorophyll derivatives and related natural porphyrins. *The Journal of Physical Chemistry*, 97(23), pp.6272–6277.

Kim, H.-J. et al., 2012. Improved performance of dye-sensitized solar cells with compact TiO2 blocking layer prepared using low-temperature reactive ICP-assisted DC magnetron sputtering. *Journal of Industrial and Engineering Chemistry*, 18(5), pp.1807–1812.

Kim, J. et al., 2012. Ga-doped ZnO transparent electrodes with TiO2 blocking layer/nanoparticles for dye-sensitized solar cells. *Nanoscale Research Letters*, 7(11), pp.2–5.

Kim, J.H., Lee, S. & Im, H.S., 1999. Effect of target density and its morphology on TiO2 thin films grown on Si(100) by PLD. *Applied Surface Science*, 151(1), pp.6–16.

Kitazawa, S., 2004. In-situ Optical Spectroscopy of Ablation Plume for Preparations of Nanostructured TiO2 Thin Films by Pulsed Laser Deposition. *Japanese Journal of Applied Physics*, 43(No. 9A), pp.6335–6341.

Kitazawa, S., Choi, Y. & Yamamoto, S., 2004. In situ optical spectroscopy of PLD of nano-structured TiO2. *Vacuum*, 74(3–4), pp.637–642.

Kojima, A. et al., 2009. Organometal Halide Perovskites as Visible-Light Sensitizers for Photovoltaic. *Journal of the American Chemical Society*, 131(17), pp.6050–6051.

Kongkanand, A. et al., 2008. Quantum Dot Solar Cells. Tuning Photoresponse through Size and Shape Control of CdSe-TiO2 Architecture. *Journal of the American Chemical Society*, 130(12), pp.4007–4015.

Kopidakis, N., Neale, N.R. & Frank, A.J., 2006. Effect of an Adsorbent on Recombination and Band-Edge Movement in Dye-Sensitized TiO2 Solar Cells: Evidence for Surface Passivation. *The Journal of Physical Chemistry B*, 110(25), pp.12485–12489.

Kruger, J. et al., 2003. Charge transport and back reaction in solid-state dye-sensitised solar cells: a study using intensity-modulated photovoltage and photocurrent spectroscopy. *The Journal of Physical Chemistry B*, 107(31), pp.7536–7539.

Krüger, J. et al., 2001. High efficiency solid-state photovoltaic device due to inhibition of interface charge recombination. *Applied Physics Letters*, 79(13), pp.2085–2087.

van de Lagemaat, J., Park, N.-G. & Frank, A.J., 2000. Influence of Electrical Potential Distribution, Charge Transport, and Recombination on the Photopotential and Photocurrent Conversion Efficiency of Dye-Sensitized Nanocrystalline TiO2 Solar Cells: A Study by Electrical Impedance and Optical Modulation Tec. *The Journal of Physical Chemistry B*, 104(9), pp.2044–2052.

Landsberg, P.T. & Badescu, V., 2000. Carnot factor in solar cell efficiencies. *Journal of Physics D: Applied Physics*, 33(22), pp.3004–3008.

Lee, S. et al., 2009. Nb-Doped TiO2: A New Compact Layer Material for TiO2 Dye-Sensitized Solar Cells. *The Journal of Physical Chemistry C*, 113(16), pp.6878–6882.

Levy, B., Liu, W. & Gilbert, S.E., 1997. Directed Photocurrents in Nanostructured TiO2/SnO2 Heterojunction Diodes. *The Journal of Physical Chemistry B*, 101(10),

pp.1810–1816.

Li, W. et al., 2014. Generation of oxygen vacancies in visible light activated one-dimensional iodine TiO 2 photocatalysts. *RSC Advances*, 4(70), p.36959.

Lin, H. et al., 2008. Photocatalytic activity of pulsed laser deposited TiO2 thin films. *Materials Science and Engineering: B*, 151(2), pp.133–139.

Luca, D., Macovei, D. & Teodorescu, C.M., 2006. Characterization of titania thin films prepared by reactive pulsed-laser ablation. *Surface Science*, 600(18), pp.4342–4346.

Manca, M. et al., 2010. Charge recombination reduction in dye-sensitized solar cells by means of an electron beam-deposited TiO2 buffer layer between conductive glass and photoelectrode. *Thin Solid Films*, 518(23), pp.7147–7151.

Mardare, D. et al., 2000. On the structural properties and optical transmittance of TiO2 r.f. sputtered thin films. *Applied Surface Science*, 156(1–4), pp.200–206.

Matteocci, F. et al., 2016. Encapsulation for long-term stability enhancement of perovskite solar cells. *Nano Energy*, 30(December), pp.162–172.

Meyer, S., Gorges, R. & Kreisel, G., 2004. Preparation and characterisation of titanium dioxide films for catalytic applications generated by anodic spark deposition. *Thin Solid Films*, 450(2), pp.276–281.

Miettunen, K., Halme, J. & Lund, P., 2013. Metallic and plastic dye solar cells. *Wiley Interdisciplinary Reviews: Energy and Environment*, 2(1), pp.104–120.

Mills, A. et al., 2002. Novel TiO2 CVD films for semiconductor photocatalysis. *Journal of Photochemistry and Photobiology A: Chemistry*, 151(1–3), pp.171–179.

Nix, F.C. & Treptow, A.W., 1939. A Thallous Sulphide Photo-e.m.f. Cell. *Journal of the Optical Society of America*, 29(11), pp.457–462.

Norton, D.P., Budai, J.D. & Chisholm, M.F., 2000. Hydrogen-assisted pulsed-laser

deposition of (001)CeO2 on (001) Ge. *Applied Physics Letters*, 76(13), pp.1677–1679.

Nozik, A.J., 2005. Exciton Multiplication and Relaxation Dynamics in Quantum Dots: Applications to Ultrahigh-Efficiency Solar Photon Conversion. *Inorganic Chemistry*, 44(20), pp.6893–6899.

NREL, 2016. NREL efficiency chart - 2016. Available at: https://www.nrel.gov/pv/assets/images/efficiency-chart.png.

Nusbaumer, H. et al., 2003. An alternative efficient redox couple for the dye-sensitized solar cell system. *Chemistry (Weinheim an der Bergstrasse, Germany)*, 9(16), pp.3756–3763.

Nusbaumer, H. et al., 2001. CoII(dbbip)22+ Complex Rivals Tri-iodide/Iodide Redox Mediator in Dye-Sensitized Photovoltaic Cells. *The Journal of Physical Chemistry B*, 105(43), pp.10461–10464.

O'Regan, B. & Grätzel, M., 1991. A low-cost, high-efficiency solar cell based on dye-sensitized colloidal TiO2 films. *Nature*, 353(6346), pp.737–740.

O'Regan, B. & Schwartz, D.T., 1998. Large Enhancement in Photocurrent Efficiency Caused by UV Illumination of the Dye-Sensitized Heterojunction TiO2/RuLL'NCS/CuSCN: Initiation and Potential Mechanisms. *Chemistry of Materials*, 10(6), pp.1501–1509.

O'Regan, B.C. et al., 2007. Influence of the TiCl4 Treatment on Nanocrystalline TiO2 Films in Dye-Sensitized Solar Cells. 2. Charge Density, Band Edge Shifts, and Quantification of Recombination Losses at Short Circuit. *Journal of Physical Chemistry C*, 111(37), pp.14001–14010.

Ohkubo, I. et al., 2001. Pulsed Laser Epitaxy and Magnetic Properties of Single Phase Y-Type Magnetoplumbite Thin Films. *Japanese Journal of Applied Physics*, 40(12B), pp.L1343–L1345.

Ohl, R.S., 1941. Light-Sensitive Electric Device. *U.S. Patent*, 2, p.402,602.

Patrocínio, A.O.T., Paterno, L.G. & Iha Murakami, N.Y., 2009. Layer-by-layer TiO2 films as efficient blocking layers in dye-sensitized solar cells. *Journal of Photochemistry and Photobiology A: Chemistry*, 205(1), pp.23–27.

Pechen, E. V et al., 1995. Pulsed-laser deposition of smooth high-Tc superconducting films using a synchronous velocity filter. *Applied Physics Letters*, 66(17), pp.2292–2294.

Peiris, T.A.N., Senthilarasu, S. & Wijayantha, K.G.U., 2012. Enhanced performance of flexible dye-sensitized solar cells: Electrodeposition of Mg(OH)2 on a nanocrystalline TiO2 electrode. *Journal of Physical Chemistry C*, 116(1), pp.1211–1218.

Peng, B. et al., 2004. Systematic investigation of the role of compact TiO2 layer in solid state dye-sensitized TiO2 solar cells. *Coordination Chemistry Reviews*, 248(13–14), pp.1479–1489.

Peter, L.M., 2011. The Grätzel Cell: Where Next? *The Journal of Physical Chemistry Letters*, 2(15), pp.1861–1867.

Peter, L.M., 2007. Transport, trapping and interfacial transfer of electrons in dye-sensitized nanocrystalline solar cells. *Journal of Electroanalytical Chemistry*, 599(2), pp.233–240.

Pichot, F. & Gregg, B.A., 2000. The Photovoltage-Determining Mechanism in Dye-Sensitized Solar Cells. *The Journal of Physical Chemistry B*, 104(1), pp.6–10.

Prasittichai, C. & Hupp, J.T., 2010. Surface Modification of SnO2 Photoelectrodes in Dye-Sensitized Solar Cells: Significant Improvements in Photovoltage via Al2O3 Atomic Layer Deposition. *The Journal of Physical Chemistry Letters*, 1(10), pp.1611–1615.

Prince, M.B., 1955. Silicon solar energy converters. *Journal of Applied Physics*, 26(5), pp.534–540.

Riordan, M. & Hoddeson, L., 1997. Origins of the pn junction. *IEEE Spectrum*, 34(6), pp.46–51.

Rühle, S., 2016. Tabulated values of the Shockley-Queisser limit for single junction solar cells. *Solar Energy*, 130, pp.139–147.

Sanz, M. et al., 2009. Nanosecond pulsed laser deposition of TiO2: nanostructure and morphology of deposits and plasma diagnosis. *Thin Solid Films*, 517(24), pp.6546–6552.

Sharma, S.D. et al., 2006. Sol–gel-derived super-hydrophilic nickel doped TiO2 film as active photo-catalyst. *Applied Catalysis A: General*, 314(1), pp.40–46.

Shockley, W. & Queisser, H.J., 1961. Detailed balance limit of efficiency of p-n junction solar cells. *Journal of Applied Physics*, 32(3), pp.510–519.

Smestad, G.P. et al., 2003. A technique to compare polythiophene solid-state dye sensitized TiO2 solar cells to liquid junction devices. *Solar Energy Materials and Solar Cells*, 76(1), pp.85–105.

Snaith, H.J., 2010. Estimating the Maximum Attainable Efficiency in Dye-Sensitized Solar Cells. *Advanced Functional Materials*, 20(1), pp.13–19.

Sommeling, P.M. et al., 2006. Influence of a TiCl4 Post-Treatment on Nanocrystalline TiO2 Films in Dye-Sensitized Solar Cells. *Journal of Physical Chemistry B*, 110(39), pp.19191–19197.

Takahashi, Y. & Matsuoka, Y., 1988. Dip-coating of TiO2 films using a sol derived from Ti(O-i-Pr)4-diethanolamine-H2O-i-PrOH system. *Journal of Materials Science*, 23(6), pp.2259–2266.

Tétreault, N. & Grätzel, M., 2012. Novel nanostructures for next generation dye-sensitized solar cells. *Energy & Environmental Science*, 5(9), pp.8506–8516.

Thelakkat, M., Schmitz, C. & Schmidt, H.-W., 2002. Fully Vapor-Deposited Thin-Layer

Titanium Dioxide Solar Cells. *Advanced Materials*, 14(8), pp.577–581.

Toyoda, T. et al., 2004. Outdoor performance of large scale DSC modules. *Journal of Photochemistry and Photobiology A: Chemistry*, 164(1–3), pp.203–207.

Trajanovic, Z. et al., 1997. Stoichiometry and thickness variation of YBa2Cu3O7−x in pulsed laser deposition with a shadow mask. *Applied Physics Letters*, 70(25), pp.3461–3463.

Wang, P. et al., 2003. A stable quasi-solid-state dye-sensitized solar cell with an amphiphilic ruthenium sensitizer and polymer gel electrolyte. *Nature Materials*, 2(June), pp.402–407.

Wang, P. et al., 2005. Charge Separation and Efficient Light Energy Conversion in Sensitized Mesoscopic Solar Cells Based on Binary Ionic Liquids. *Journal of the American Chemical Society*, 127(18), pp.6850–6856.

Wang, Z.-S. et al., 2006. Electronic-Insulating Coating of CaCO3 on TiO2 Electrode in Dye-Sensitized Solar Cells: Improvement of Electron Lifetime and Efficiency. *Chemistry of Materials*, 18(12), pp.2912–2916.

Woo, J.-S. & Jang, G.-E., 2013. A Comparative Study on the Various Blocking Layers for Performance Improvement of Dye-sensitized Solar Cells. *Transactions on Electrical and Electronic Materials*, 14(6), pp.312–316.

Wu, X. et al., 2007. BaCO3 Modification of TiO2 Electrodes in Quasi-Solid-State Dye-Sensitized Solar Cells: Performance Improvement and Possible Mechanism. *The Journal of Physical Chemistry C*, 111(22), pp.8075–8079.

Wu, Y., Fan, R. & Yang, P., 2002. Block-by-Block Growth of Single-Crystalline Si/SiGe Superlattice Nanowires. *Nano Letters*, 2(2), pp.83–86.

Xia, J., Masaki, N., Jiang, K. & Yanagida, S., 2006. Deposition of a thin film of TiOx from a titanium metal target as novel blocking layers at conducting glass/TiO2 interfaces in ionic liquid mesoscopic TiO2 dye-sensitized solar cells. *The journal of physical*

chemistry. B, 110(50), pp.25222–25228.

Xia, J. et al., 2007a. Fabrication and characterization of thin Nb2O5 blocking layers for ionic liquid-based dye-sensitized solar cells. *Journal of Photochemistry and Photobiology A: Chemistry*, 188(1), pp.120–127.

Xia, J., Masaki, N., Jiang, K., Wada, Y., et al., 2006. Importance of Blocking Layers at Conducting Glass/TiO2 Interfaces in Dye-sensitized Ionic-liquid Solar Cells. *Chemistry Letters*, 35(3), pp.252–253.

Xia, J. et al., 2007b. Sputtered Nb2O5 as a Novel Blocking Layer at Conducting Glass/TiO2 Interfaces in Dye-Sensitized Ionic Liquid Solar Cells. *The Journal of Physical Chemistry C*, 111(22), pp.8092–8097.

Xia, J. et al., 2007c. Sputtered Nb2O5 as an effective blocking layer at conducting glass and TiO2 interfaces in ionic liquid-based dye-sensitized solar cells. *Chemical communications (Cambridge, England)*, (2), pp.138–140.

Xu, B., Cross, L.E. & Bernstein, J.J., 2000. Ferroelectric and antiferroelectric films for microelectromechanical systems applications. *Thin Solid Films*, 377–378, pp.712–718.

Yamanaka, N. et al., 2007. Dye-Sensitized TiO2 Solar Cells Using Imidazolium-Type Ionic Liquid Crystal Systems as Effective Electrolytes. *Journal of Physical Chemistry B*, 111(18), pp.4763–4769.

Yilmaz, S., Venkatesan, T. & Gerhard-Multhaupt, R., 1991. Pulsed laser deposition of stoichiometric potassium-tantalate-niobate films from segmented evaporation targets. *Applied Physics Letters*, 58(22), pp.2479–2481.

Yu, Z. et al., 2013. Fabrication and characterization of textured Bi2Te3 thermoelectric thin films prepared on glass substrates at room temperature using pulsed laser deposition. *Journal of Crystal Growth*, 362, pp.247–251.

Zaban, A. et al., 2000. Bilayer nanoporous electrodes for dye sensitized solar cells.

Chemical Communications, pp.2231–2232.

Zaban, A., Meier, A. & Gregg, B.A., 1997. Electric Potential Distribution and Short-Range Screening in Nanoporous TiO2 Electrodes. *The Journal of Physical Chemistry B*, 101(40), pp.7985–7990.

Zhang, Z. et al., 2007. Effects of ω-Guanidinoalkyl Acids as Coadsorbents in Dye-Sensitized Solar Cells. *The Journal of Physical Chemistry C*, 111(1), pp.398–403.

Zhang, Z. et al., 2005. Influence of 4-Guanidinobutyric Acid as Coadsorbent in Reducing Recombination in Dye-Sensitized Solar Cells. *The Journal of Physical Chemistry B*, 109(46), pp.21818–21824.

Appendix A

I-V characteristics of the samples with thin deposited film that were carbon coated. Measured in two cycles of forward and reverse bias. Applied voltage range from -1 V to 1 V.

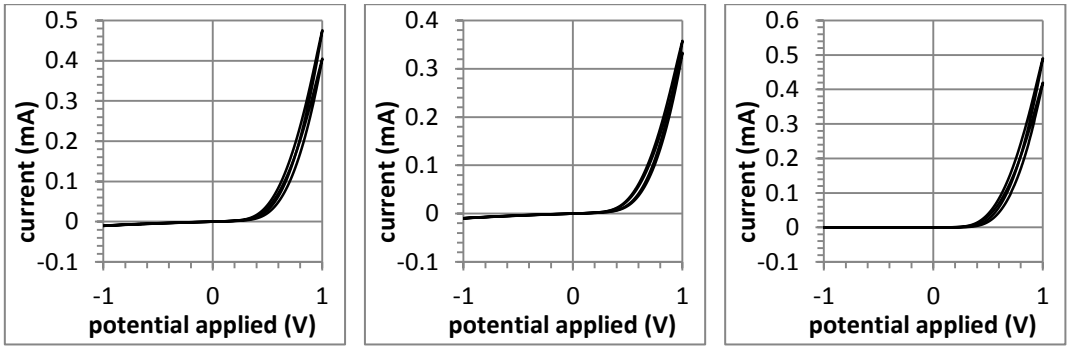

(a) (b) (c)

Figure A.1: I-V characteristics of the sample with thin deposited film that was carbon coated; measured in 3 positions, sample BL120/0.26

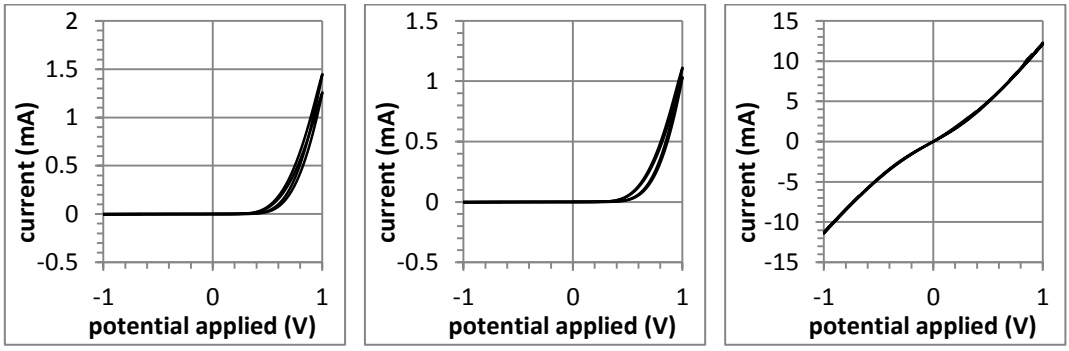

(a) (b) (c)

Figure A.2: I-V characteristics of the sample with thin deposited film that was carbon coated; measured in 3 positions, sample BL30/0.26

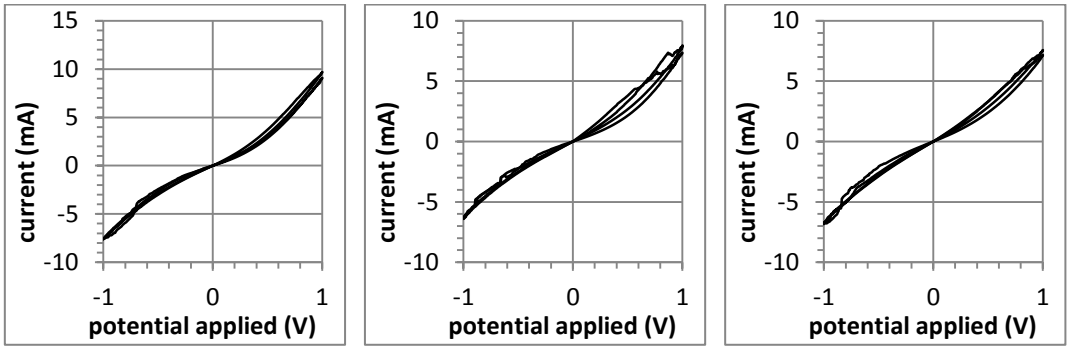

(a) (b) (c)

Figure A.3: I-V characteristics of the sample with thin deposited film that was carbon coated; measured in 3 positions, sample BL15/0.26

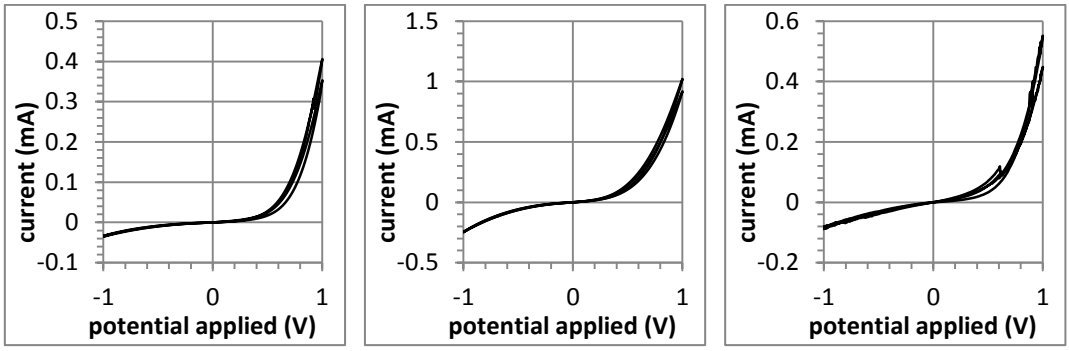

(a) (b) (c)

Figure A.4: I-V characteristics of the sample with thin deposited film that was carbon coated; measured in 3 positions, sample BL30/1.00

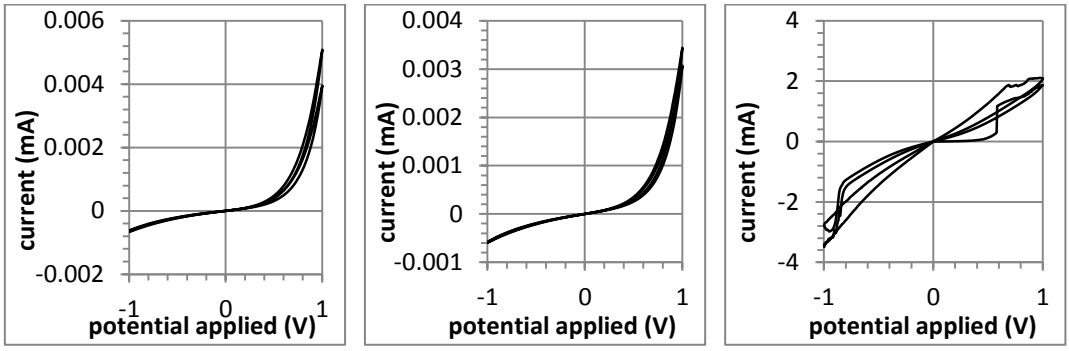

(a) (b) (c)

Figure A.5: I-V characteristics of the sample with thin deposited film that was carbon coated; measured in 3 positions, sample BL30/2.00

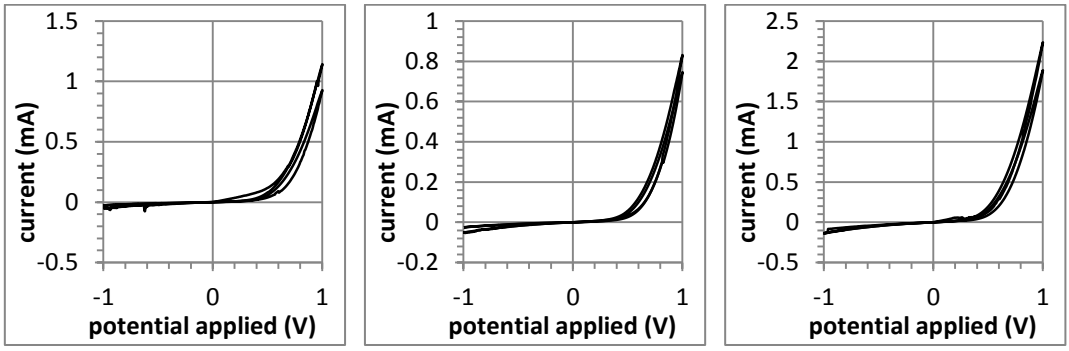

(a) (b) (c)

Figure A.6: I-V characteristics of the sample with thin deposited film that was carbon coated; measured in 3 positions, sample BL30/0.18

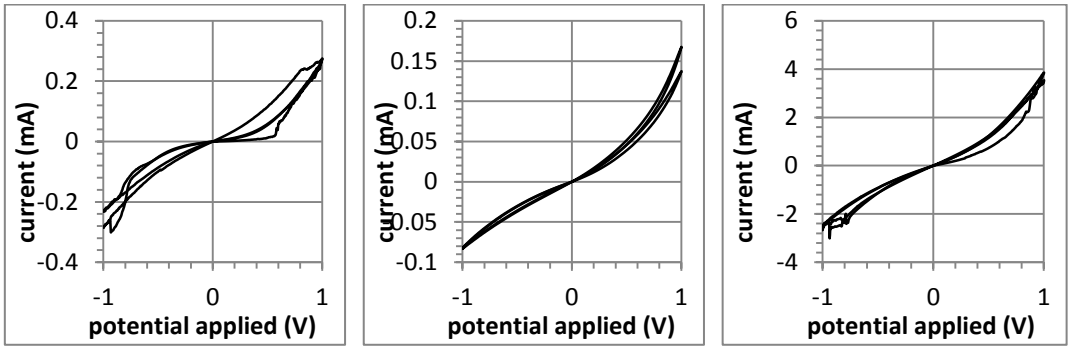

(a) (b) (c)

Figure A.7: I-V characteristics of the sample with thin deposited film that was carbon coated; measured in 3 positions, sample BL30/0.14

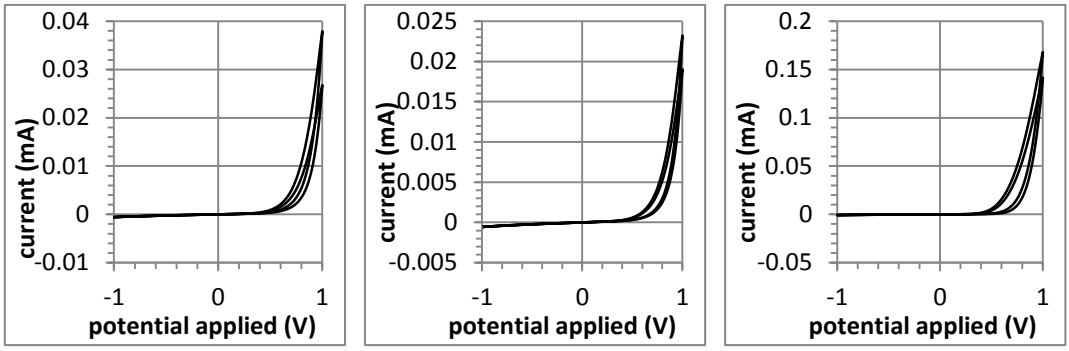

(a) (b) (c)

Figure A.8: I-V characteristics of the sample with thin deposited film that was carbon coated; measured in 3 positions, sample BL30/0.11

Appendia B

List of publications and conference presentations

Publications

- Augustyniak, M. and Min, G., 2016, Influence of various titanium oxide blocking layers on performance of dye-sensitized solar cells. IEEE Xplore. In 2016 International Conference for Students on Applied Engineering (ICSAE) (listed for the conference proceedings)

- Mars, K., Godlewska, E., Augustyniak, M., Mitoraj, M., 2015. Mg_2Si layers deposited by pulsed magnetron sputtering. *Elektronika: konstrukcje, technologie, zastosowania*, 56(2), pp.108-110.

- Preparation and characterisation of titanium oxide thin films deposited by pulsed laser deposition (under preparation)

Conference presentations

- The International Conference for Students on Applied Engineering ICSAE 2016, Newcastle, United Kingdom, 20-21 October 2016

- Gregynog conference 2016 - Cardiff School of Engineering 8th ENGIN Postgraduate Conference, Gregynog, 27-29 June 2016.

- Speaking of Science 2016 Conference, Cardiff, 5th May 2016.